Fibre Optic Sensors Based on D-Shaped Elliptical Core Fibres

by

Sameer M. Chandani

B.Sc.E., Queen's University, 1998
M.A.Sc., University of British Columbia, 2002

A THESIS SUBMITTED IN PARTIAL FULFILMENT OF
THE REQUIREMENTS FOR THE DEGREE OF

DOCTOR OF PHILOSOPHY

in

THE FACULTY OF GRADUATE STUDIES

(Electrical and Computer Engineering)

THE UNIVERSITY OF BRITISH COLUMBIA

September 07

Abstract

Optical fibre-based sensors have gained much attention over the past three decades and are gaining acceptance in many industries such as the aerospace, automotive, chemical processing, biological sensing, and medical industries. The work presented here demonstrates the use of D-shaped fibres as intensity-based fibre optic sensors. The fibres are etched to gain access to their evanescent optical fields and are operated in their "leaky" regimes, i.e., the regime in which optical power leaks out of their cores. The optical power transmission through the etched D-fibre, which constitutes the sensor head, depends on the refractive index of the measurand placed on the sensor head. Thus by using materials whose refractive indices depend on the desired measurands, intensity-based sensors can be realised. A "non-destructive" process for determining the etched cladding thickness of the D-fibre is also developed. Once calibrated for a specific fibre or fibre batch, only one thermo-optic oil, three temperature measurements and a mathematical fitting routine are required to determine the etched cladding thickness with an accuracy better than 0.3 μm. Four types of sensor are demonstrated. A refractive index sensor with a high resolution region and a low resolution region, both of which can be shifted by changing the operating wavelength, is demonstrated with a maximum resolution on the order of 10^{-6} refractive index units. Naturally, this leads to the development of a temperature sensor with an adjustable dynamic range and resolution that uses thermo-optic oils. Proof of principle is demonstrated for an electric field sensor using chiral smectic A liquid crystals. A continuous liquid level sensor (that can also be implemented as a discrete level sensor) is also demonstrated using only one optical source, one optical detector and a single length of fibre.

Contents

List of Tables

List of Figures

List of Symbols and Abbreviations

EPW	Equivalent planar waveguide
BHF	Buffered hydrofluoric acid
n_{co}	Fibre core refractive index
n_{cl}	Fibre cladding refractive index
k_o	Free space propagation constant
n_{eff}	Fibre mode effective index
β	Fibre mode propagation constant
T_p	Power transmission ratio
n_{si}	Refractive index of undoped silica
a	Elliptical core semimajor axis
b	Elliptical core semiminor axis
$\Psi(x,y)$	Modal field of the d-fibre
Ψ_x	Scalar mode of the slab with index variations in the x.
Ψ_y	Scalar mode of the slab with index variations in the y.
p_x, p_y, σ_x, and σ_y	Adjustable parameters used in maximization of β^2 in Sharma's model
d'	Cladding thickness of the equivalent planar waveguide
d	Cladding thickness of d-fibre
d_{shift}	Empirical parameter used in simplified theoretical model to shift EPW
dn/dT	Thermo-optic coefficient of oil
n_0	Refractive index of oil at 25°C
SEM	Scanning electron microscope
n_{ext}	External medium's refractive index
L	Length of etched section of d-fibre
λ_o	Operating wavelength
$_oHE_{11}$	Notation used for the odd fundamental of elliptical fibres
n_{x1} and n_{x2}	Core and cladding refractive indices of EPW
ΔT_P	Power transmission measurement resolution
n_{liq}	Refractive index of liquid
d_{opt}	Optimal cladding thickness

β_r	Real part of complex propagation constant of leaky mode
β_j	Imaginary part of complex propagation constant of leaky mode
γ	Power attenuation coefficient of leaky mode
P_{in} and P_{out}	Power into and out of sensor head, respectively
M_P	Slope of the power transmission ratio
d_{fit}	Fitted cladding thickness required to fit measured transmission and slope to calculated ones
b_{fit}	Fitted semiminor axis required to fit measured transmission and slope to calculated ones
d_{SEM}	Cladding thickness measured using SEM images
Δd	$\Delta d = \lvert d_{SEM} - d_{fit} \rvert$
FBG	Fibre Bragg grating
RIU	Refractive index units
SRI	Surrounding refractive index
n_s	Refractive index of surrounding refractive index
Δn_s	Resolution of refractive index measurement
n_{max}	Refractive index at which the maximum resolution occurs in Region III
SmA*	Chiral Smectic A liquid crystal
LCs	Liquid crystals
n_e and n_o	Extraordinary and ordinary refractive index of liquid crystal
$\tilde{N}$	Director of liquid crystal
$\tilde{E}_{app}$	Applied electric field
n_θ	Angle dependent refractive index
ITO	Indium tin oxide
LIA	Lock-in amplifier

Acknowledgments

My deepest gratitude goes to my family for supporting me throughout my education. Special thanks to my parents for their love, support, understanding and encouragement throughout the duration of this degree. I would like to thank my close friends for being there through the ups and downs experienced during my graduate years and for putting up with my many antics.

Finally, I would like to thank my supervisor, Dr. Jaeger, for his knowledgeable guidance. He has been a mentor, colleague and much more than a supervisor. His belief in my abilities and potential has helped me get through the challenges of graduate work.

Chapter 1

1 Introduction

1.1 Overview and Motivation

Due to the limitations of the human body, mankind continues to develop sensors and sensor systems to better understand and quantify his environment. The need to monitor, measure and understand the many processes occurring around us has never been greater than in today's technological society. Consequently, scientists and engineers continue to develop new sensor technologies and/or improve on the sophistication of existing sensor systems.

The development of fibre optics for optical communications applications has enabled, as an added benefit, the parallel development of the optical sensors industry. The use of fibre optics to develop and manufacture sensors has been the subject of intense research for over three decades [1]. In particular, the availability of photonic components such as lasers, detectors, and most importantly, optical fibre has significantly contributed to the growth of the fibre optics sensor field. It is expected that the continued availability and decreasing cost of specialised optical fibres and components will lead to the further maturation of the optical sensors industry.

This chapter begins with an introduction to fibre optic sensors including their classification, types, advantages and disadvantages, and their application niches. It is intended to give the reader an appreciation, and basic understanding, of this field of study. A description of a particular type of fibre optic sensor, the evanescent wave sensor, is provided and facilitates the description of the sensors developed in the present work. The chapter concludes with a summary and outline of the thesis.

1.2 Fibre Optic Sensors [2, 3]

1.2.1 Definition

An optical sensor is one in which the principle of operation involves the modulation of light by the measurand. Thus, this requires the use of a light source and, in most cases, a photo detector to convert the modulated light signal into an electrical one. A fibre optic sensor is a special kind of optical sensor wherein an optical fibre is used. The fibre can be used either to guide the light towards the measurand (the optical channel) or to interact with the measurand (the sensor head) or both. The measurand changes the properties of the light traveling in the sensor head e.g., the

light's amplitude, wavelength, polarization state, or phase. These changes are then converted to electrical signals using photo detectors.

1.2.2 Sensor Classification

Optical sensors can be classified into groups based on the type of measurand being investigated.

a) *Mechanical*: includes the measurement of displacement, acceleration, velocity, force, pressure, torque, flow, changes in mass, etc.
b) *Thermal*: includes the measurement of temperature and heat flow.
c) *Electromagnetic*: includes the measurement of electric field, magnetic field, voltage and currents.
d) *Radiation*: includes measurement of X-rays and nuclear radiation.
e) *Chemical*: includes measurement of parameters such as toxicity, acidity, refractive index or chemical composition.
f) *Flow and Turbulence of Fluids*: includes measurement of turbidity in fluids.
g) *Biosensors*: includes measurement of typical magnitudes in biological systems such as oxygen, carbon dioxide, blood flow, DNA identification, etc.

1.2.3 Spatial Distribution

Depending on how the sensor is implemented in the measurand's environment, the sensor can be either a point sensor, an integrated sensor, a distributed sensor, or a quasi-distributed sensor as shown in Figure 1-1.

a) A point sensor measures the state of the measurand at a single point in space. When making measurements over a defined space, often multiple sensors are required, each sensor requiring its own optical channel.
b) In integrated sensors the measurement is integrated over a space from all the contributions from the measurand along the sensor head and thus results in a single signal. An example of this is the measurement of an electric current by integration of the magnetic field, created around the conductor, in a loop of fibre.
c) Distributed sensors measure the state of the measurand along a line in space with a given spatial resolution. Thus they allow the measurement of the measurand state in a continuous way at each point in space. An example of this is the measurement of the distribution of the temperature and/or strain along a length of fibre, where the fibre forms the optical channel as well as the sensor head.

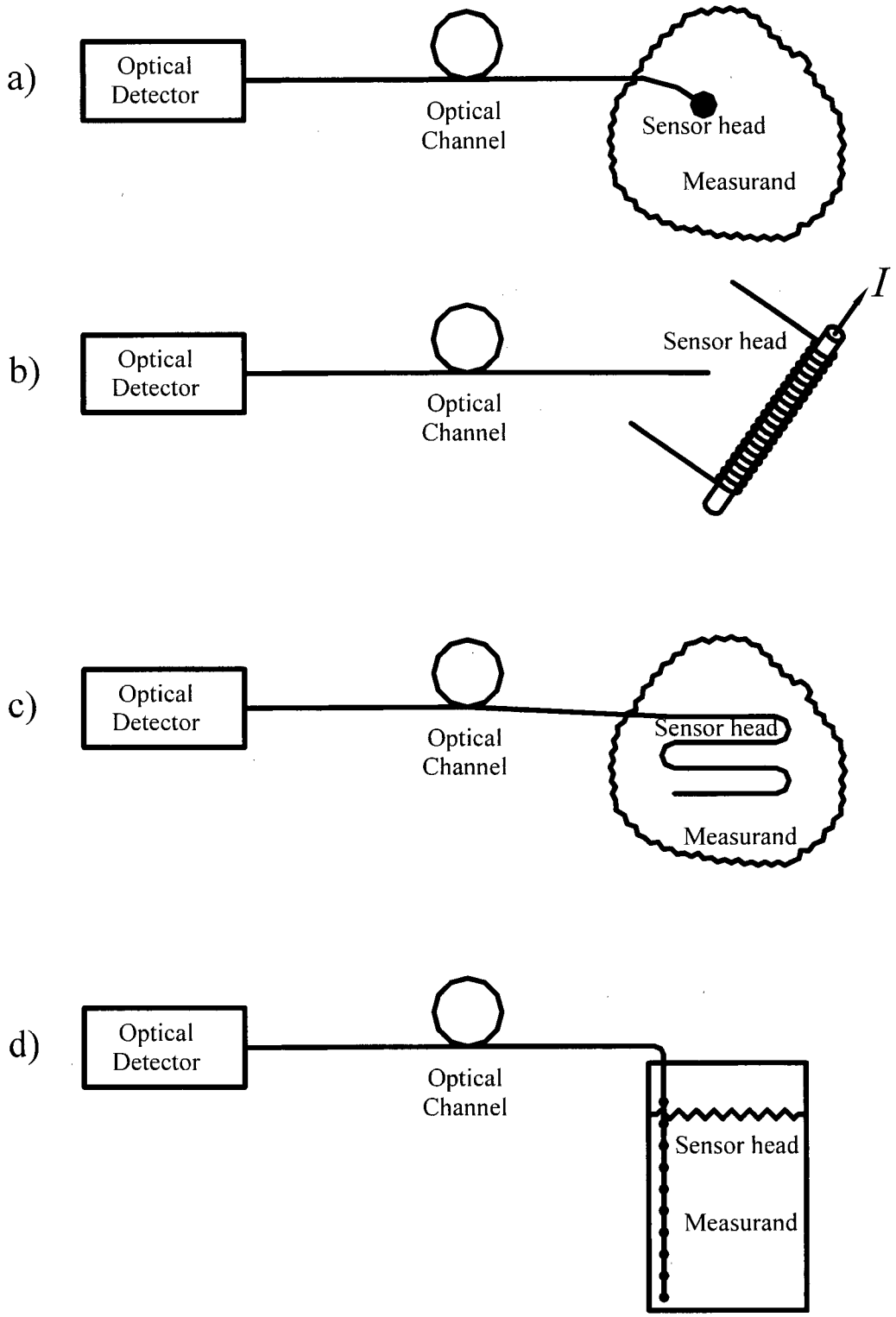

Figure 1-1: Spatial distribution of fibre optic sensors. a) Point sensor, b) Integrated sensor, c) Distributed sensor, d) Quasi-distributed sensor.

d) Quasi-distributed sensors measure the state of the measurand at discrete points in space. An example of this is the measurement of the liquid level by sensors placed at discrete points along the wall of a tank.

1.2.4 Nature of Transduction

Depending on how the measurand interacts with the sensor head, fibre optic sensors can be grouped in to two categories:

a) *Intrinsic*: The light remains guided in the fibre and the measurand surrounds the sensor head. In this case, the measurand changes the intrinsic properties of the fibre in order to modulate the light guided within it.

b) *Extrinsic*: The interaction between the light and measurand takes place in an external device. Here, light is delivered to the device via an input fibre and extracted via an output fibre. Often, a single fibre is used as both the input and output fibre.

1.2.5 Modulation of Light

According to the type of modulation of the light, optical sensors can be classified in four ways.

a) *Intensity-based sensors*: the optical intensity of the light travelling in the sensor is modulated by the measurand.

b) *Interferometric sensors*: the phase of the optical wave is modulated by propagation through the sensor.

c) *Polarimetric sensors*: the polarization state of the light is modulated by the measurand.

d) *Spectroscopic or wavelength-based sensors*: the optical spectrum is modulated by the measurand.

1.2.6 Advantages of Fibre Optic Sensors

a) Made with dielectric materials that are, generally speaking, chemically inert.

b) Immune to electromagnetic interference.

c) Biocompatible, reliable and non-intrusive.

d) Withstand high temperatures.

e) Small size, compact and light-weight.

f) Fibre can be used as the optical channel (allows for remote measurements).

g) High sensitivities, wide dynamic ranges and high resolutions.

h) Allows for distributed sensors (very difficult using conventional technologies).

i) Ever decreasing component costs.

1.2.7 Disadvantages of Fibre Optic Sensors

There are two main disadvantages, or impediments, to using fibre optic sensors:

a) The sensitivity of a fibre optic sensor to other influences can cause errors in the measurement. This cross sensitivity is caused by the effects of undesired measurands such as temperature on the fibre. Nevertheless, this problem also exists for many conventional sensors.

b) In many cases, conventional sensors are still more cost effective. The cost of implementing fibre optic sensors also includes the cost of replacing current conventional sensors in existing applications.

1.2.8 Application Niches

Based on the above advantages and disadvantages of fibre optic sensors, it is evident that there are many sensor applications which can be improved. Thus, fibre optic sensors can be more ideal for some applications, which are listed below.

a) Areas of high electromagnetic interference such as power substations, transformers, alternators, electric motors, power supply lines, etc.

b) Nuclear plants or areas where radiation can be harmful to health and remote measurement is required.

c) Aerospace and transportation industries where light-weight, high-speed and electromagnetic immunity are advantageous.

d) Medicine and biotechnology applications such as "in-vivo" measurements of pressure, pH of blood, and temperature. Other applications such as intravenous surgical cameras and laser surgery.

e) Point measurements of chemical compounds in the environment, e.g., gas sensors.

f) Applications requiring great sensitivity such as accelerometers, hydrophones, gyroscopes, electric and magnetic field measurements.

g) Applications requiring non-metallic and non-radiative parts, e.g., flammable environments and security applications.

h) Distributed sensing of variables such as temperature and strain.

1.3 Evanescent Wave Sensors

In this thesis, the sensors presented use evanescent optical fields to interact with the measurand. This section is intended to give the reader a brief introduction to evanescent fields in optical waveguides.

1.3.1 The Evanescent Optical Field

Figure 1-2a) shows the cross section of a typical circular step-index single-mode fibre. Figure 1-2b) shows the blow up of the core and the radial refractive index and optical field distributions in the region of the core. In such a fibre, the refractive index of the core, n_{co}, is larger than that of the cladding, n_{cl}, and total internal reflection at the core-cladding boundary guides the light. While certain principles of light guiding can be explained using ray theory, deeper insights can be obtained using complete solutions of Maxwell's equations for electromagnetic radiation. Using Maxwell's equations and assuming time harmonic electromagnetic fields leads to the Helmholtz equation:

$$\nabla^2 \vec{E}(\vec{r}) + k_o^2 n(r)^2 \vec{E}(\vec{r}) = 0 \tag{1-1}$$

where k_o is the free space propagation constant, n is the refractive index distribution and $E(r)$ is the electric field vector. Since we are interested in fields that propagate in the fibre, it is common to pick a field of the form

$$\vec{E}(\vec{r}) = \vec{E}(r,\varphi)e^{-j\beta z} \tag{1-2}$$

where cylindrical coordinates are used for fibres with circular symmetry and β is the longitudinal propagation constant. It can be shown that the transverse components of the field can be expressed in terms of the longitudinal components of the field and thus it is only necessary to solve the wave equation for the longitudinal components. Substituting equation (1-2) into equation (1-1) gives

$$\nabla_t^2 E_z(r,\varphi) + (k_o^2 n^2 - \beta^2) E_z(r,\varphi) = 0 \tag{1-3}$$

for the longitudinal component.

Using appropriate fields in the core and cladding, equation (1-3) can be used to determine the modes of the fibre, which are characterized by their fields being harmonic functions. "Guided modes" are modes in which the optical field is confined to the core and the fields are oscillatory in the core and decaying in the cladding (see Figure 1-2b)). These decaying fields in the cladding are referred to as "evanescent fields". "Radiation modes" are characterised by oscillatory fields in the cladding. A subset of radiation modes are "leaky modes", which form the basis of the sensors investigated in this thesis (these will be discussed in detail later).

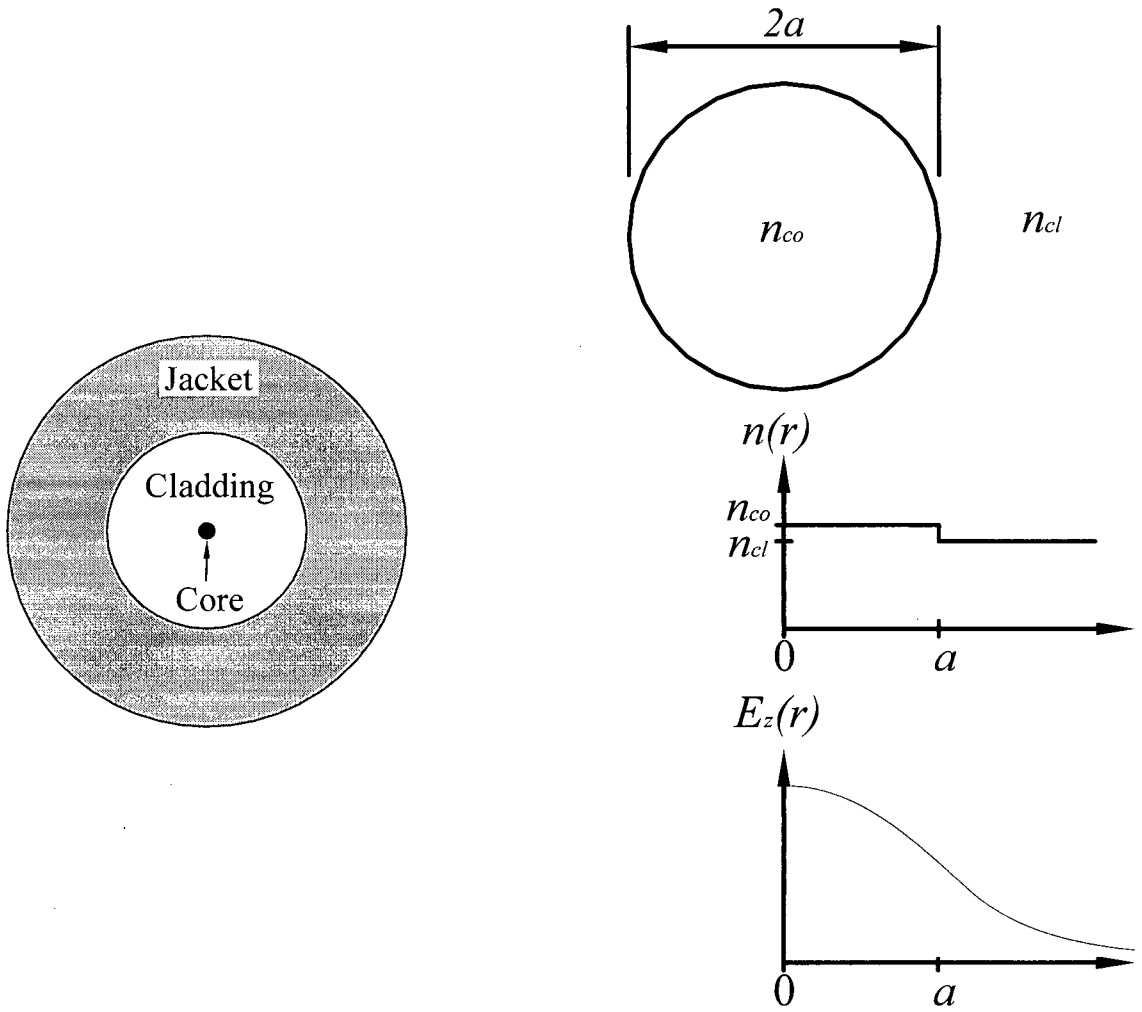

a) b)

Figure 1-2: a) Cross section of a typical step-index single-mode fibre. b) Blow up of the core and radial refractive and optical field distribution in the region of the core.

1.3.2 Evanescent Wave Sensors

As described in the previous section, for guided modes there exists an evanescent field in the cladding of an optical fibre. This field can be used to create a sensor by allowing it to interact with a measurand which, in turn, affects the propagation of light in the fibre [4]. The evanescent field is typically a weak, decaying one. Access to the evanescent field requires removal of part of the fibre's cladding. The removed cladding is replaced by the measurand (or by a material that is sensitive to the measurand) as shown in Figure 1-3. Because of the rate of decay of the evanescent field, the distance between the edge of the core and the edge of the cladding needs to be reduced to a few micrometres.

This access to the evanescent field is accomplished by "side-polishing" a fibre or by starting with a "D-fibre" and etching away part of its cladding as shown in Figure 1-4. Side-polishing involves fixing a fibre into a curved V-groove on a quartz or silicon substrate and polishing the exposed side to the desired depth [5]. The resulting fibre is a side-polished fibre and is used to create a variety of fibre optic sensors [6], [7], [8], [9], [10], [11]. Since the fibre is fixed to a curved groove, the polish depth varies along the length of the sensor head and thus the effective interaction length between the measurand and evanescent field is usually limited.

A D-fibre is a fibre that has a D-shaped cross section. As manufactured, the minimum distance between the core edge and the flat side of the D is usually 10-20 μm [12]. This distance can be reduced by etching the fibre. Typically, this etching is done in a solution of hydrofluoric acid [13]. D-fibres have been used in various fibre optic sensor applications [14]-[21]. A Bragg grating etched into the surface of the D-fibre flat has been used to demonstrate a temperature sensor. The Bragg wavelength was proportional to the temperature up to a temperature of 1100°C [14], [15]. A long-period fibre Bragg grating UV-inscribed into a D-fibre with an etched (reduced) cladding was shown to have a higher sensitivity as a refractive index sensor as compared to a grating on a regular fibre [16]. The shift of the resonance wavelength of the grating was sensitive to the surrounding refractive index. This same concept was also demonstrated as a directional bend sensor [17]. Fibre optic sensors for the monitoring of cryogenic spacecraft tank structures using an inscribed Bragg grating in a D-fibre with a 2-10 μm thin palladium foil glued onto the flat side of the D-fibre were demonstrated in [18]. A methane gas sensor was demonstrated by using a 5 metre length of D-fibre to measure the absorption line of methane, which is around 1.66 μm [19]. For the above examples, the shift in the resonance wavelength of the Bragg gratings was monitored and thus the measurement required an optical spectrum analyzer. The change in birefringence of a D-fibre when surrounded by a liquid was

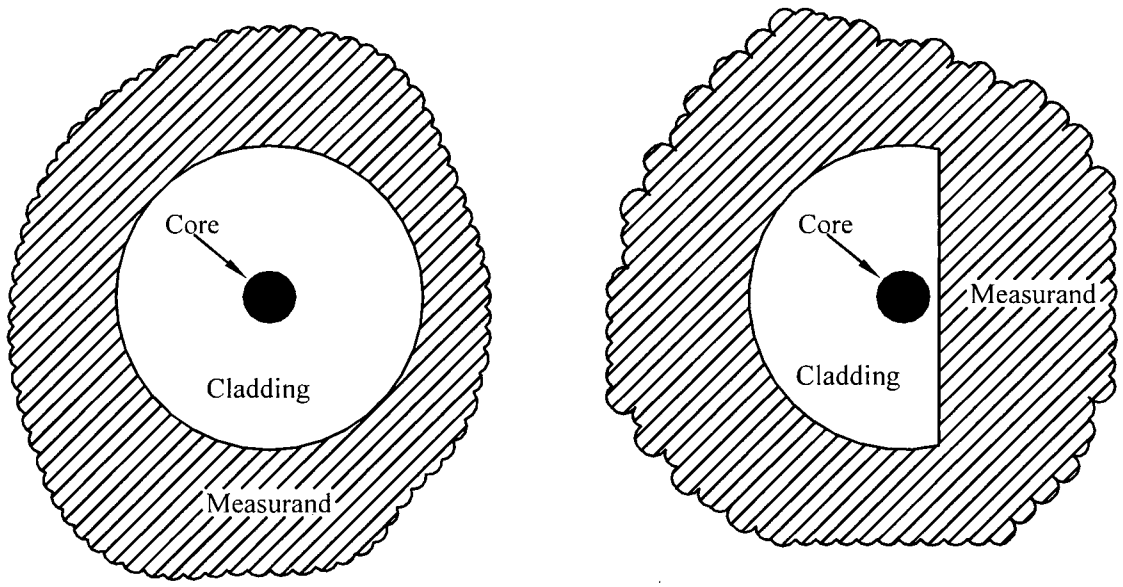

Figure 1-3: a) Cross section of a fibre immersed in a surrounding medium. b) Cross section of a fibre with part of its cladding removed and immersed in a surrounding medium to gain access to the evanescent field.

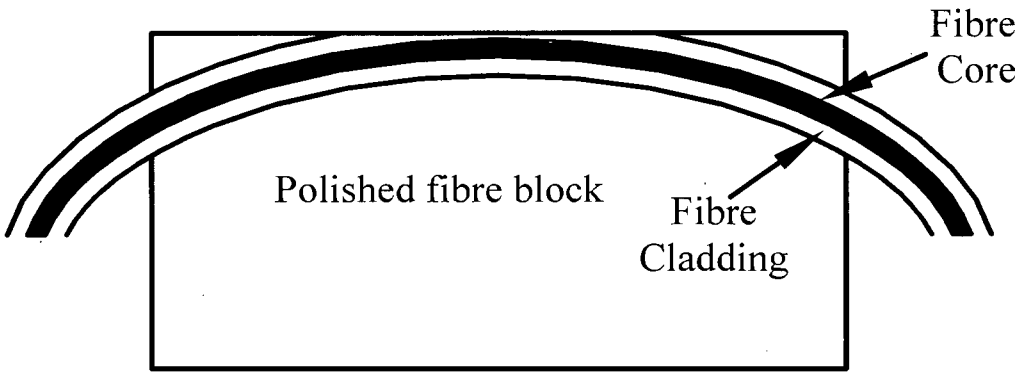

a)

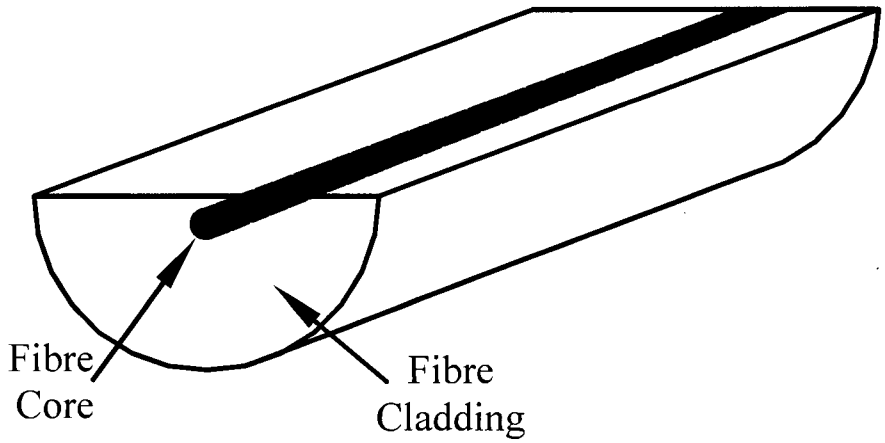

b)

Figure 1-4: a) Fibre fixed to a curved groove in a block and side-polished. b) D-fibre etched to reduce cladding thickness

used to create a liquid contamination detector [20]. A surface-enhanced Raman scattering sensor based on a D-shaped fibre was demonstrated in [21]. Surface-enhanced Raman scattering sensors are used as molecular sensors whereby Raman-scattering is induced in colloidal solutions or in thin films. By coating the D-fibre with a film, the interaction length between the optical field and the film was increased resulting in a stronger Raman signal.

D-fibres offer two advantages over side-polished fibres: 1) the interaction length between the optical evanescent field and the measurand can be quite long; and 2) the control of the distance between the fibre core and the measurand is more easily achieved, i.e., by etching the fibre as opposed to side-polishing it.

1.4 Overview of Thesis

1.4.1 Summary

This thesis describes the investigation into fibre optic sensors based on D-shaped fibres used in their leaky regimes. Such fibres have to-date been used as wavelength-based sensors and/or in their guided regimes, whereas the sensors developed here are intensity-based and aim to provide similar or better resolutions and dynamic ranges. The thesis presents a theoretical model to describe the behaviour of the D-fibre sensors with regards to their operating regions and resolutions. A software package is also used to further verify the model and demonstrate the ability to model the fibres actually used. The model is also verified by experimental data. It is shown that, once calibrated, a simplified version of the model can be used to determine, in a non-destructive way, the cladding thicknesses of the etched fibres to facilitate their manufacture. Four types of sensor are investigated, fabricated and characterized. These are a refractive index sensor, a temperature sensor, an electric field sensor, and a liquid level sensor.

1.4.2 Outline

The remainder of this thesis is divided into seven chapters. Chapter 2 describes the operating principles of the sensors and presents a theoretical model and software simulations conducted to describe D-fibre sensors. Chapter 3 describes the fabrication steps required to etch a fibre with a known cladding thickness. A non-destructive technique to determine the etched cladding thickness is described. Chapter 3 also describes the experimental setup used to measure the power transmission ratio of the D-fibre sensors.

Chapters 4 through 7 describe and present measurements and results on four types of sensor based on D-fibres. Chapter 4 presents a high resolution refractive index sensor along with an analysis of the sensor's resolution and operating point. Chapter 5 presents a temperature sensor

with an adjustable operating point and range. Chapter 6 shows proof of principle of an electric field sensor using chiral smectic A liquid crystals. Chapter 7 describes a novel liquid level sensor that can be used as a continuous or discrete level sensor using only one fibre, one source and one detector. Finally, Chapter 8 provides suggestions for possible future work in this field, a summary and conclusions.

Chapter 2

2 Theory

2.1 Introduction

In this chapter the operating principles of the sensor are presented. An existing theoretical model is presented and used to illustrate the general behaviour of the type of sensor studied. The principle of operation of D-fibre sensors, which includes an introduction to leaky modes, is presented in Section 2.2. A D-shaped, elliptical-core fibre, which is the fibre used in this work, is physically described in Section 2.3, with a brief introduction to the fundamental modes of an elliptical fibre. The theoretical model used to describe the D-fibre with an external medium is presented in Section 2.4. A commercially available software package, BeamPROP™ (RSoft, Inc., Ossining, NY) [22], is used to simulate the actual fibre in Section 2.5 and thus validate the theoretical model.

2.2 Principle of Operation

As mentioned earlier, solutions to the Helmholtz equation are usually sought such that the modes are guided ones, i.e., the fields decay exponentially as one moves away from the core-cladding boundary. However, it is possible to find solutions such that the fields in the cladding are also oscillatory. Such solutions are "radiation modes". These modes play an important role is describing how radiation can be coupled into or out of the fibre. There exists a set of radiation modes that are able to propagate within the fibre for long distances in which much of the power remains in or close to the core [23]. Such modes are called "leaky modes". These modes generally have field descriptions that are almost the same as the field descriptions of guided modes. The only difference being that the leaky modes radiate power away from the core as they propagate along the fibre, i.e., power leaks out of the fibre core. Thus leaky modes can be described approximately by modes which are similar to the guided modes within or near the core but that have complex propagation constants such that the power in the core attenuates with propagation along the fibre.

Leaky modes commonly occur in waveguides in which the cladding has been modified or a second cladding has been added. Shown in Figure 2-1(a) is the boundary between two media having refractive indices of n_1 and n_2, with $n_2 < n_1$. For plane waves incident at angles greater

than the critical angle, θ_c (=$\sin^{-1}(n_2/n_1)$), there will be total internal reflection at the boundary. However, if a third medium of refractive index greater than n_2, is introduced, as shown in Figure 2-1(b), then even for incident angles greater than the critical angle, a portion of the energy will tunnel through to the second medium and appear in the third medium. This phenomenon is known as frustrated total internal reflection [24]. When applied to a waveguide structure, this phenomenon prevents the structure shown in Figure 2-1(c) from supporting a guided mode and the energy launched into the waveguide will gradually leak out of the core.

The phenomenon of leaky modes forms the basic operating principle of the sensors studies here, i.e., of etched D-fibres immersed in an external medium (see Figure 1-3). If the refractive index of the external medium is greater than the mode effective index, ($n_{eff} = \beta/k_o$), a leaky mode exists [25], [26], [27], [28], [29]. The propagation constant for the leaky mode is complex and the propagating electric field can be written as

$$E(z) = E_o e^{-j(\beta_r - j\beta_j)z} \tag{2-1}$$

where β_r and β_j are the real and imaginary parts of the propagation constant, respectively. The power transmission ratio, T_P, of a leaky section of the D-fibre can be written in terms of the power into, P_{in}, and the power out of, P_{out}, the leaky section as

$$T_p = \frac{P_{out}}{P_{in}} = e^{-2\beta_j L} = e^{-\gamma L} \tag{2-2}$$

where L is the length of the leaky section and γ (=$2\beta_j$) is the power attenuation coefficient.

Thus by etching a length of D-fibre and surrounding it with an external medium of refractive index, n_{ext}, that is greater than the mode effective index, n_{eff}, an intensity-based fibre optic sensor can be realised. The external medium can be chosen such that its refractive index is sensitive to the measurand. Examples of such materials include electro-optic materials, whose refractive indices change with applied electric fields, and thermo-optic oils, whose refractive indices change with temperature.

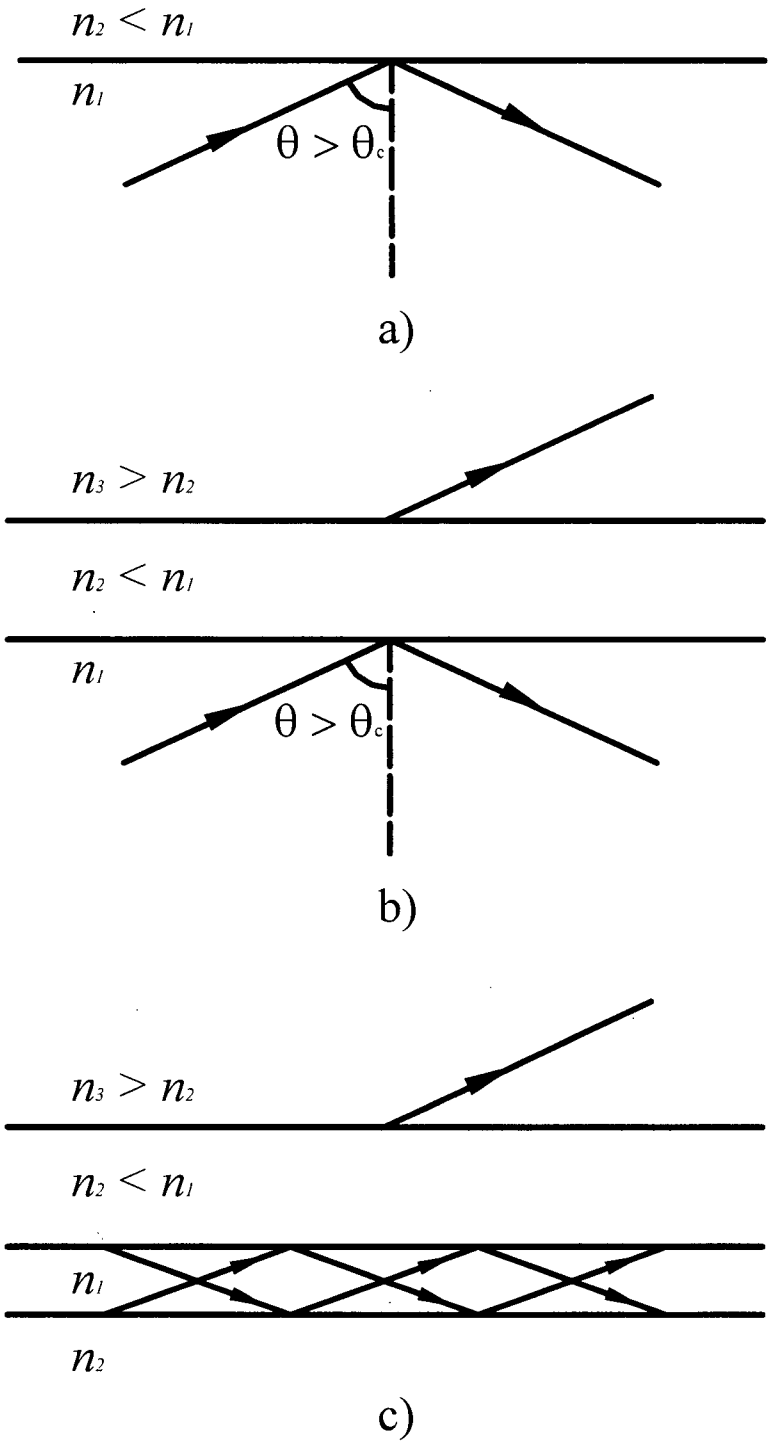

Figure 2-1: a) Total internal reflection at an interface; b) frustrated total internal reflection; c) leaky planar structure.

2.3 D-Shaped Elliptical Core Fibre

2.3.1 Physical Description

In this section, we describe the actual fibre used to create fibre optic sensors based on D-shaped fibres. Because D-fibres are a special type of fibre, they are not widely available. The fibre used in this work was commercially available from KVH Industries (Middletown, RI). It is a single-mode polarization-maintaining fibre. It has an elliptical core, which, due to the birefringence introduced by the ellipticity of the core, makes it polarization maintaining. Figure 2-2 shows the cross section of the D-fibre used. Based on information gathered from the manufacturer and published literature, the elliptical core of the fibre has a semimajor axis of $a \approx 2$ μm, a semiminor axis of $b \approx 1$ μm, and is germania-doped with a refractive index $n_{co} = 1.4756$. The cladding is fluorine-doped with a refractive index $n_{cl} = 1.441$. At the core's centre there exists a circular undoped silica region ($n_{si} = 1.444$) of approximate radius 0.4 μm. This undoped region is referred to as a "vapour spot" and is an artefact of the manufacturing process [30], [31]. All refractive indices are given for an operating wavelength of 1550 nm. The exact refractive index distributions of the core and circular undoped region are unknown and for the purpose of modelling the fibre, are assumed to have step-index profiles. The cladding thickness, d, defined as the minimum distance between the fibre core edge and the flat of the fibre, is approximately 13 μm for as-manufactured fibres.

2.3.2 Elliptical Fibre Waveguides

As we are dealing with an elliptical core waveguide, this section provides a brief description of the modes of elliptical waveguides. The fundamental mode, HE_{11}, of a circular single-mode fibre splits into two fundamental modes in an elliptical fibre [32], [33]. In keeping with the literature for elliptical waveguides, these two fundamental modes are the odd HE_{11} ($_oHE_{11}$) mode and the even HE_{11} ($_eHE_{11}$) mode. The $_oHE_{11}$ mode has its transverse field polarized parallel to the major axis and the $_eHE_{11}$ mode polarized parallel to the minor axis of the elliptical core. Both modes have different propagation constants and thus the fibre exhibits birefringence.

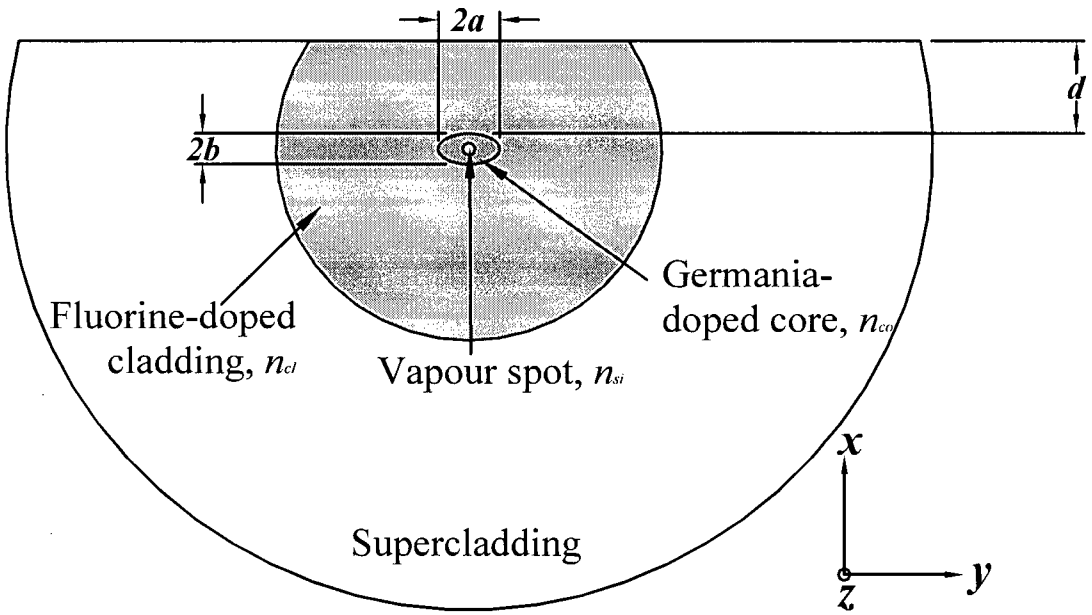

Figure 2-2: Cross section of D-fibre showing doped core and cladding regions, undoped silica region (vapour spot) and cladding thickness (not to scale).

2.4 Theoretical Model of D-fibre

There are several methods proposed to model fibres with their claddings limited by a plane [25], [28], [29], [34], [35], [36], [37], [38]. Here, we use the method proposed by Sharma *et al.* [35] which aims to replace the core of the fibre with an equivalent planar waveguide, which can then be extended to a four-layer planar structure to take into account the external medium. The method was chosen as it allows for the inclusion of the undoped circular region that is present in the D-fibre's core. Once the four-layer structure is determined, the propagation constant of its leaky mode can be computed analytically using the theory of leaky absorbing structures developed by Thyagarajan *et al.* [39]. The imaginary part of the propagation constant is given analytically for the TE_0 mode of a leaky four-layer planar structure. This TE_0 mode corresponds to the ${}_oHE_{11}$ mode of the elliptical fibre, and is often referred to as the TE-like mode.

Sharma's method proposes to replace a fibre with an equivalent planar waveguide (EPW). The equivalence is achieved by matching, as far as possible, the modal fields in the direction of interaction and the propagation constants for the fibre and its EPW. The method of finding the EPW is based on the variational method. The EPW is a step-index slab waveguide and is defined based on the direction of interaction. Thus, if the evanescent tail of the fibre field in the cladding interacts with the external medium along the x-axis, then the EPW should have its interfaces along the y-z plane; this is termed an x-slab (Figure 2-2 shows the coordinate system). Likewise, a y-slab can also be defined. Sharma *et al.* have demonstrated the applicability and accuracy of their method for step-index circular core fibres for the purpose of analyzing directional couplers and coupler half-blocks (side-polished fibre blocks). Here we apply Sharma's method to elliptical core fibres, in particular to step-index elliptical core fibres with an undoped circular region at the centre of their cores (the vapour spot) as described in Section 2.3.1.

The modal fields of the D-fibre are first approximated by a trial function which is used to determine the core-cladding index difference of the EPW. The modal field of the fibre is chosen to be of the following form [35]:

$$\psi(x,y) = \psi_x(x)\psi_y(y) \tag{2-3}$$

where $\Psi(x,y)$ is the modal field of the D-fibre and Ψ_x and Ψ_y are scalar modes of the two slabs with index variations in the x and y directions, respectively.

The functional form of Ψ_x is chosen to be [35]

$$\psi_x(x) = \begin{cases} A\cos(p_x x/b), & |x| \le \sigma_x b \\ A\cos(p_x\sigma_x)e^{-p_x\tan(p_x\sigma_x)\{x/b-\sigma_x\}} & |x| \ge \sigma_x b \end{cases} \tag{2-4}$$

and the functional form of Ψ_y is chosen to be

$$\psi_y(y) = \begin{cases} B\cos(p_y y/a), & |y| \le \sigma_y a \\ B\cos(p_y\sigma_y)e^{-p_y\tan(p_y\sigma_y)\{y/a-\sigma_y\}} & |y| \ge \sigma_y a \end{cases} \tag{2-5}$$

where a and b are the semimajor and semiminor axis, respectively, of the elliptical core, p_x, p_y, σ_x, and σ_y are adjustable parameters, suitable values of which are obtained by maximizing the stationary expression for the propagation constant, β,

$$\beta^2 = \frac{\int_{-\infty}^{\infty}\int_{-\infty}^{\infty}\left[k_o^2 n^2(x,y)|\psi(x,y)|^2 - |\nabla\psi(x,y)|^2\right]dx\,dy}{\int_{-\infty}^{\infty}\int_{-\infty}^{\infty}|\psi(x,y)|^2\,dx\,dy} \tag{2-6}$$

where k_o is the free space propagation constant and $n(x,y)$ is the refractive index distribution of the fibre to be replaced.

The forms of the fields chosen for Ψ_x and Ψ_y are such that they correspond exactly to the scalar modal fields of some slab waveguides which can be defined once p_x, p_y, σ_x, and σ_y are known. Substitution of $\Psi(x,y)$ from equations (2-3), (2-4) and (2-5) into equation (2-6) leads to an expression for β^2 in terms of p_x, p_y, σ_x, and σ_y. The value of β^2 is then maximized with respect to p_x, p_y, σ_x, and σ_y. Keeping in mind that the direction of interaction of the D-fibre modal field with the external medium is in the x-direction, it is the x-slab, thus arrived at, that is used to create the four-layered leaky structure to be analyzed using the equations laid out in [39], which have not been repeated here.

Since Ψ_x corresponds to the exact scalar mode of a step-index slab, the x-slab is defined as [35]

$$n_x(x) = \begin{cases} n_{x1}, & |x| < \sigma_x b \\ n_{x2}, & |x| > \sigma_x b \end{cases} \tag{2-7}$$

such that $\Psi_x(x)$ is the solution of the corresponding scalar wave equation

$$\frac{d^2\psi_x(x)}{dx^2} + \left[k_o^2 n_x^2(x) - \beta_x^2\right]\psi_x(x) = 0 \tag{2-8}$$

where β_x is the corresponding propagation constant. The core-cladding index difference $(n_{x1}^2 - n_{x2}^2)$ can be completely deduced from the variation of the field itself and is given as [35]

$$\left(n_{x1}^2 - n_{x2}^2\right) = \frac{p_x^2 \sec^2(p_x \sigma_x)}{k_o^2 b^2} \tag{2-9}$$

The absolute values of n_{x1} and n_{x2} cannot be determined from the field variation itself. However, the value of n_{x1} can be determined by imposing one more condition for equivalence between the fibre and its EPW: the condition that their longitudinal propagation constants be matched. Thus far, the transverse phase constant, p_x, of the x-slab has been matched to the transverse phase constant of the fibre mode along the x-axis, i.e., the evanescent tail of the x-slab mode closely matches the evanescent tail of the fibre mode. Making the longitudinal propagation constant of the x-slab mode equal to that of the fibre mode, makes the x-slab equivalent to the fibre in both field variation and propagation characteristics as far as interactions across the y-z plane are concerned. With this additional condition, the equivalent x-slab then has an index distribution given as [35]

$$n_x^2(x) = \begin{cases} n_{x1}^2 = n_{co}^2 - \left(U^2 - p_x^2\right)/\left(k_o b\right)^2, & |x| < \sigma_x b \\ n_{x2}^2 = n_{x1}^2 - p_x^2 \sec^2\left(p_x \sigma_x\right)/\left(k_o b\right)^2 & |x| > \sigma_x b \end{cases} \tag{2-10}$$

where $U = b\sqrt{k_o^2 n_{co}^2 - \beta_f^2}$, β_f is the propagation constant of the fibre mode, n_{co} and n_{cl} are the core and cladding refractive indices of the fibre, respectively.

Figure 2-3 shows a cross section of a step-index elliptical core D-fibre immersed in an external medium. Shown also is the elliptical core with a cladding limited by a plane along with its EPW. Equation (2-6) can be split into three different integral equations:

$$I_1 = \int_{-\infty}^{\infty}\int_{-\infty}^{\infty} k_o^2 n^2(x,y)\left|\psi(x,y)\right|^2 dx\, dy \tag{2-11}$$

$$I_2 = \int_{-\infty}^{\infty}\int_{-\infty}^{\infty} \left|\nabla\psi(x,y)\right|^2 dx\, dy \tag{2-12}$$

$$I_3 = \int_{-\infty}^{\infty}\int_{-\infty}^{\infty} \left|\psi(x,y)\right|^2 dx\, dy \tag{2-13}$$

where I_1 needs to be evaluated numerically and I_2 and I_3 can be evaluated analytically. The results of optimizing equation (2-6) for the D-fibre described in Section 2.3.1 are shown in Table 2-1. Shown are the values determined for p_x, p_y, σ_x, and σ_y for several values of the elliptical core's semiminor axis, b. Shown also are the optimized values of β, given as the effective mode index, $n_{eff} = \beta/k_o$. As will be seen, these values for n_{eff} agree well with those determined using commercially available waveguide analysis software, indicating that the fibre mode propagation constant is well matched to that of its equivalent planar waveguide.

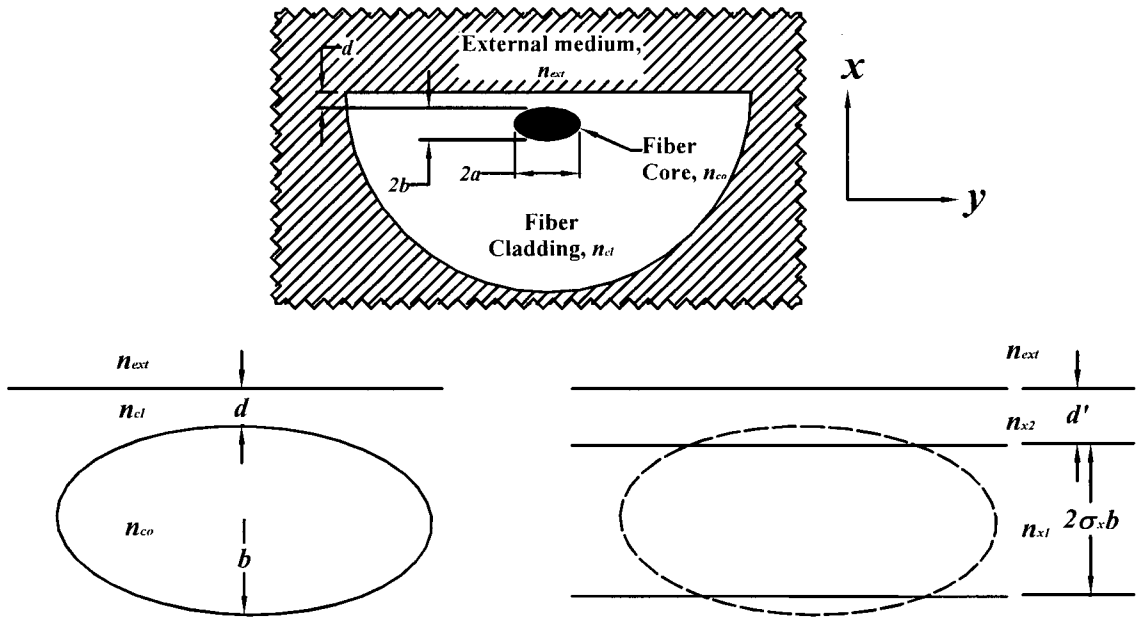

Figure 2-3: Cross section of a step-index elliptical core D-fibre (not to scale) immersed in an external medium. Elliptical core with a cladding limited by a plane along with its EPW and their respective refractive index distributions.

Table 2-1: Results of optimization of equation (2-6) with respect to p_x, p_y, σ_x, and σ_y for several values of semiminor axis b.

b	p_x	p_y	σ_x	σ_y	$n_{eff} = \beta/k_o$
0.85	0.738957	1.073373	0.933845	0.903210	1.448319
0.90	0.765567	1.076929	0.933364	0.909309	1.448889
0.95	0.787560	1.076706	0.939305	0.917884	1.449443
1.00	0.809221	1.080367	0.943008	0.921504	1.449913
1.05	0.832298	1.082729	0.938277	0.922409	1.450371

Using the values in Table 2-1, the EPW can be defined and the equations in [39] can be used to compute the power attenuation coefficient of the leaky mode of the four-layer planar waveguide structure. The power attenuation coefficient has been used in equation (2-2) to calculate the power transmission ratio for a one-centimetre etched section of the D-fibre used in this work as a function of the external refractive index, n_{ext}, for several values of the etched cladding thickness d at λ_o = 1550 nm, and is shown in Figure 2-4.

The power transmission ratio has three regions of operation, separated by the vertical dotted lines in Figure 2-4. In Region I, where $n_{ext} \gtrsim n_{eff}$, the power transmission decreases sharply to a minimum and the slope is large and negative over a small refractive index range, leading to a high sensitivity to changes in n_{ext}. This behaviour is consistent with the leaky mode behaviour described earlier, i.e., for $n_{ext} > n_{eff}$, the mode becomes leaky and power is radiated out of the core. In Region II where $n_{ext} > n_{eff}$, the transmission is close to its minimum and its slope is small or even zero, leading to a small or even zero sensitivity to changes in n_{ext}. In Region III, where $n_{ext} > n_{eff}$ as well, the transmission increases monotonically and the slope is positive over a large refractive index range and a moderate sensitivity to changes in n_{ext}. Thus, depending on the application and the required sensitivity, one of the three regions can be used to realise an intensity-based fibre optic sensor. It should be noted that the propagation constant of the mode in the fibre is also changed for $n_{ext} < n_{eff}$, but remains real and thus the mode is not leaky. The boundaries for the three regions have been selected subjectively based on the descriptions given above for each region. However, a quantitative approach can be used which could be based on a minimum or threshold sensitivity value.

Since the direction of interaction is along the x-axis, of the two elliptical core dimensions, the semiminor axis, b, plays a role in determining the transverse phase constant of the EPW. The power transmission ratio has been calculated for d = 4.5 μm for several values of b and is shown in Figure 2-5. It is evident that changes in the semiminor axis have a significant effect on the

power transmission ratio. This is to be expected as the extent of the penetration of the evanescent tail into the external medium depends on b.

The optimization of equation (2-6) required numerical integration as well as optimization with respect to the four parameters, p_x, p_y, σ_x, and σ_y. This was resource intensive and typically took 3-4 hours per optimization. As will be demonstrated in Chapter 3, Sharma's formulas for determining the EPW for step-index circular fibres can be applied to the D-fibre with an additional modification. Nevertheless, to verify the model presented here, the next section shows results of simulations conducted using a commercially available waveguide modelling software package called BeamPROP™.

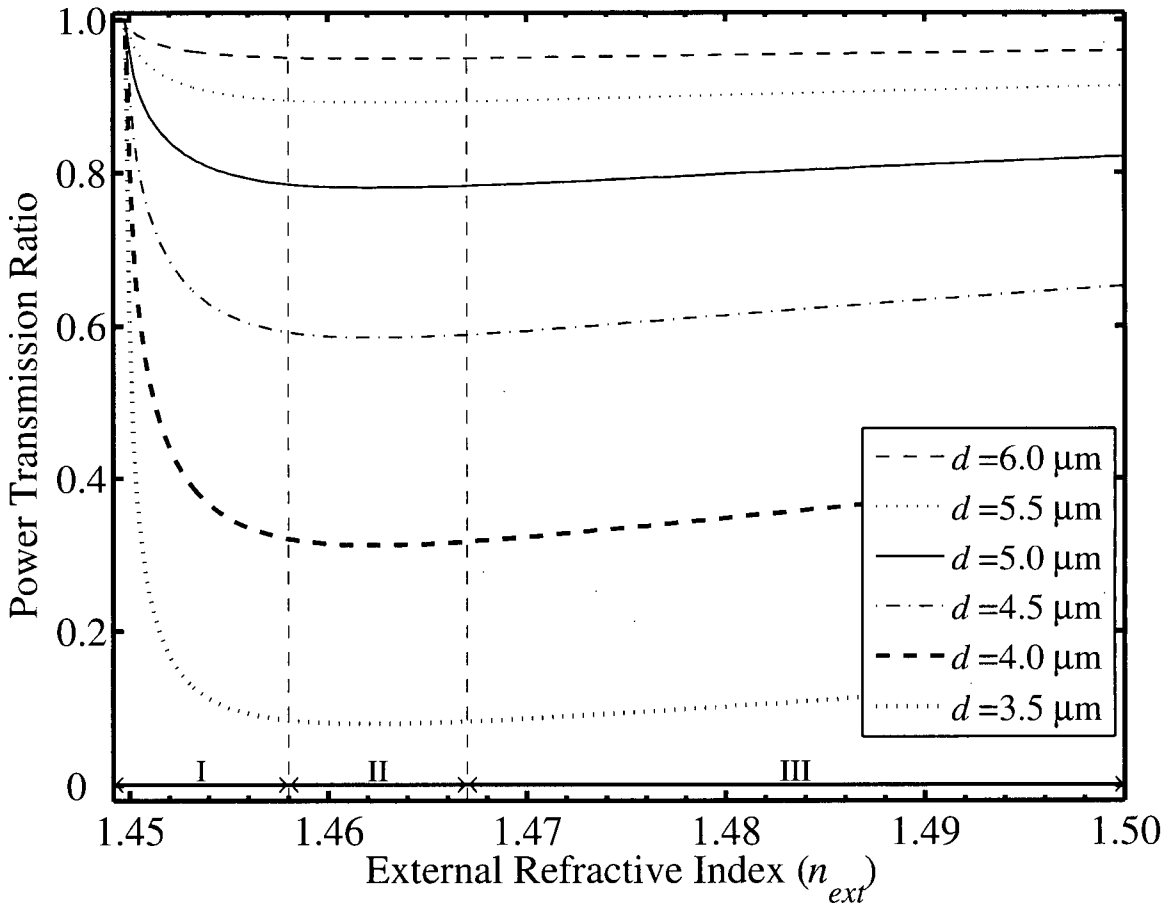

Figure 2-4: Calculated power transmission ratio for the four-layer equivalent planar waveguide structure's leaky TE_0 mode versus n_{ext} for several values of d using $a = 2$ μm, $b = 1$ μm and $L = 1$ cm at $\lambda_o = 1550$ nm. Vertical dotted lines separate Regions I, II, and III.

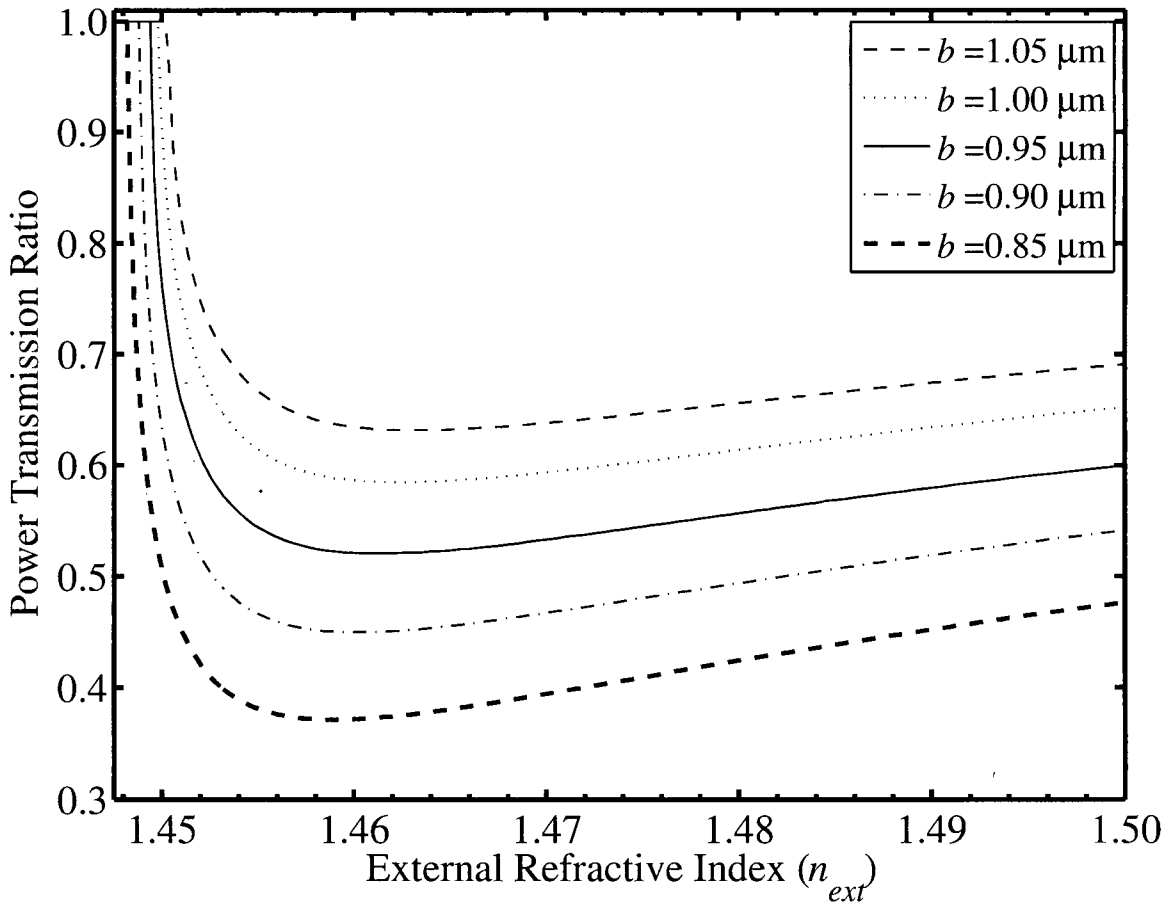

Figure 2-5: Calculated power transmission ratio for the four-layer equivalent planar waveguide structure's leaky TE_0 mode versus n_{ext} for several values of b using $a = 2$ μm, $d = 4.5$ μm and $L = 1$ cm at $\lambda_o = 1550$ nm.

2.5 Software Modelling of D-fibre

Due to the non-ideal nature of many practical waveguide structures, typical analytical solutions to common waveguide geometries are often not sufficient to describe their behaviour. In many cases, numerical simulations based on methods such as beam propagation, finite difference, or finite element methods are required. This section describes how a commercially available waveguide modelling software package based on the beam propagation method, BeamPROP™, was used to model the D-fibre with an external medium present. Power transmission ratio curves similar to those presented in the previous section were obtained, further validating the theoretical model described in the previous section.

BeamPROP™ allows the creation of waveguide structures with user defined refractive index distributions. Thus, the effective index and the field distribution of the fundamental ${}_oHE_{11}$ mode of the D-fibre described in Section 2.3.1 (with air as the external medium and a large cladding thickness) could be obtained. The mode effective index of the D-fibre's fundamental ${}_oHE_{11}$ mode with the vapour spot included is tabulated in Table 2-2 along with those determined using Sharma's model, demonstrating that the differences are negligible. To model the leaky structure, an external medium was added to the refractive index distribution.

Table 2-2: Mode effective indices for the fundamental ${}_oHE_{11}$ mode of the D-fibre with elliptical core including vapour spot determined using BeamPROP™ and Sharma's model for several values of the semiminor axis, b.

b	n_{eff} (β/k_o) BeamPROP™	n_{eff} (β/k_o) Sharma
0.85	1.448184	1.448319
0.90	1.448817	1.448889
0.95	1.449425	1.449443
1.00	1.450006	1.449913
1.05	1.450564	1.450371

The computed ${}_oHE_{11}$ mode field distribution (using BeamPROP™) was 'launched' into the waveguide structure and the power along the fibre was calculated by determining the overlap integral between the launched mode and the propagated mode along the fibre length (automatically done by BeamPROP™). The power as a function of propagation distance along the length of the fibre was then fit to an exponential function (equation (2-2)) to determine the power attenuation coefficient. This was done for several values of d and b to produce the power transmission ratio curves shown in Figure 2-6 and Figure 2-7. It is evident that the curves

calculated using the results from BeamPROP™ are similar to those obtained using Sharma's model.

To demonstrate the validity of both models, the transmission ratio curves obtained using both Sharma's model and BeamPROP™ are shown on a single plot in Figure 2-8 for three values of the cladding thickness. The curves with circles are those obtained using BeamPROP™. The discrepancies between those obtained using Sharma's model and those obtained using BeamPROP™ can be attributed to the fact that Sharma's model attempts to approximate the modal fields of the elliptical fibre using those of slab structures and thus is not exact. Also, the accuracy of the results in BeamPROP™ depends on the grid sizes used and a trade-off between computation time and accuracy is required. As will be seen later in Section 3.4, modifications are made to Sharma's model so that the calculated curves match those that are obtained experimentally. It is preferable to use an analytical model as opposed to software simulations as the simulations are resource intensive and time consuming. For example, using a grid size of 0.1 μm in the simulations, each point on the transmission curve takes approximately 10 minutes to compute. In addition, the results obtained using BeamPROP™ are sometimes inaccurate as can be seen the lack of smoothness of the curves.

2.6 Conclusions

In this chapter, the operating principles of the sensor were presented. An analytical method and software package were used to illustrate the behaviour of the sensor. It was found that both methods were able to describe the general behaviour of the sensor with regards to its regions of operation and effects of the cladding thickness and semiminor axis of the fibre's core. Power transmission ratio curves obtained using both methods showed similar trends. However, simulations using BeamPROP™ required up to 10 minutes per point and thus it was preferable to use the analytical method to predict the response of the fibre.

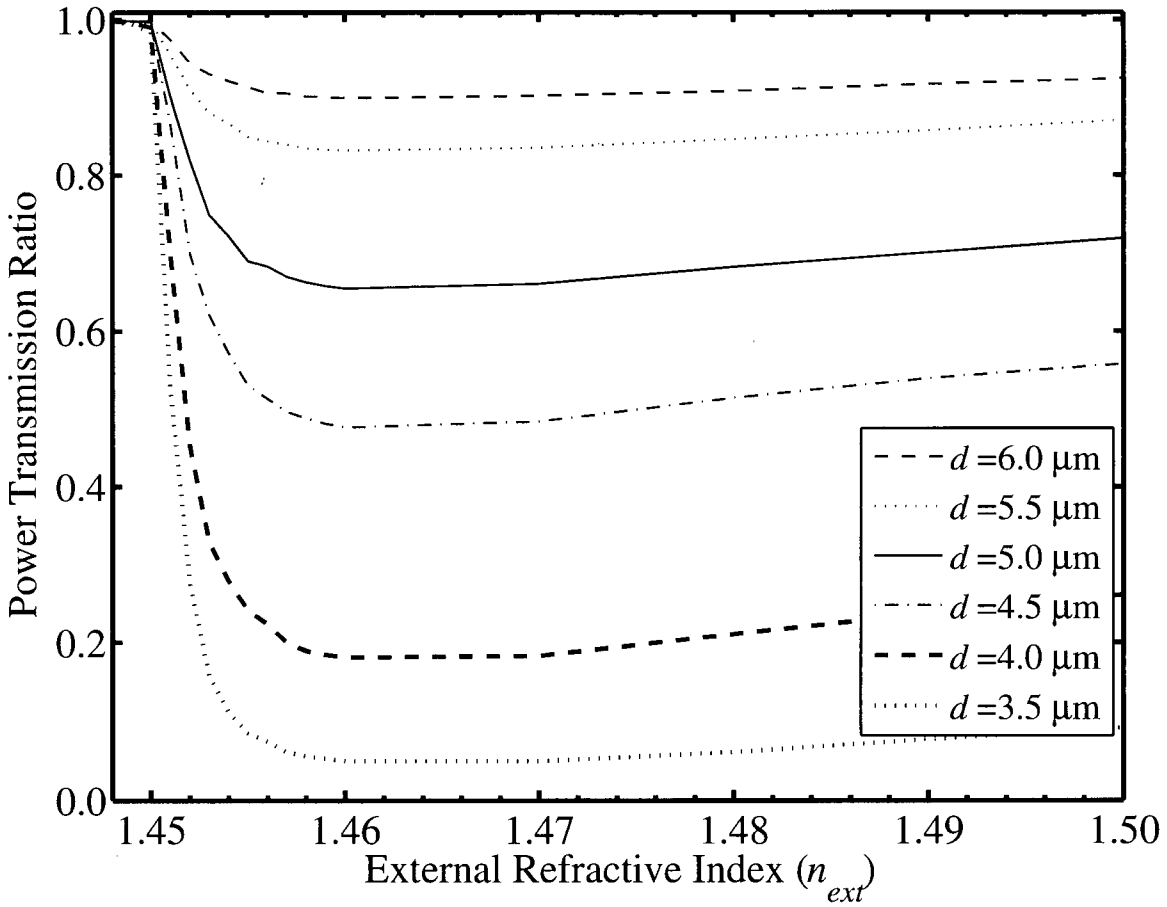

Figure 2-6: Simulated power transmission ratio of the ${}_oHE_{11}$ mode of a step-index elliptical core D-fibre, with vapour spot, versus n_{ext} for several values of d using $a = 2$ μm, $b = 1$ μm and $L = 1$ cm at $\lambda_o = 1550$ nm.

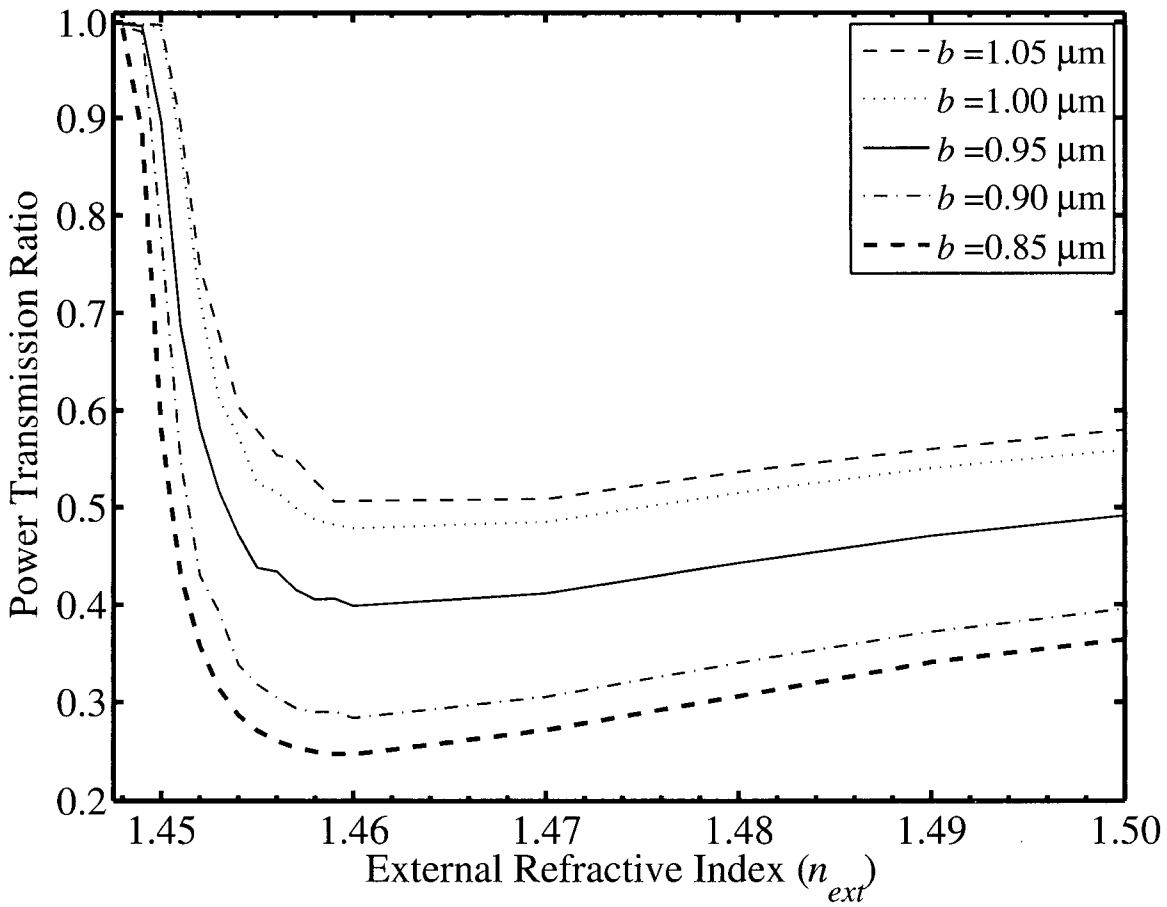

Figure 2-7: Simulated power transmission ratio of the ${}_{o}HE_{11}$ mode of a step-index elliptical core D-fibre, with vapour spot, versus n_{ext} for several values of b using $a = 2$ μm, $d = 4.5$ μm and $L = 1$ cm at $\lambda_o = 1550$ nm.

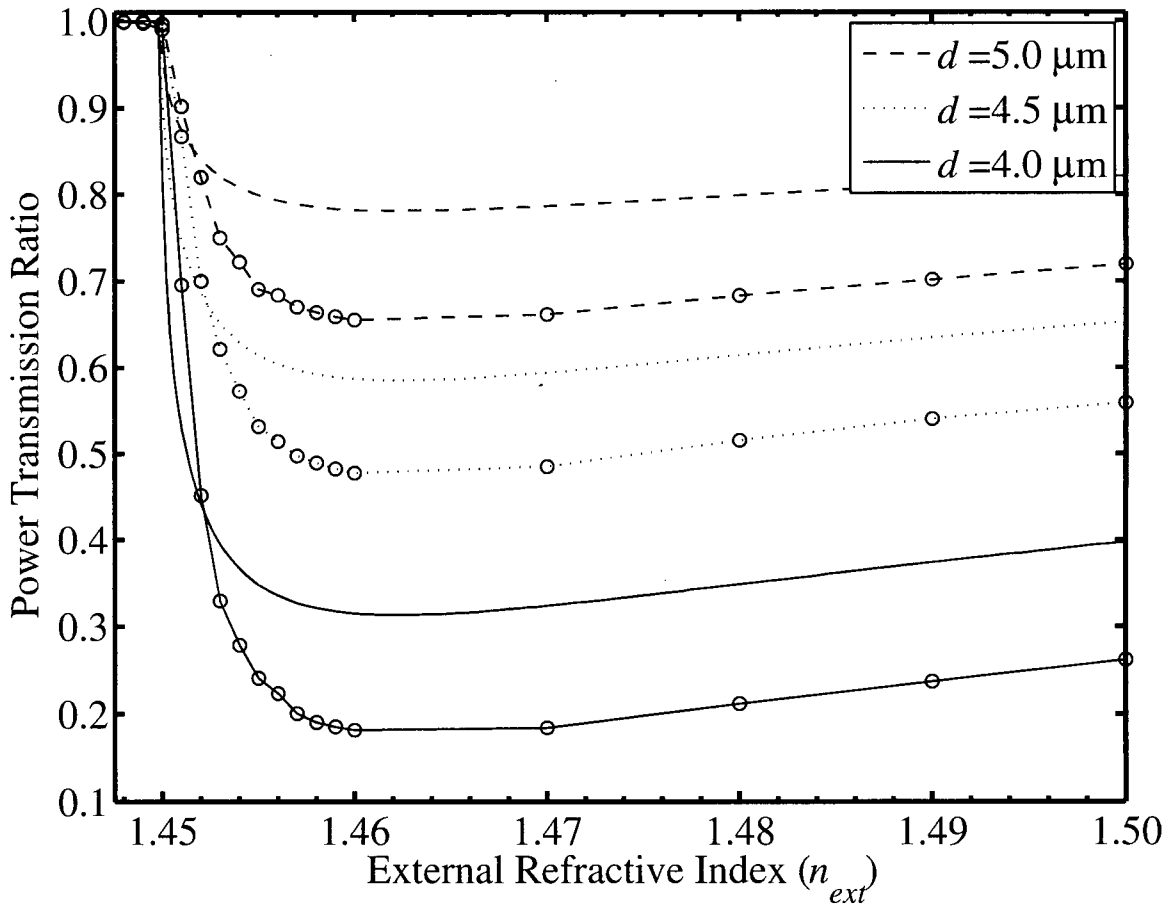

Figure 2-8: Calculated power transmission ratio for the four-layer equivalent planar waveguide structure's leaky TE_0 mode versus n_{ext} using Sharma's model and simulated power transmission ratio of the ${}_0HE_{11}$ mode of a step-index elliptical core D-fibre, with vapour spot, using BeamPROP™ versus n_{ext} for three values of d using $a = 2$ μm, $b = 1$ μm and $L = 1$ cm at $\lambda_o = 1550$ nm Curves with circles are those obtained using BeamPROP™.

Chapter 3

3 Fabrication and Experimental Setup

3.1 Introduction

In this chapter we present details on the fabrication of the sensors, the experimental setup and a technique to determine the etched cladding thickness. Section 3.2 gives details on how the fibres are etched and the steps involved. Section 3.3 describes the experimental setup used to measure the power transmission ratio of the etched fibres. Section 3.4 describes a method to determine the etched cladding thickness in a "non-destructive" manner.

3.2 Sensor Fabrication

To fabricate a sensor, a section of D-fibre is etched to reduce its as-manufactured cladding thickness. The fibres have an acrylate coating jacket that is approximately 250 μm in diameter. To expose the fibre, the coating is removed over the section to be etched. Unlike typical fibres, this coating is not attached to the fibre and can slide off of the fibre as there is a gel like substance between the coating and the fibre. Typically a 30-40 cm piece of fibre is cut from the spool and used to fabricate a sensor. The coating is scored at the centre of this fibre piece using a standard 250 μm fibre stripper. Once this is done, the fibre piece is gripped on either side of the score and, with minimal force, the coating is pulled back to expose a fibre section to be etched. The length that is exposed for etching depends on the type of sensor being fabricated.

Before etching, the gel like substance is cleaned off of the fibre. To do this, the exposed section of the fibre piece is dipped in acetone for about twenty minutes. To dip the exposed section in the acetone, and subsequently into a hydrofluoric acid solution for etching, special holders were fabricated to accommodate the fibre pieces. Several such holders were made so that several fibre pieces could be cleaned and etched simultaneously. Figure 3-1 shows a photo of a holder with a fibre in it. The holders are then lowered into a beaker so that the exposed sections of the D-fibres are immersed in the acetone as shown Figure 3-2. We have verified that the hydrofluoric acid does not attack the coating and thus accurate lengths of fibre can be etched by exposing the correct length.

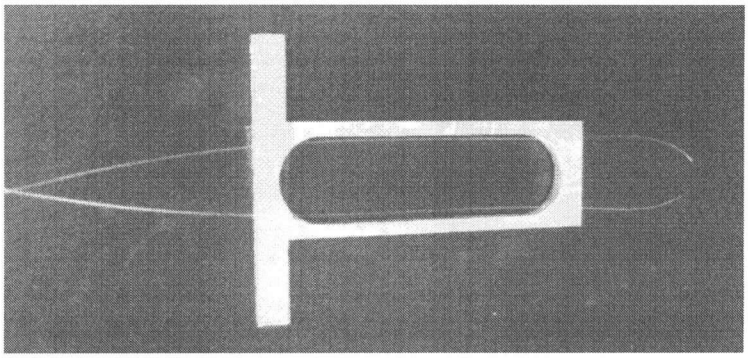

Figure 3-1: Photo of special holders fabricated to hold the D-fibre pieces for immersion in acetone or hydrofluoric acid

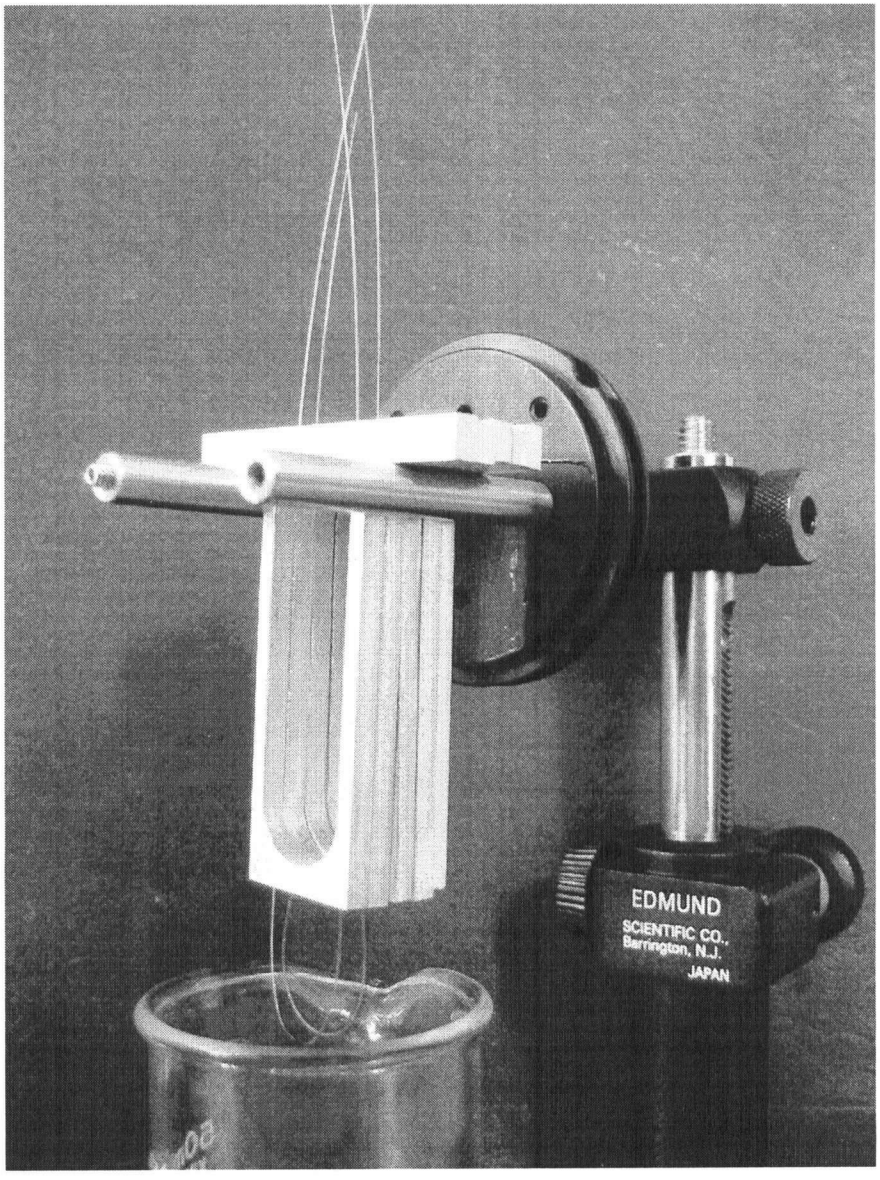

Figure 3-2: Photo of fabricated fibre holders for immersing exposed sections into acetone

Once the fibres are cleaned, the holders containing the fibres are transferred into a different beaker containing a 10% buffered hydrofluoric acid (BHF) solution. The holders are lowered into the beakers so that the exposed sections are immersed in the BHF solution. The fibres are then etched for a specific time, usually between 130 to 200 minutes, depending on the cladding thicknesses desired. The etch rate depends on the acid concentration, doping of the cladding material, temperature, and fibre batch [40]. Due to these variables, timed etches are not reliable. Instead, an accurate method is required to determine the cladding thickness of such etched fibres and will be addressed later in this chapter. Once the desired etch time is completed, etching is halted by immersing the sections in deionised water.

To use the etched fibre as a sensor, its two ends need to be cleaved in order to couple light into and out of it. Standard commercially available fibre cleavers are made to fit circular fibres with standard diameters of 125 μm. Thus, to cleave the D-fibre, the fibre has to be mounted into the cleaver so that the flat of the fibre is perpendicular to the cleaver's blade. To rotate the fibre, it is mounted in to a fibre chuck with a rotatable holder. This allows for the fibre to be rotated along its axis. Figure 3-3 shows a photo of the chuck and a fibre placed in the cleaver. This cleaving process required some practice and patience and could require several attempts as it proved difficult to get the fibre flat to be exactly perpendicular to the blade. Once cleaved, the ends were inspected under an optical microscope to ensure that they were optically flat. Figure 3-4 shows a conceptual diagram of the D-fibre with a section of length L etched to act as the sensor head.

3.3 Experimental Setup

To measure the power transmission ratio of the fibre, light needs to be coupled into and out of the fibre. The polarization state of the light is also a major consideration as, in our sensors, only one of the modes of the fibre is to be launched. Ideally, a repeatable and relatively quick method to achieve this coupling is required due to the number of sensors fabricated. Several methods are available to do this:

1) connectorization – attaching a standard fibre optic connector on to the end
2) end fire coupling – focusing a collimated beam onto the fibre core
3) butt coupling – physical connection of the D-fibre end to a standard fibre end
4) splicing – fusion or mechanical splicing of the fibre to a standard circular fibre

Except for connectorization, all the above methods were tried and resulted in varying performance in terms of the coupling coefficient and stability. Connectorization was not

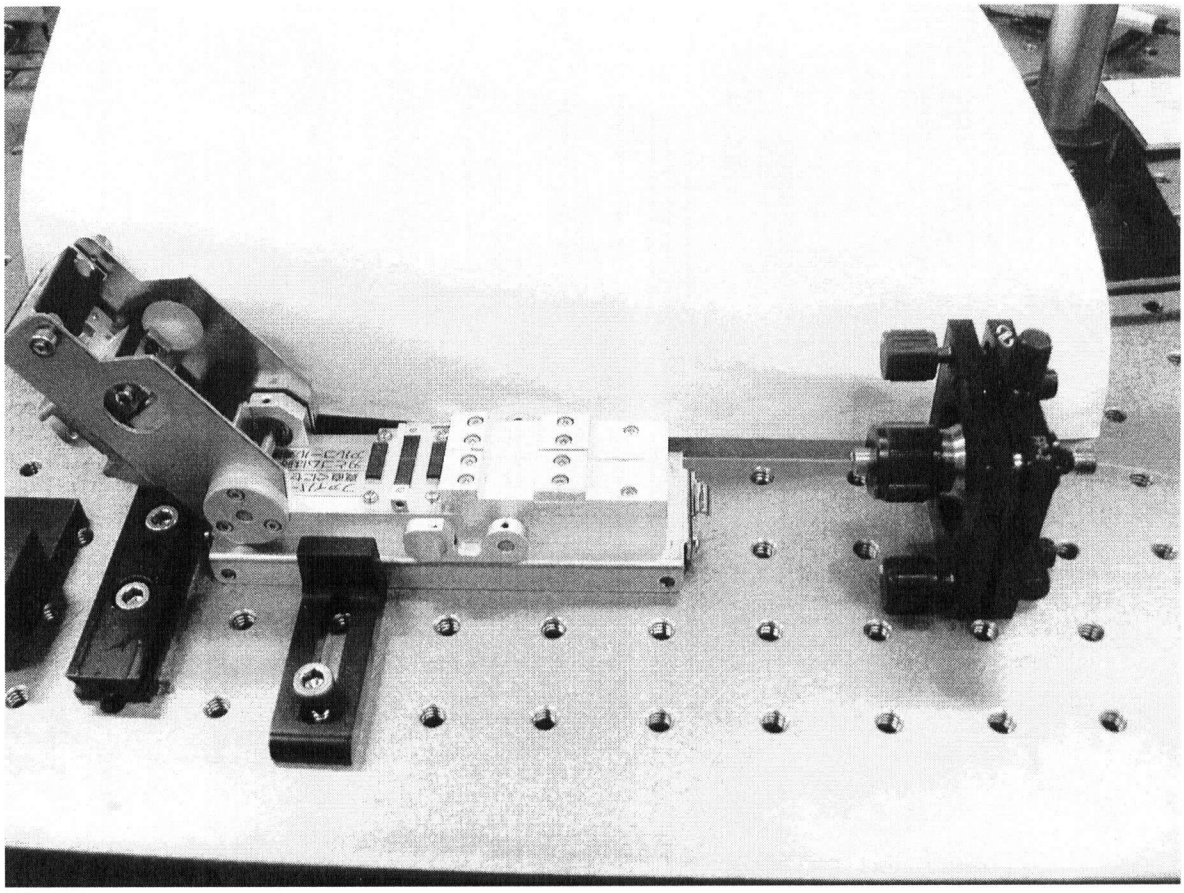

Figure 3-3: Photo of fibre in a rotatable chuck, allowing rotation along its axis, inserted into a fibre cleaver

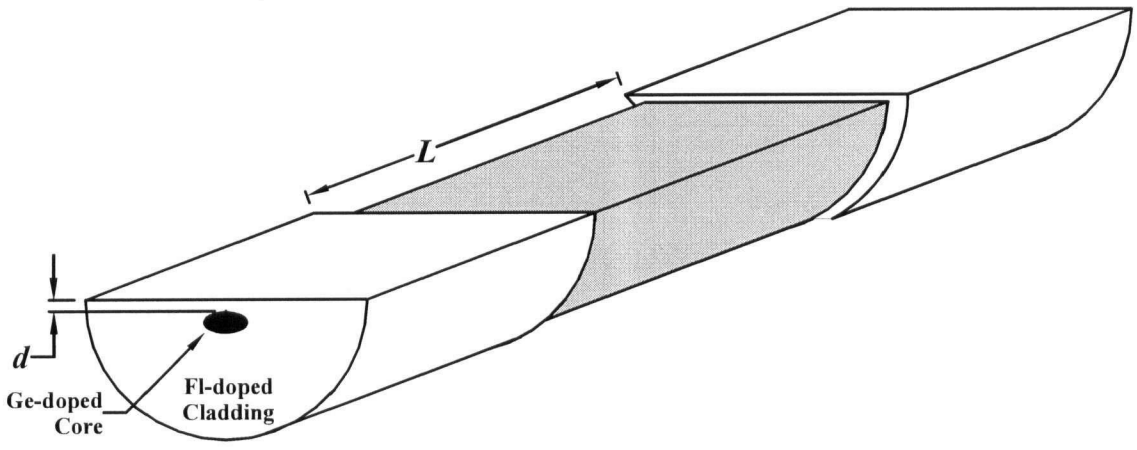

Figure 3-4: Conceptual diagram of D-fibre with a section of length L etched to act as the sensor head.

attempted due to the non-standard size of the D-fibre and due to the time and effort required to connectorise each sensor.

With end fire coupling, a nanopositioner was used along with a fibre collimator and lens to focus the beam to a spot size less than 5 μm. The resolution of the nanopositioner was 50 nm. Since the core size is approximately 2 by 4 μm, even small movements on the order of ~50 nm significantly affected the coupling coefficient. End fire coupling is not a trivial task due to the small spot sizes involved and initial alignment requires a considerable effort. Here, a coupling coefficient of >80% was achieved. However, due to the inherent drift in the nanopositioner and unavoidable vibrations, the coupling was noisy and drifted every few minutes. Butt coupling was also investigated using a standard input fibre. This input fibre was mounted onto a nanopositioner. The end of the input fibre was brought close to the end of the D-fibre and, using a microscope, the two ends were butted against each other. Index matching gel was then placed on the joint to enhance the coupling. In this case, a coupling coefficient of >70% was achieved but suffered the same limitations as end fire coupling, i.e., drift of nanopositioner and vibrations.

Splicing of the D-fibre to an input standard circular fibre is the best way to avoid drift and vibrations. A fusion splice is a non-reversible process and requires considerable effort due to the non-standard size of the D-fibre. Instead, a commercially available mechanical splice was used and is shown in Figure 3-5. These splices are reusable and are preloaded with index matching gel. They feature a glass view port enabling easy alignment of the fibres. The splices also have clamps to protect the splice against tension applied to the fibres. This method proved to be very repeatable and once an acceptable coupling coefficient was achieved, the two fibres ends were clamped in place. Coupling ratios of up to 80% were achievable and the stability was maintained over several days. Because the splices were reusable, sensors could be easily exchanged in the experimental setup. In order to launch polarized light into only one of the modes of the D-fibre (the $_{o}HE_{11}$ mode), a fibre-based polarization controller was used between the optical source and the sensor head.

Figure 3-6 shows the general experimental setup used to measure the response of the various types of sensor. The optical source used was a monochromatic laser source. The optical fibre used to guide light from the optical source through the polarization controller and then to the mechanical splice was SMF-28 fibre. The black box labelled Sensor Module was different for each sensor type, the details of which are given in the respective chapters describing each type. The output end of the D-fibre was placed in front of a large area photodetector, which was able to collect all the light exiting the fibre. The Optical Detector was comprised of the photodetector

connected to a measurement unit. All sensor modules were placed on a temperature stage which was a thermoelectric cooler that had a temperature range of 10 to 85°C. For ease and repeatability, all of the instruments were remotely controlled by a computer, using LabView™.

The polarization state of the light entering the D-fibre (i.e., at the mechanical splice) was controlled using a broadband fibre-based polarization controller (Agilent 11896A). To ensure that the correct mode of the D-fibre was launched, the polarization of the light at the output was monitored every time a new sensor was inserted into the experimental setup. This was done by collimating the beam exiting the D-fibre and measuring the extinction ratio of the light using a rotatable polarizer. By using the polarization controller, the extinction ratio at the output could be optimized. An extinction ratio in excess of 27 dB was maintained. Furthermore, the axis of the polarizer was aligned with the major axis of the elliptical core (which was parallel to the D flat) to verify that the linearly polarized light was along the major axis, i.e., the ${}_{o}HE_{11}$ mode was launched.

To measure the power transmission ratio of the etched fibre, the output power of the sensor is recorded with no external medium present, i.e., with air surrounding the sensor head. This power level is used as the reference to calculate the power transmission ratio so that, for no external medium present, $T_P = 1$. Thus, when an external medium having a refractive index greater than the mode effective index surrounds the sensor head, the power transmission ratio decreases and becomes less than one. In this way, power losses due to certain other mechanisms, such as intrinsic attenuation and absorption in the D-fibre, are normalized out. The output power was averaged for a second and data was sampled every second. With such a detection scheme, we were able to effortlessly measure the power transmission ratio with a resolution of better than 0.2%.

A typical measurement of the power transmission ratio as a function of n_{ext} was achieved using thermo-optic oils (for the electric field sensor, liquid crystals were used). The oils were obtained from Cargille Labs (Cedar Grove, NJ) which develops and manufactures optical liquids calibrated for refractive index. By changing the temperature of the oil, the refractive index can be controlled accurately. The etched section of the fibre was threaded through a specially built aluminum plate that had a trench in it. The trench was used to contain the thermo-optic oil that served as the external medium. The aluminum plate was also the cold plate of the thermoelectric cooler (TEC) used to control the temperature of the thermo-optic oil. A cover plate was placed on top of the trench so as to create an oven-like chamber to keep the temperature distribution of the oil uniform. Figure 3-7 shows a photo of the aluminum plate with a fibre immersed in oil.

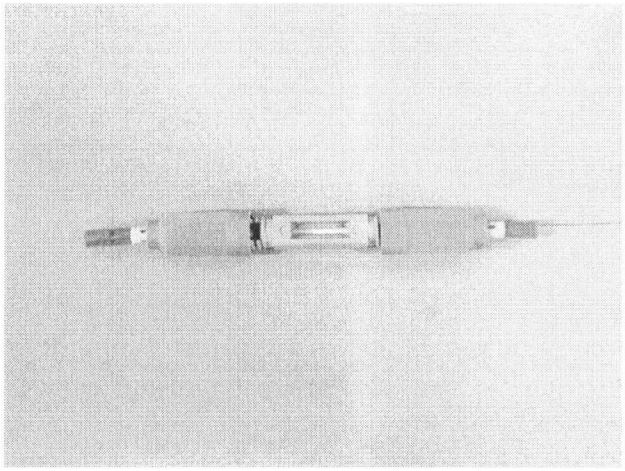

Figure 3-5: Mechanical splice used to couple light from a standard circular fibre to D-fibre.

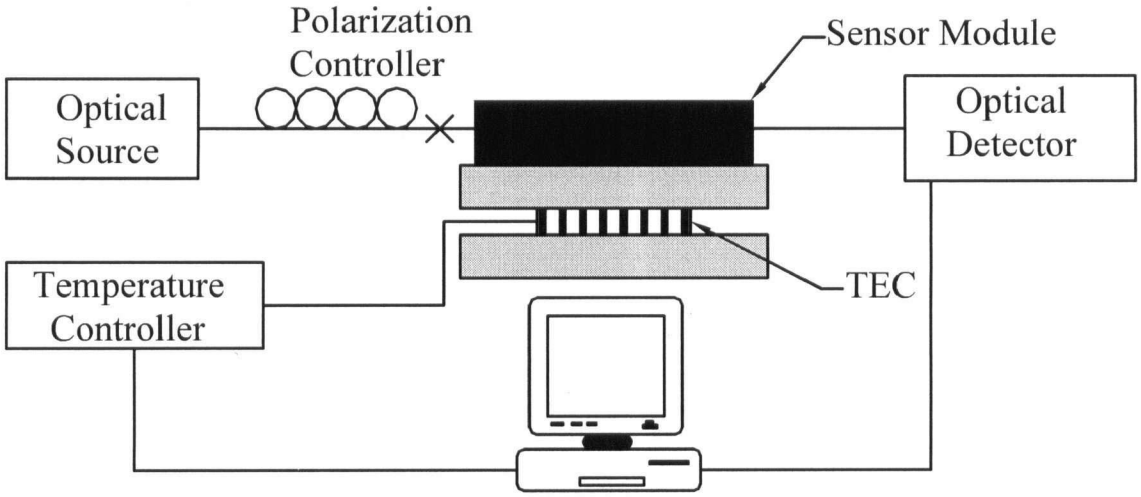

Figure 3-6: General experimental setup used to characterize various sensors. PC-polarization controller; TEC-thermoelectric controller.

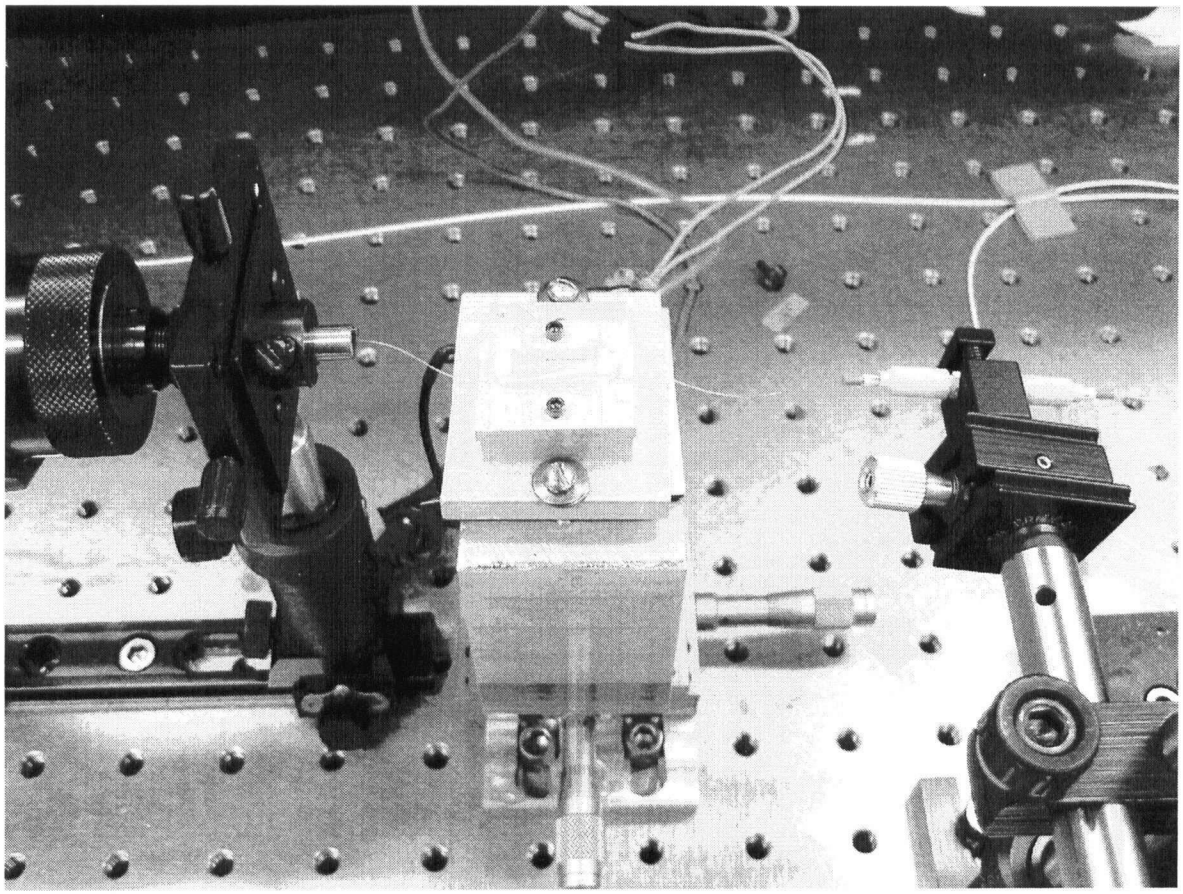

Figure 3-7: Photo of experimental setup to measure power transmission ratio with sensor head threaded through an aluminum plate and immersed in oil. Shown also are the mechanical splice at the input (right) and photodetector at the output (left).

3.4 Cladding Thickness Determination

3.4.1 Introduction

As will become apparent in subsequent chapters, the sensitivity of the sensors can be tailored by adjusting the cladding thickness. In some cases there exists an optimum cladding thickness. Thus it is essential to know the etched cladding thickness in a non-destructive manner. This section describes a novel technique developed to determine the etched cladding thickness non-destructively after a calibration is performed for a particular fibre batch or spool. It should be noted that timed etches are not reliable due to the sensitivity of the etch rate to the environment.

As mentioned in Section 2.3.1 the elliptical core fibres used in this work were not ideal step-index fibres. In addition, the refractive index distribution of the core and vapour spot were not known exactly. A model was presented in Chapter 2 and shown to be able to predict the sensor's general behaviour. However, upon comparison of the calculated power transmission ratio and the measured power transmission ratio of numerous sensors, there was a noticeable discrepancy between the slopes of the transmission ratios. The slopes of the measured transmission ratios were higher than the calculated ones, resulting in a poor fit between calculated and measured transmission ratios. To better describe the sensor's behaviour, we sought to model the fibres empirically. In doing so, we have developed a technique to determine the etched cladding thickness. Nevertheless, the model presented in Chapter 2 will be used to investigate and describe the sensors in subsequent chapters.

There have been several methods proposed to determine the cladding thickness of D-fibres and/or the polish depth of side-polished fibres. For example, several liquids having various refractive indices were dropped onto a side-polished fibre and the resulting power loss of the fibre for each liquid was fit to a model to determine the polish depth [36]. Tseng and Chen [5] performed similar measurements to those in [36] and fit their data to theory to determine the effective interaction length of their side-polished fibres. In addition to using several liquids with different refractive indices, Tseng and Chen performed a temperature ramp over 10°C at a rate of 0.15°C/min. An in-situ method was presented whereby the birefringence of a polarization-maintaining D-fibre was monitored while being etched [34]. However, this method was limited to cladding thicknesses of about 1.5 μm or less.

A version of this section has been accepted for publication. Chandani, S.M. and Jaeger, N.A.F. (2007) Modelling of elliptical core D-fibers for determination of cladding thickness in Proc. of SPIE (6 pages).

In the technique developed in this work [41], [42], the measured power transmission ratio of the D-fibre immersed in a thermo-optic oil at three temperature points is fit to a theoretical model that is based on a simple modification made to Sharma's model [35]. The modification is made to account for the particular D-fibre's actual refractive index distribution. We use an empirical parameter in the model obtained by fitting two measured responses for the particular fibre to the model.

3.4.2 Simplified Model

The theoretical model used is similar to that described in Section 2.4 with a few simplifications. Instead of determining the equivalent planar waveguide (EPW) of a step-index elliptical core fibre as was done in Section 2.4, the D-fibre is treated instead as a step-index circular fibre with a core radius equal to the elliptical core semiminor axis and its EPW is determined using formulas developed by Sharma for step-index circular fibres. Figure 3-8 shows a circular core with its EPW superimposed on it along with the refractive index distributions of the fibre and its EPW. Sharma's model requires that a fibre's phase constants along the direction of interaction (the x-direction, see Figure 3-8) and the direction of propagation (the z-direction) be matched with the corresponding phase constants of its EPW. As a result, of the two core dimensions of the elliptical D-fibre, only b plays a role in determining the EPW. In the four-layer waveguide, it is the tail of the evanescent field in the x-direction that interacts with the external medium. Sharma's formulas for determining the EPW for step-index circular fibres are repeated here for convenience

$$n^2(x) = \begin{cases} n_{x1}^2 = n_{co}^2 - (U^2 - p^2)/(k_o b)^2, & |x| < b\sigma \\ n_{x2}^2 = n_{x1}^2 - p^2 \sec^2(p\sigma)/(k_o b)^2, & |x| > b\sigma \end{cases} \tag{3-1}$$

where n_{x1} and n_{x2} are the refractive indices of the EPW core and cladding, respectively, b is the core radius, and

$$p^3 = 1.3528 + 1.6880V - 0.1894V^2$$
$$\sigma = 0.8404 + 0.0251V - 0.0046V^2$$

where $U = b\sqrt{k_o^2 n_{co}^2 - \beta_f^2}$, $V = k_o b\sqrt{n_{co}^2 - n_{cl}^2}$, β_f and k_o are the fibre mode and free space propagation constants, respectively, and n_{co} and n_{cl} are the fibre core and cladding refractive indices, respectively.

According to Sharma's technique, the thickness of the cladding layer of the four-layer waveguide, d', should be $d + (1-\sigma)b$ (see Figure 3-8). However, to take into account the poor match between the modal fields of the actual D-fibre and its EPW (determined using formulas

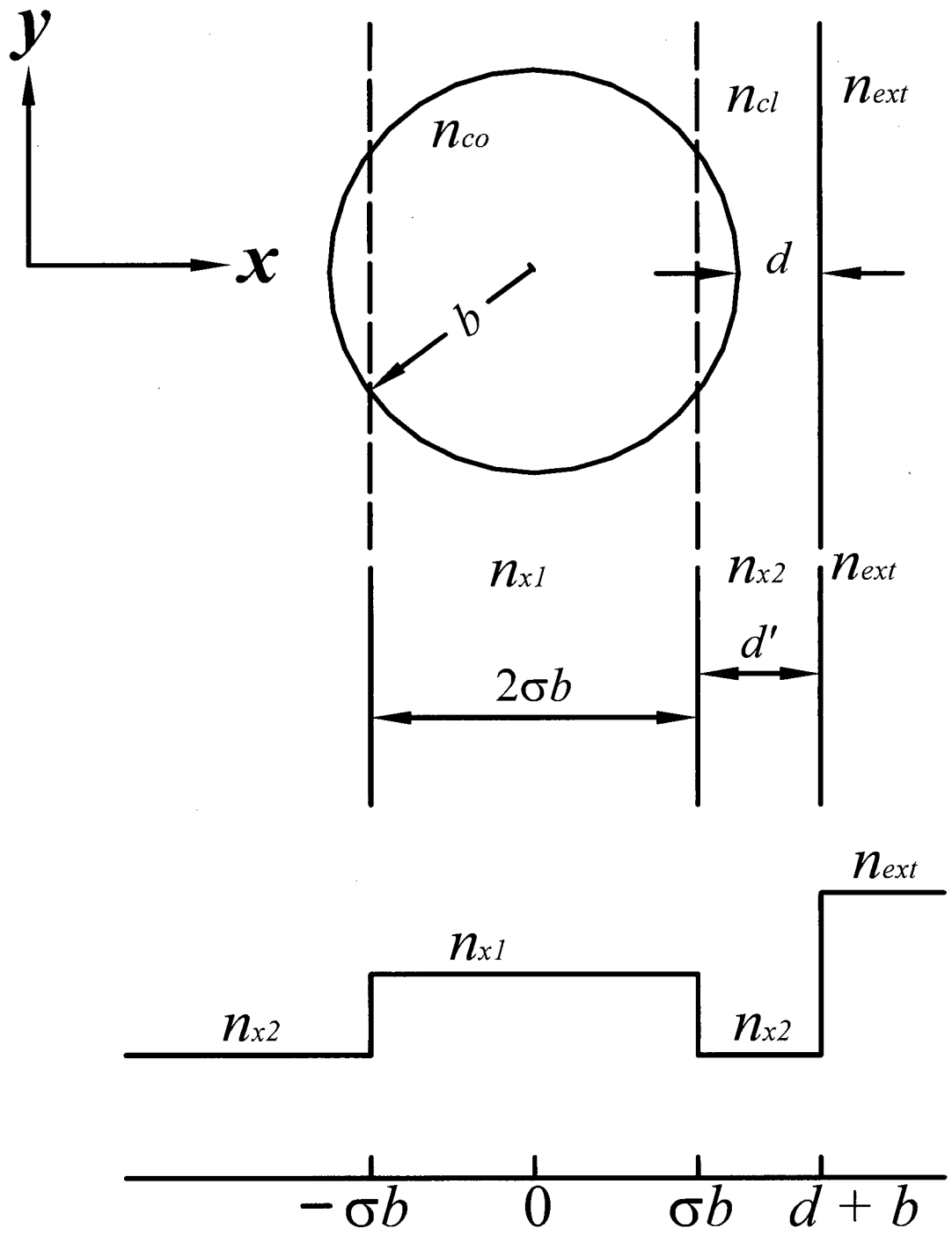

Figure 3-8: Schematic of circular core and its equivalent planar waveguide with cladding thickness d and an external medium of refractive index n_{ext}. Circular core of radius b, core and cladding refractive indices of n_{co} and n_{cl}. Equivalent planar waveguide (identified by the dashed lines) of thickness $2\sigma b$, core and cladding refractive indices of n_{x1} and n_{x2}.

for step-index circular fibre) we propose shifting the D-fibre's EPW. We propose that $d' = d + d_{shift}$, where d_{shift} is empirically determined for a particular fibre. The shift of the modal field achieves a better match between the portion of optical power that penetrates into the external medium in the model and that which penetrates into the external medium in the actual fibre. Figure 3-9 shows a schematic of an elliptical core fibre and its equivalent planar waveguide (identified by the dashed lines) with a positive shift.

Once the EPW is defined and d_{shift} is empirically determined, the fibre's power transmission ratio can be calculated as a function of d and b at a particular n_{ext}. In section 2.4, the power transmission ratio of the D-fibre was calculated for different values of cladding thickness d and shown to decrease with decreasing d for a particular n_{ext} (see Figure 2-4). The power transmission ratio was also shown to depend on the semiminor axis b (see Figure 2-5). From Figure 2-4 and Figure 2-5, it is clear that there are two important characteristics of the transmission in Region III: its value and its slope. The model described above can be used to create a lookup table of power transmission ratio values and their slopes for the range $0 < d \leq 7$ μm and $0.9 \leq b \leq 1$ μm at a particular n_{ext} for the D-fibre. This table provides a unique combination of transmission value and slope for each combination of d and b. Thus, one way of determining d and b is to measure the power transmission ratio as a function of n_{ext} in Region III and fit the response to the model, using d and b as fitting parameters.

3.4.3 Determination of d_{shift}

To determine d_{shift}, a calibration is required for the particular D-fibre used. To do this, we used the measured transmission ratio of two one-centimetre sections of D-fibre, both taken from a single longer fibre, that were etched so that each section had a different cladding thickness from the other one. In particular, we used one section with a shallow etch and one with a deep etch. To demonstrate the method, we used five such fibre sections, all taken from the same fibre. For each etched fibre, the power was measured in the absence of the thermo-optic oil. This power level was used as the reference level to calculate the power transmission ratio. The trench was then filled with the oil and its temperature changed from 15°C to 35°C in 10°C steps. The oil used had an index of refraction at 25°C, n_0, and thermo-optic coefficient, dn/dT, of 1.4710 ± 0.0005 and -3.86×10^{-4}/°C, respectively, at $\lambda_o = 1550$ nm. Thus, by measuring the power transmission ratio at $T = [15\ 25\ 35]$ °C, which corresponds to $n_{ext} = [1.475\ 1.471\ 1.467]$, the power transmission ratio, T_P, and its slope, M_P, at $n_{ext} = 1.471$ could be determined and fit to the model using d and b as fitting parameters. After measuring the sections' transmission ratios, they were cleaved through the centres of their etched regions and scanning electron microscope

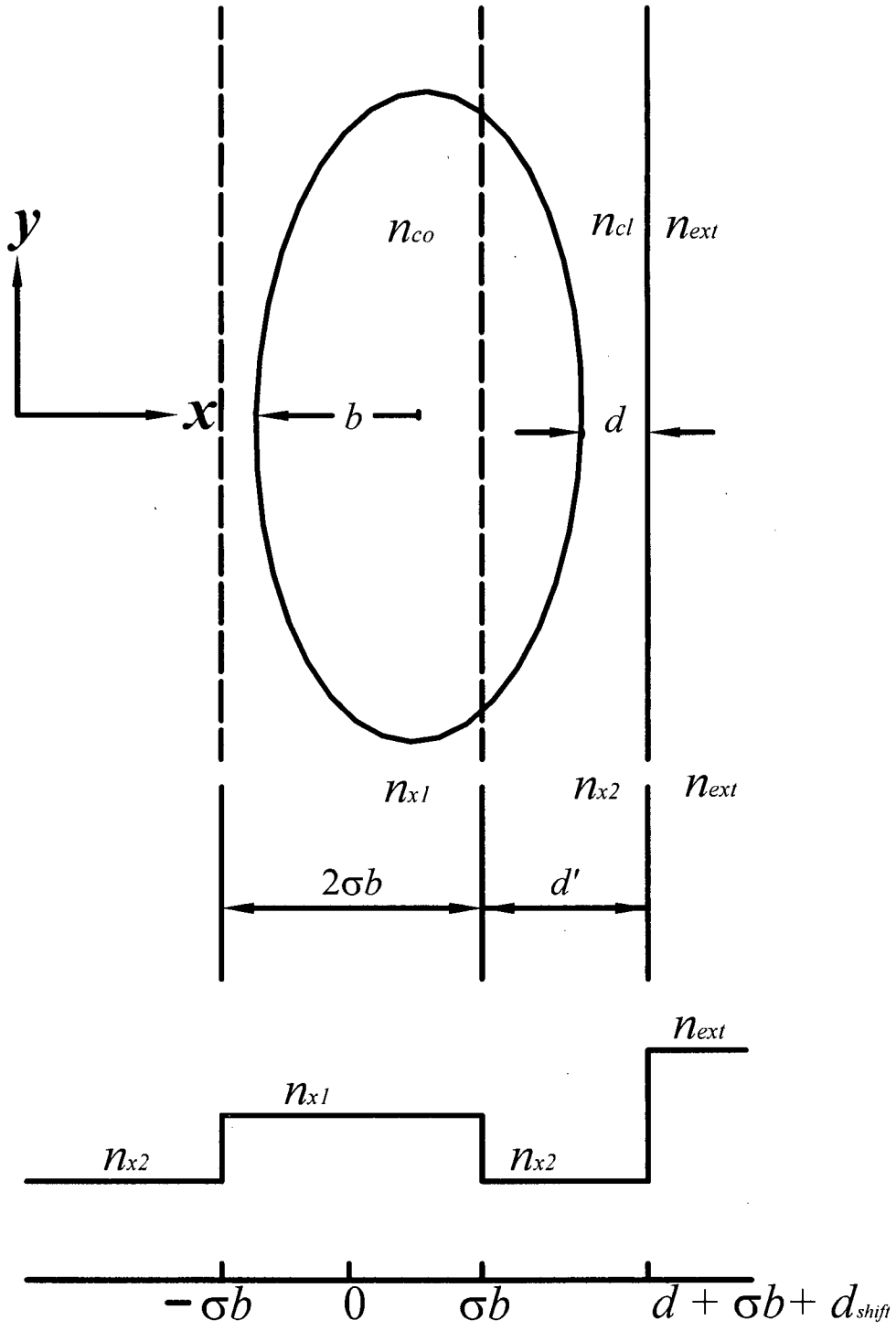

Figure 3-9: Schematic of elliptical core and its equivalent planar waveguide (identified by the dashed lines), shifted by d_{shift}, with cladding thickness d and an external medium of refractive index n_{ext}. Elliptical core of semiminor axis b, core and cladding refractive indices of n_{co} and n_{cl}. Equivalent planar waveguide of thickness $2\sigma b$, core and cladding refractive indices of n_{x1} and n_{x2}.

(SEM) images were used to determine their respective cladding thicknesses. The resulting d and b values that give the best fit, in a least squares sense, between the measured and calculated transmission ratios and their slopes are termed d_{fit} and b_{fit}. Table 3-1 shows the cladding thicknesses measured using the SEM images, d_{SEM}, the measured transmission ratios, and their slopes for the five fibre sections used to demonstrate the method presented here.

Table 3-1: Cladding thicknesses of D-fibre sections, measured transmission ratios, and slopes

Section	d_{SEM} (±0.2 μm)	T_P	M_P ($\times 10^{-4}$/°C)
S1	6.3	0.877	-5.90
S2	5.5	0.788	-9.75
S3	4.5	0.516	-16.67
S4	4.0	0.161	-13.53
S5	3.8	0.236	-12.26

To start with, we fit the measured transmission ratio and slope of each section to the model by fixing $d_{fit} = d_{SEM}$ and using b_{fit} and d_{shift} as the fitting parameters for each section. Shown in Table 3-2 are the model parameters required such that $d_{fit} = d_{SEM}$ for each section.

Table 3-2: Model parameters required to match cladding thicknesses determined using SEM images and the present model

Section	$d_{fit} = d_{SEM}$ (μm)	b_{fit} (μm)	d_{shift} (μm)
S1	6.3	0.90	1.1200
S2	5.5	0.90	1.3630
S3	4.5	0.91	1.3202
S4	4.0	0.94	0.6798
S5	3.8	1.00	0.6969

The modal fields of the D-fibre's equivalent planar waveguide depend on the semiminor axis b and thus d_{shift} is also a function of b. We use the fibre sections S1 and S5 as the calibration sections since their values for d_{SEM} are at the two extremes of the five sections, where S1 is the shallow etched section and S5 is the deep etched one. We used the d_{shift} and b_{fit} values for S1 and S5 to obtain a linear function that will give d_{shift} (in μm) for any value of b (in μm), given as

$$d_{shift} = -4.2310\,b + 4.9279 \tag{3-2}$$

With d_{shift} defined by equation (3-2), a look up table of transmission and slope values was created for $n_{ext} = 1.471$ and the transmission ratio and slope values of each of the five sections were fit to the model using b and d as fitting parameters. The results are shown in Table 3-3.

Table 3-3: Measured and calculated values for the cladding thickness using sections S1 and S5 as the calibration pair

S1 and S5 $d_{shift} = -4.2310b + 4.9279$			
Section	d_{SEM} (±0.2 μm)	d_{fit} (μm)	$\Delta d = \lvert d_{SEM} - d_{fit} \rvert$ (μm)
S1	6.3	6.3	0.0
S2	5.5	5.8	0.3
S3	4.5	4.8	0.3
S4	4.0	3.7	0.3
S5	3.8	3.8	0.0

Since we used S1 and S5 as the calibration sections, the Δd 's ($\Delta d = |d_{SEM} - d_{fit}|$) for S1 and S5 are zero and for the other three sections are 0.3 μm, demonstrating that a calibration using one shallow and one deep etched section to determine d_{shift} gives good results. Clearly there are three other possible combinations of deep and shallow etched sections that could have been used to obtain a linear function for d_{shift}. However, upon inspection of Table 3-1, it is evident that the transmission ratio values of S4 and S5 do not fit the general trend of decreasing transmission with decreasing cladding thickness. Based on modelled transmission curves, we suspect that either the measured transmission ratio, slope or cladding thickness of S4 is incorrect and will not use it as a calibration section. Table 3-4 shows the results of using S2 and S5 as the shallow and deep etch calibration section, respectively.

With d_{shift} determined for the particular D-fibre used, the etched cladding thickness of the D-fibres can be determined non-destructively using only one liquid, three temperature steps and a mathematical fitting routine. The first step in the fitting routine is to use the measured transmission ratio value and slope at 25°C and the lookup table to get starting values for d and b. In the second step, d and b are varied by 0.1 μm and 0.01 μm, respectively, around their starting values and the data are fit to the calculated values in a least-squares sense.

Table 3-4: Measured and calculated values for the cladding thickness using sections S2-S5 the as calibration pair

S2 and S5 $d_{shift} = -6.661b + 7.3579$			
Section	d_{SEM} (±0.2 μm)	d_{fit} (μm)	$\Delta d = \lvert d_{SEM} - d_{fit} \rvert$ (μm)
S1	6.3	6.4	0.1
S2	5.5	5.5	0.0
S3	4.5	4.5	0.0
S4	4.0	3.6	0.4
S5	3.8	3.8	0.0

In using b as a fitting parameter, we found that it varied between 0.90 to 1.00 μm (which is consistent with the variations that one can expect for this type of fibre). For the range of d values for our fibres, the transmission value and slope are very sensitive to b and become more sensitive as b decreases. Hence, possible variations in d and b over the 1 cm fibre lengths used here may have contributed to the differences between d_{SEM} and d_{fit}.

To further demonstrate that the simplified model presented accurately predicts the power transmission ratio, Figure 3-10 shows the measured and calculated power transmission as a function of n_{ext} for calibration section S3. The figure shows an excellent match between the measured and calculated transmission ratios in Region III. The two curves, however, deviate in Regions I and II due to the fact that the oil's thermo-optic coefficient is not accurately known at those temperatures. As mentioned earlier, this close match was not achievable using the theoretical model presented in Section 2.4.

In summary, this section presented a method for determining the cladding thickness, after being reduced by etching, in elliptical core D-fibres. The measured transmission ratio and slope of an etched fibre can be fit to a simplified model to determine its cladding thickness. An empirical parameter used in the model is first determined using two calibration sections of the fibre. We show that a shallow etch and a deep etch calibration section can be used to determine the empirical parameter, d_{shift}. Comparisons of the differences between the cladding thicknesses as measured using SEM images and those determined using the present method illustrate the effectiveness of the method presented.

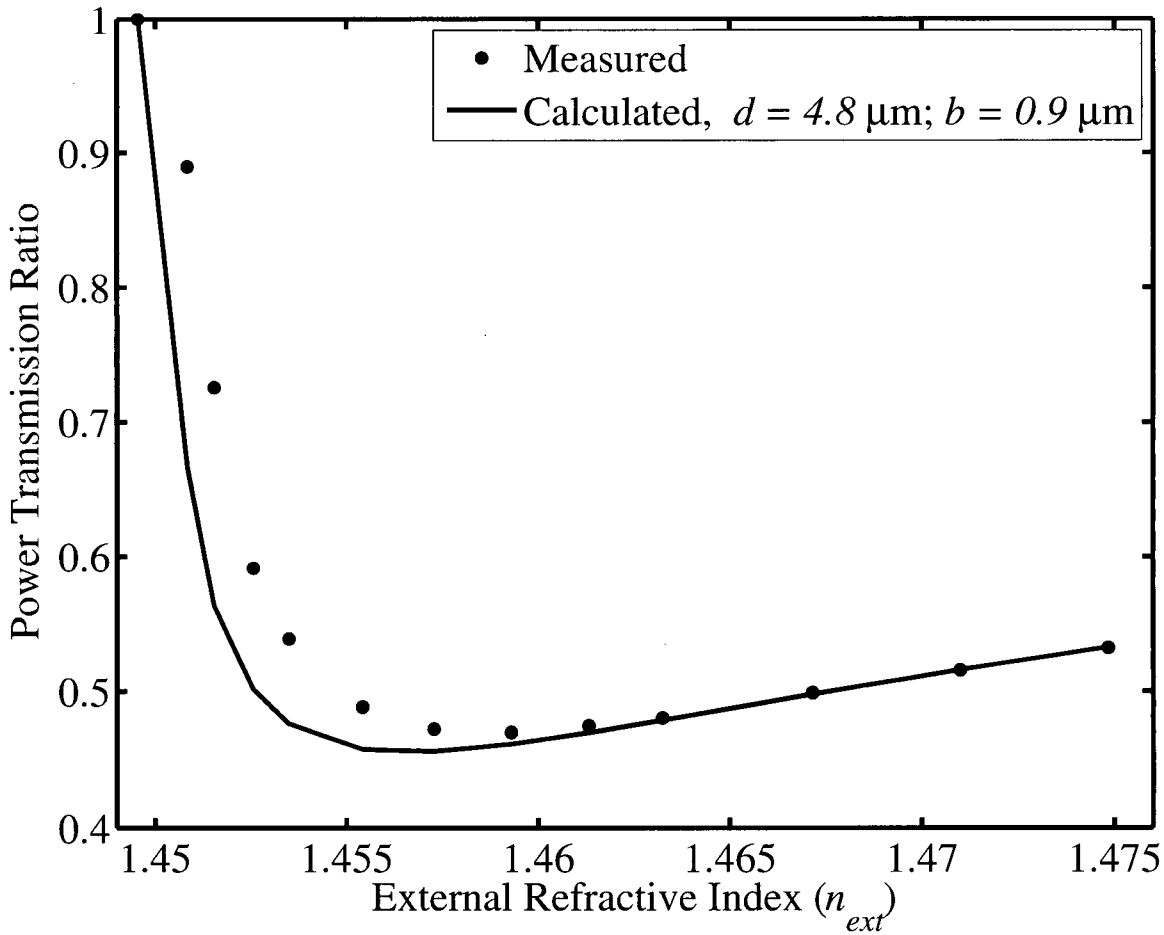

Figure 3-10: Measured and calculated power transmission ratio of calibration section S3 using simplified model which includes an empirical parameter.

3.5 Conclusions

In this chapter, the process used to fabricate a sensor and the general experimental setup were described. Etching of the D-fibre was achieved using a 10% BHF solution. The BHF does not attack the fibre's coating and thus accurate lengths of fibre could be etched. Mechanical splicing of the fibre to a standard circular fibre was found to be the best coupling technique with regard to stability. A fibre-based polarization controller was used to control the input polarization state and was capable of launching only the desired mode of the D-fibre. Finally, a novel "non-destructive" method to determine the cladding thicknesses of the etched D-fibres was presented.

Chapter 4

4 Refractive Index Sensor

4.1 Introduction

Optical fibre-based refractive index sensors are promising and attractive for use in chemical and biological sensing applications due to their inherent advantages such as chemical inertness, high sensitivity, compactness, light weight, non-intrusiveness, immunity to electromagnetic fields, and fast response times. The measurement of the refractive index of many chemical substances can be used to determine certain physical parameters, such as density, pH, acidity, and liquid concentration [43], [44]. For these reasons, there has been a significant amount of work done toward the development of optical fibre-based refractive index sensors [16], [44]-[68].

There are two common methods of measurement used in optical fibre-based refractive index sensors. The first method uses wavelength interrogation and requires the measurement of the transmission spectrum of the sensor with the use of a broadband source and an optical spectrum analyzer. The resolution of such sensors is determined by the resolution to which shifts in the resonance wavelengths of the sensors can be measured. Such sensors have been demonstrated in a uniformly thinned fibre Bragg grating (FBG) obtained by using wet chemical etching [45], in a thinned section of fibre (approximate radius of ~1.5 μm) sandwiched between two FBGs used to create a fibre Fabry-Pérot interferometer [46], in the resonance of cladding modes in a thinned FBG [47], in tilted FBGs [48], [49], in FBGs written on side polished fibres [50], on etched D-fibres, [16], [51] and on microstructured fibres [52] and in long-period fibre gratings [53], [54], [55] written on circular fibres. In Table 4-1 we have tabulated the peak sensitivities and operating points of the sensors described above for which have been reported. The range of refractive index values that can be measured for the majority of such sensors reported thus far is typically from 1.33 to 1.46.

Table 4-1: Reported peak sensitivities and operating points for refractive index sensors based on wavelength interrogation taken from the literature.

Peak Sensitivity (nm/RIU)	Operating Point (RIU)	Reference
~600	~1.45	16
340	1.333	48
300	1.455	50
294	1.42	54
~185	~1.35	55
172	~1.45	47
143	~1.45	52
71.2	1.333	46
60	~1.450	45
39	1.43	49

The second method uses intensity measurements and requires the measurement of the power transmission through the sensor using typical optical sources and detectors. In this method, the resolution depends on the resolution to which the optical power transmission can be measured. Such sensors have been demonstrated in a bent plastic multimode optical fibre with a partially stripped cladding [56], in cladded multimode tapered fibre tips with mirrored ends based on the radiation of the modes guided by the cladding [57], in an evanescent wave-based sensor created using a tapered single-mode fibre embedded in a polymer [58], in the leakage of a side-polished single-mode fibre [59], in side-polished plastic optical fibres [60], [61], in a microstructured fibre Bragg grating in a single-mode fibre [62] (the wavelength of the optical source had to be tuned to be close to the Bragg wavelength), in the fibre core diameter mismatches when a small section of a single-mode fibre was sandwiched between two lead multimode fibres [44], in V-shaped unclad multimode fibres with varying angles [63], in a tapered section of multimode fibre sandwiched between two single-mode fibres having two different FBGs [64]. The ranges of operation and the peak resolution reported for the sensors described above are given in Table 4-2. Another specialized group of refractive index sensors includes surface plasmon resonance sensors [65] which use wavelength interrogation [66], intensity measurement [67], or the phase difference between two orthogonal modes [68].

Table 4-2: Reported ranges or operating points and peak resolutions for refractive index sensors based on intensity variations taken from the literature.

Peak Resolution (RIU)	Range/Operating Point (RIU)	Reference
10^{-5}	1.3333-1.4206	64
3×10^{-5}	1.36-1.46	57
7×10^{-5}	1.445-1.455	44
4×10^{-5} and 6×10^{-5}	1.41 and 1.38	62
2.5×10^{-4}	1.35-1.46	63
10^{-4}	1.46-1.48	59
$\sim 5 \times 10^{-4}$	1.37-1.40	58
$\sim 10^{-3}$	1.440-1.446	56
10^{-3}	> 1.417	60
2×10^{-3}	1.45-1.5	61

In this chapter we present a high resolution, wide range, intensity-based refractive index sensor that can be tailored with regard to its operating point and resolution. The sensor head is a short length of D-fibre and the power transmission through the sensor head depends strongly on the surrounding refractive index. In Section 4.2 we describe the operating principle and a study of the effects of the cladding thickness and the operating wavelength on the resolution and operating point of the sensor. In Section 4.3 an experimental analysis of the sensor is presented, demonstrating the ability to fabricate a sensor with a particular operating point and resolution by carefully selecting the etched cladding thickness and the operating wavelength. A discussion is provided in Section 4.4 with concluding remarks given in Section 4.5.

4.2 Operating Principle

As described earlier, the etched D-fibre is leaky when the external refractive index, n_{ext}, is greater than the mode effective index, n_{eff}. In this case the transmission through the sensor head depends on n_{ext} and thus an intensity-based refractive index sensor can be realised. For the purpose of this application, the external refractive index will be denoted as the surrounding refractive index (SRI), n_s. Equation (2-2) has been used to calculate the power transmission ratio, T_P, of the equivalent planar waveguide's TE_0 mode for a 1 cm length of the D-fibre sensor as a function of n_s for several values of d at $\lambda_o = 1550$ nm, as shown in Figure 4-1. The sensor has three regions

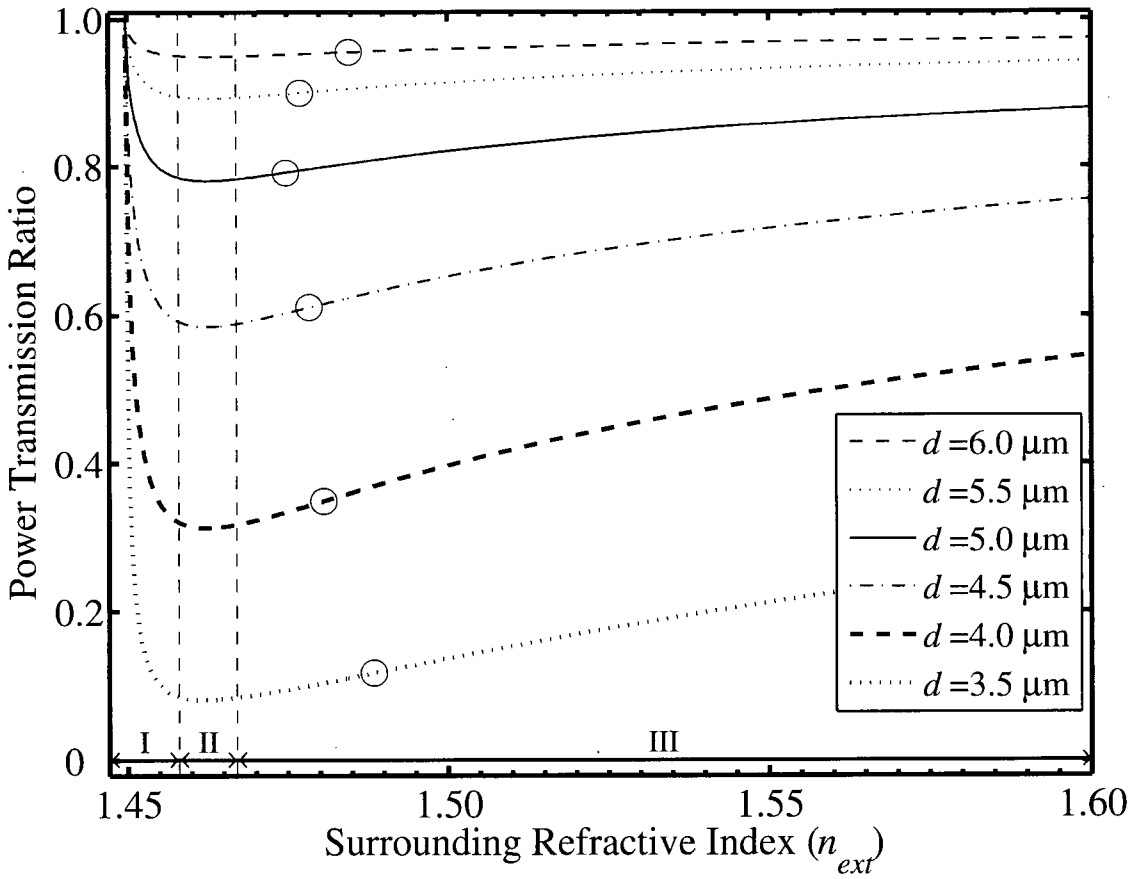

Figure 4-1: Calculated power transmission ratio for the equivalent planar waveguide's TE_0 mode versus n_s for several values of d using $a = 2$ μm, $b = 1$ μm and $L = 1$ cm at $\lambda_o = 1550$ nm. Vertical dotted lines separate Regions I, II, and III. Circles are points where the maximum resolution occurs in Region III.

of operation, separated by the vertical dotted lines (determined subjectively) in Figure 4-1. In Region I, where $n_s \gtrsim n_{eff}$, the power transmission decreases sharply to a minimum and the slope is large and negative over a small refractive index range. In Region II $n_s > n_{eff}$, and the transmission is close to its minimum and its slope is small or even zero. In Region III, where $n_s > n_{eff}$ as well, the transmission increases monotonically and the slope is positive over a large refractive index range. Effects of any non-uniformity in the cladding thickness along the length of the etched region are minimal as they are averaged out over its length. Furthermore, in Region I, the index contrast between the fibre's cladding and the SRI is small.

The resolution to which the refractive index can be measured, Δn_s, depends on the resolution to which T_P can be measured, ΔT_P, and is approximated by

$$\Delta n_s \approx \Delta T_P \left(\frac{\partial T_P}{\partial n_s} \right)^{-1} \tag{4-1}$$

It is apparent from (4-1) that the sensor resolution improves with increasing slope of the transmission ratio. The sensor is most useful in Regions I and III and the maximum resolutions in these two regions, calculated using (4-1), are shown in Figure 4-2 for four values of ΔT_P. In Region I the maximum resolution dramatically improves with decreasing d and occurs at $n_s \approx 1.4495$ for all values of d. In Region III, however, the maximum resolution has a parabolic dependence on d with its best value at the apex of the parabola which occurs at $d \approx 4.0$ μm indicating that there is an optimum cladding thickness, d_{opt}, for such D-fibre sensors that gives the best resolution. The SRI at which the maximum resolution occurs, n_{max}, is different for each d and is marked by the circles in Figure 4-1. The calculated maximum resolution in Region I is on the order of 10^{-6} and such resolutions have, thus far only been reported for fibre Bragg grating based sensors [48], [55] and surface plasmon resonance sensors [66], [68]. Figure 4-3 shows the calculated resolutions in Regions I and III for a sensor with $d = 4.0$ μm as a function of n_s for several values of ΔT_P. The calculated resolution in Region III is on the order of 10^{-2} for $\Delta T_P = 1\%$ over a very large range. The figure shows that as expected, by improving ΔT_P by an order of magnitude, the resolution is also improved by an order of magnitude. In our case, we are able to achieve $\Delta T_P \leq 0.2\%$, with no extra effort, which results in a resolution between 10^{-3} and 10^{-4} over a large range of 0.23 RIUs. For refractive indices other than n_{max} in Region III, the resolution is lower (due to the decreased slope of the transmission ratio) and the optimum cladding thickness is changed, thus, depending on the sensor's operating point its resolution can be maximized by selecting the optimal cladding thickness.

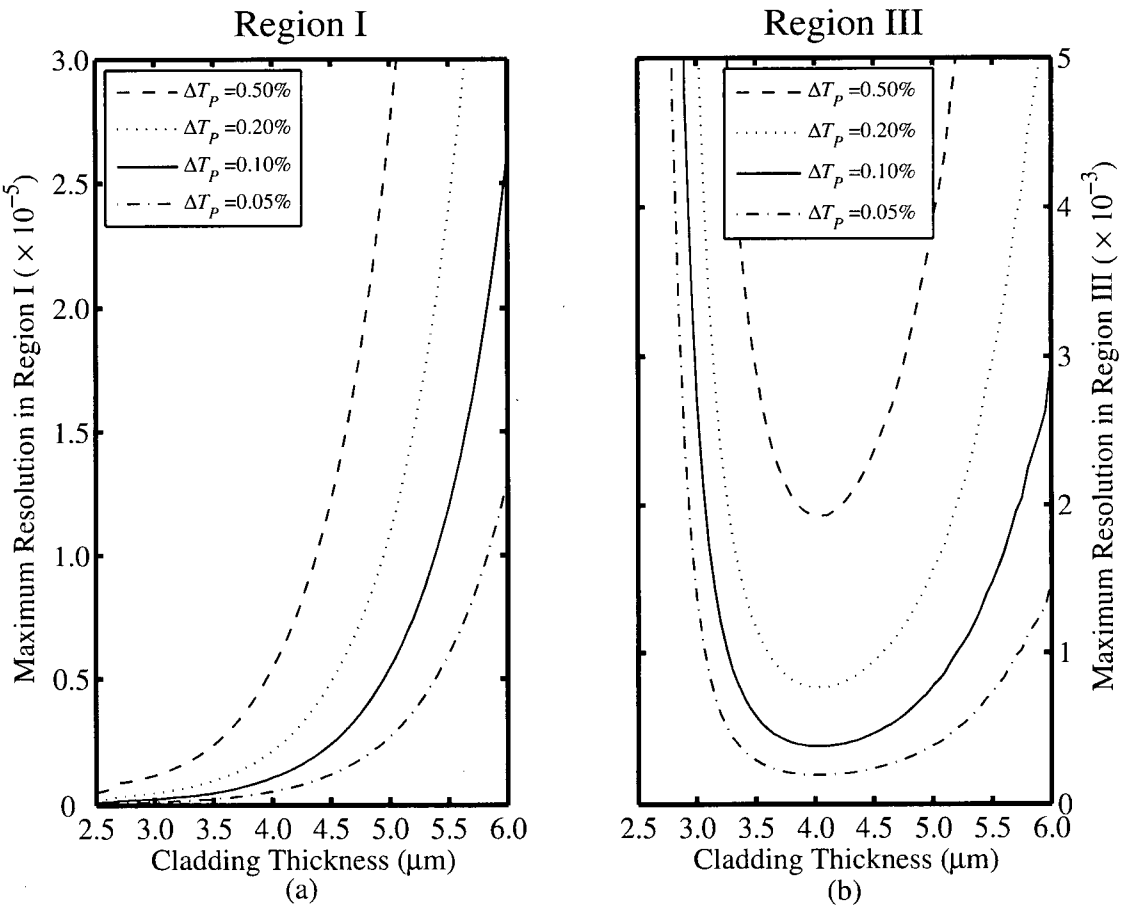

Figure 4-2: Calculated maximum resolution of D-fibre sensor as a function of d for ΔT_P = 0.5%, 0.2%, 0.1% and 0.05% in (a) Region I and (b) Region III.

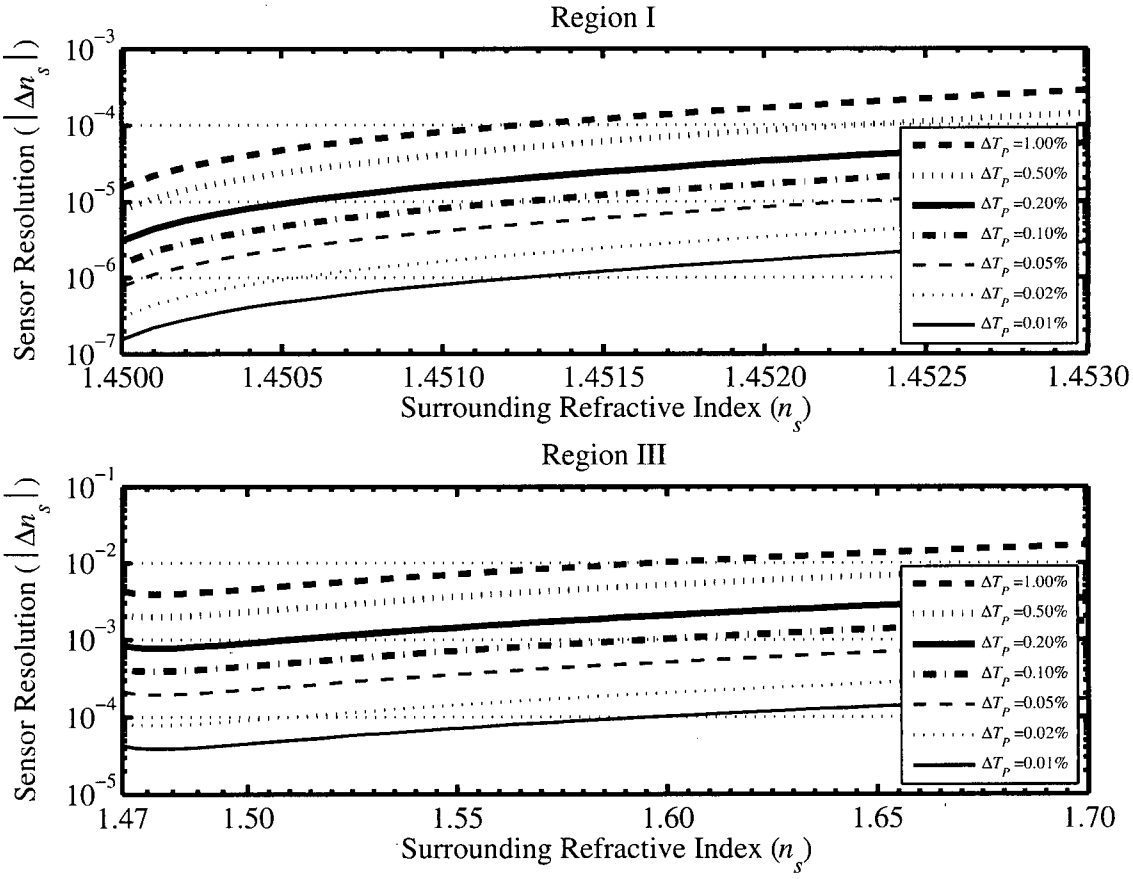

Figure 4-3: Calculated resolution of D-fibre sensor with $d = 4.0$ μm as a function of n_s for several values of ΔT_P in Region I and Region III.

To better exploit the high resolutions obtainable in Region I, it is possible to shift the operating point by changing the operating wavelength λ_o. To demonstrate the effect on the sensor of changing the wavelength, Figure 4-4 shows the calculated power transmission ratio of the equivalent planar waveguide's TE_0 mode in Region I for a 1 cm length of our D-fibre sensor as a function of n_s at several wavelengths using $d = 4.0$ μm. For each wavelength, the refractive index distribution of the fibre was determined using the equations for germania-doped and fluorine-doped silica given in [69]. The range over which Region I can be shifted is ~0.012 RIUs, which is sufficiently large for applications that require the accurate measurement of the refractive indices of the many liquids, such as typical hydrocarbons, for which $1.45 \leq n_s \leq 1.46$.

The maximum resolution point in Region III, i.e., n_{max}, can also be shifted by changing the operating wavelength. Here, d_{opt}, is a function of both the operating point and the operating wavelength. Figure 4-5 shows the optimum cladding thickness as a function of n_s for several wavelengths. The d_{opt} for each wavelength is significantly different and shown in Figure 4-6 are the power transmission curves at several wavelengths using the optimum cladding thickness for each wavelength. The figure's legend shows d_{opt} and the corresponding n_{max} for each wavelength. Here, n_{max} can be shifted by ~0.027 RIUs, which is a significant amount considering the number of liquids that have refractive indices between 1.46 and 1.50, such as glycerin, benzene, chloroform, honey, turpentine, and sugar solutions. Figure 4-2 to Figure 4-6 illustrate that, in principle, a sensor having a desired resolution and operating point can be realized by carefully selecting the correct combination of the cladding thickness and the operating wavelength.

Furthermore, a tuneable broadband sensor can also be realized by picking a particular cladding thickness. Figure 4-7 shows power transmission ratio curves in Region I for $d = 2.50$ μm at several wavelengths illustrating that the operating wavelength can be tuned to change the sensor's operating point over the range $1.4462 \leq n_s \leq 1.4583$. For $\Delta T_P = 0.2\%$, the maximum resolution is $\sim 8 \times 10^{-8}$ RIUs at $\lambda_o = 1200$ nm and improves to $\sim 1 \times 10^{-8}$ RIUs at $\lambda_o = 1700$ nm. The points of maximum resolution for each wavelength are marked by the solid circles. A broadband device can also be realized for Region III by making a trade off between the sensor resolution and the ability to tune the device using the operating wavelength. Figure 4-8 shows the sensor's resolution at four different operating points in Region III for $\Delta T_P = 0.2\%$ at several wavelengths as a function of the cladding thickness. Figure 4-8 also illustrates how d_{opt} (the apexes of the parabolas) changes with wavelength and operating point. Furthermore, Figure 4-8 gives a sense of how sensitive the resolution is to the cladding thickness, d.

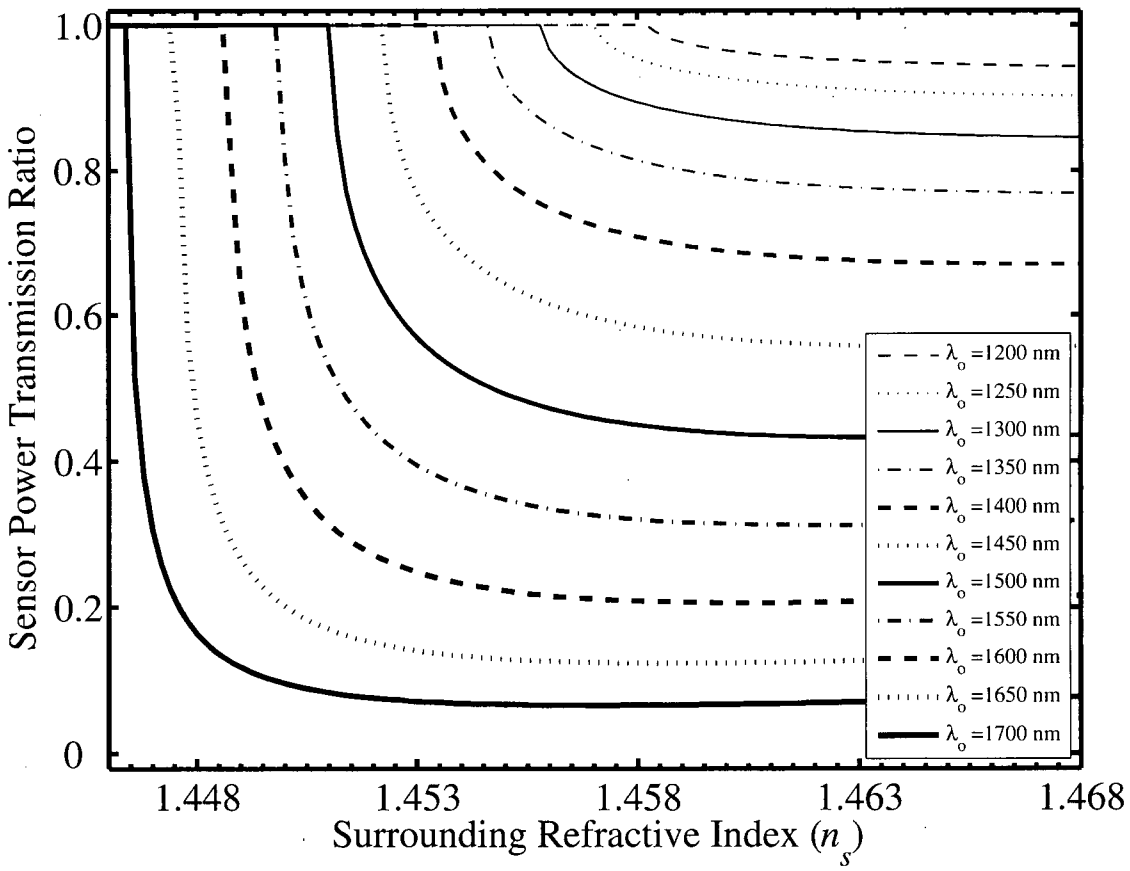

Figure 4-4: Calculated power transmission ratio for the TE_0 mode of the equivalent planar waveguide in Region I versus n_s at several wavelengths using $a = 2$ μm, $b = 1$ μm, $L = 1$ cm and $d = 4.0$ μm.

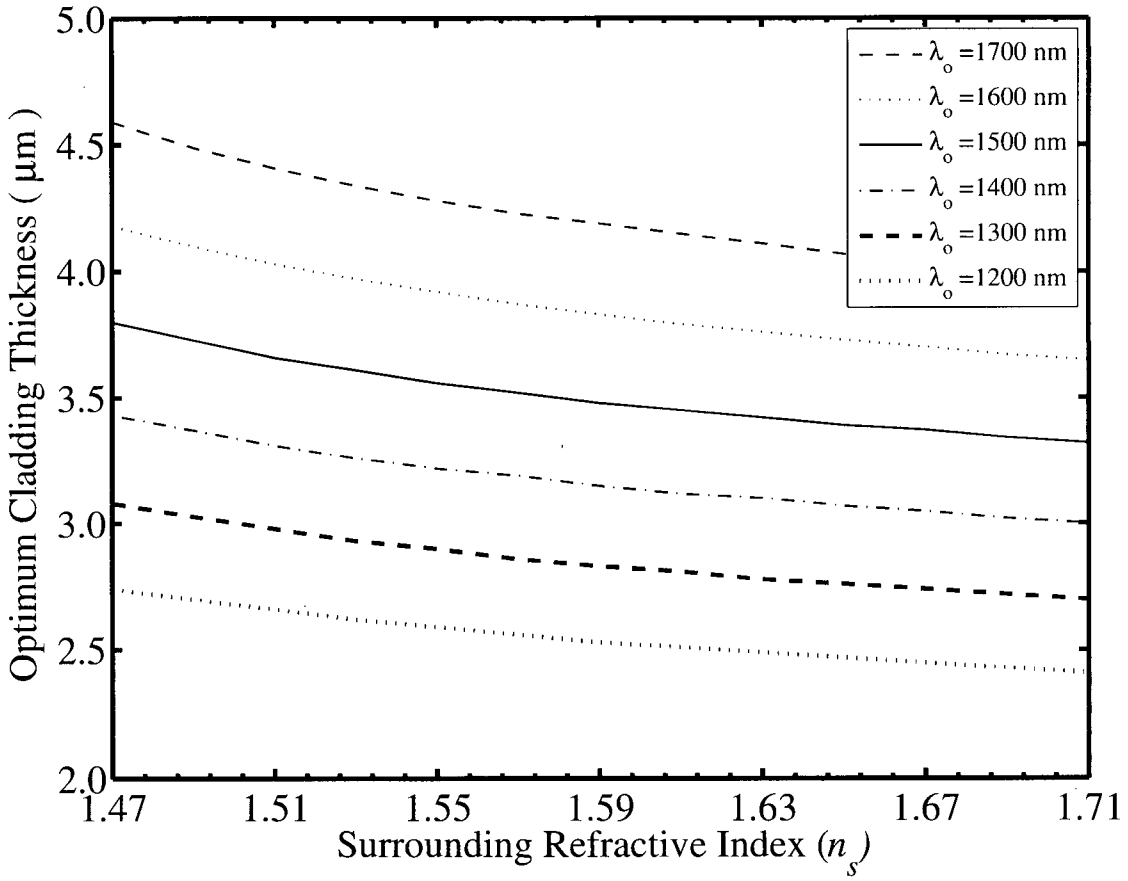

Figure 4-5: Optimum cladding thickness as a function of n_s for several wavelengths.

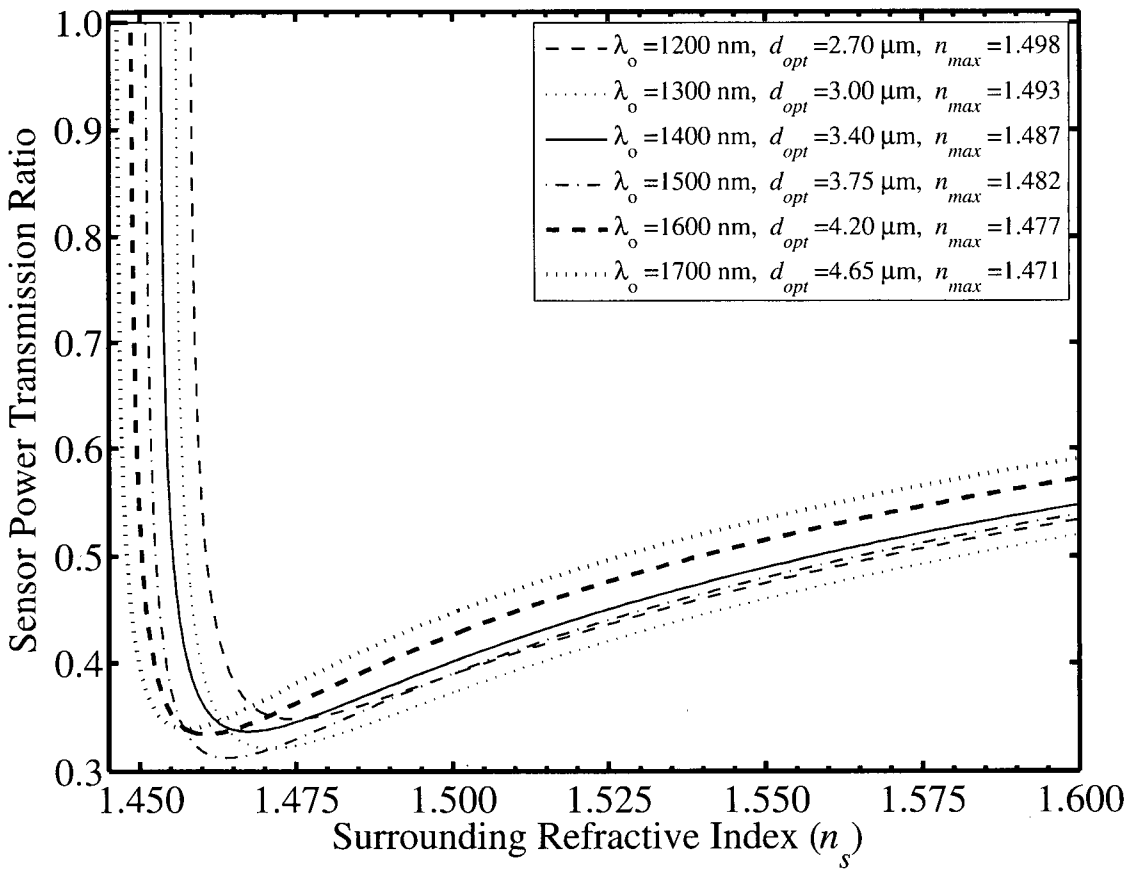

Figure 4-6: Calculated power transmission ratio for the equivalent planar waveguide's TE_0 mode versus n_s for several values of λ_o using L = 1 cm and d_{opt} for each wavelength. The legend shows the point at which the maximum resolution occurs.

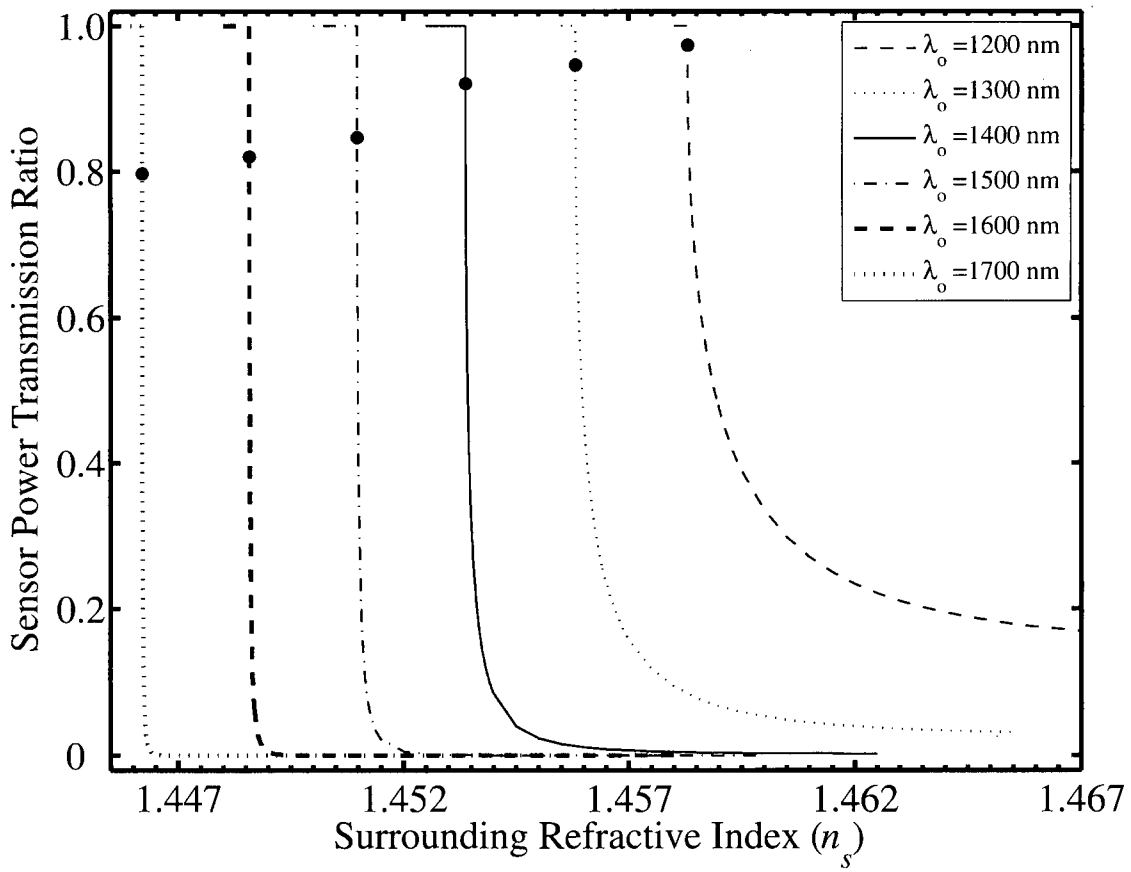

Figure 4-7: Power transmission ratio curves for the equivalent planar waveguide's TE_0 mode in Region I as a function of n_s for $d = 2.50$ μm at several wavelengths. Dark circles mark the points of maximum resolution.

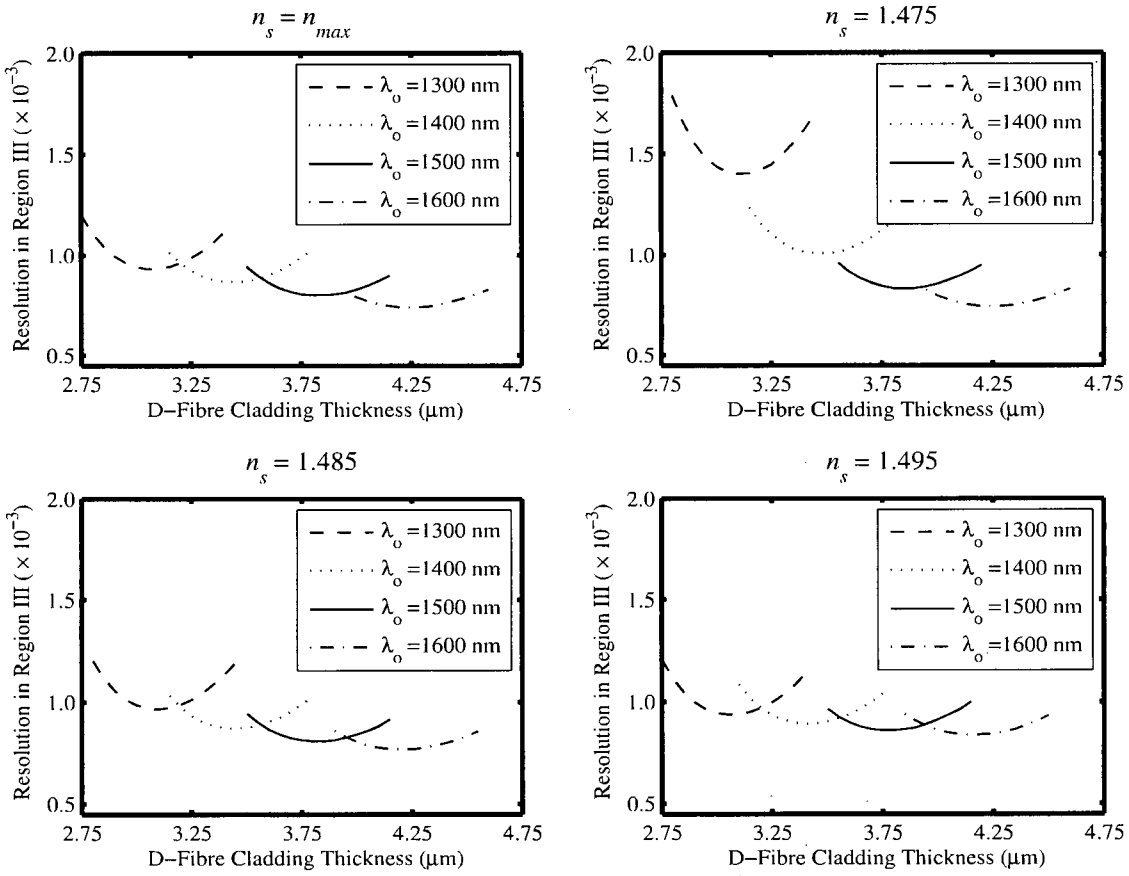

Figure 4-8: Sensor resolution in Region III at four different operating points as a function of cladding thickness at several wavelengths using $\Delta T_P = 0.2\%$.

4.3 Experimental Setup and Results

The sensor was fabricated in a similar fashion to that described in Section 3.2 and is briefly repeated here for convenience. A one-centimetre long stripped section of D-fibre was dipped in acetone for 20 minutes to clean the fibre and then etched in a 10% hydrofluoric acid solution for 150 to 180 minutes to obtain the desired cladding thickness. To determine the cladding thickness after etching, we used the technique described in Section 3.4.

We used standard thermo-optic oils to measure the sensor's response so that changes in the oils' temperatures would result in changes in their refractive indices. OIL-1 had an index of refraction at 25°C, n_0, and thermo-optic coefficient, dn/dT, of 1.4710 ± 0.0005 and -3.86×10^{-4}/°C, respectively, at $\lambda_o = 1550$ nm and OIL-2 had $n_0 = 1.451 \pm 0.0005$ and $dn/dT = -3.83\times10^{-4}$/°C at $\lambda_o = 1550$ nm. The values given by the manufacturer for the thermo-optic coefficients of the oils were valid for a temperature range of 15-35°C. Outside of this range, the values were not exactly known. Thus to characterize the sensor in Region I, OIL-2 was used and in Region III, OIL-1 was used, keeping their temperatures between 15-35°C.

The experimental setup is shown in Figure 4-9. The D-fibre was threaded through a specially built aluminum plate that had a trench in it to contain the thermo-optic oil. The plate also served as the cold plate for the thermoelectric cooler (TEC) used to control the temperature of the oil. The polarization controller (PC) was used to launch only the $_oHE_{11}$ mode in the fibre. To confirm that the $_oHE_{11}$ mode was launched correctly, an analyzer was placed at the output to measure the extinction ratio between the two orthogonal modes of the fibre, which we found to be consistently in excess of 27 dB. The ends of the D-fibres were coupled to standard SMF-28 fibres using mechanical splices.

4.3.1 Sensor Resolution

To demonstrate the sensor's high resolution, its response was measured at a single wavelength ($\lambda_o = 1550$ nm) using a monochromatic source and a power meter. A sensor with a cladding thickness of ~4.0 μm was fabricated and will be referred to as Sensor-1 from now on. The power level when the sensor was surrounded by air was used as the reference level to calculate the transmission ratio values. With the sensor immersed in the oil, the temperature was ramped up in discrete steps and for each step the temperature was allowed to stabilize before it was sampled along with the sensor's transmission ratio. The temperature was increased until the power transmission ratio was unity and further increases in temperature yielded no changes in the

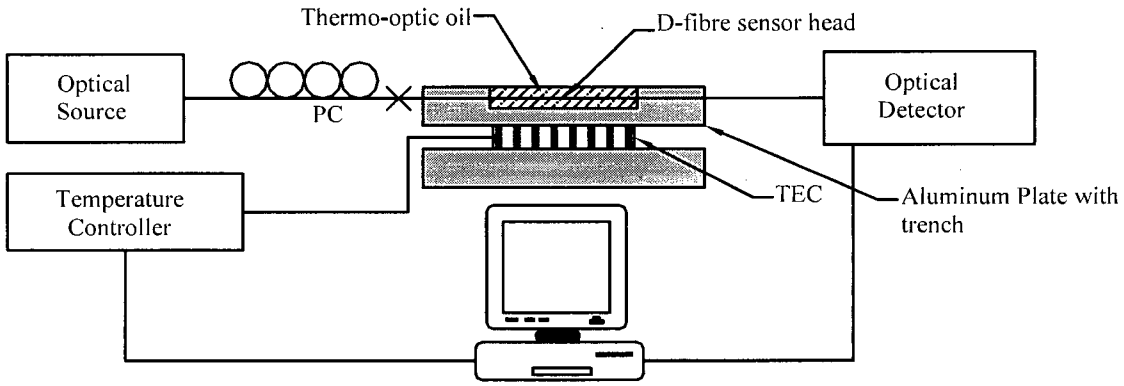

Figure 4-9: Experimental setup showing sensor head immersed in thermo-optic oil. TEC-Thermoelectric Cooler; x-Fibre splice; PC-Polarization Controller.

transmission, indicating that the sensor was in its lossless region, i.e., $n_s < n_{eff}$. Several such ramps were conducted yielding virtually identical results. The measured temperature was used to determine the refractive index of the oil. Figure 4-10 shows the measured power transmission ratio of Sensor-1 at $\lambda_o = 1550$ nm as a function of the refractive index of OIL-1. The slope in Region III of the measured response was used to determine the sensor's resolution. For $\Delta T_P = 0.2\%$, the measured maximum resolution over the range of Region III for which the transmission was measured was $\sim 5 \times 10^{-4}$ at $n_s \approx 1.475$ and agrees reasonably well with the calculated resolution of 7×10^{-4} shown in Figure 4-2. The slight discrepancy can be attributed to the fact that the calculated value was determined using the slope of the calculated transmission ratio, which is lower than what is measured, as mentioned in Section 3.4.1. In order to be in Region I, the temperature of OIL-1 had to be between 65 and 80°C, which was close to the limit of our thermoelectric cooler and, as mentioned earlier, the thermo-optic coefficient of the oil was not exactly known at such high temperatures. Thus, for better temperature control and accurate knowledge of the refractive index of the oil, OIL-2 was used to measure the power transmission ratio of the sensor in Region I, and is shown in Figure 4-11. The measured maximum resolution with OIL-2 was determined to be 2×10^{-6} at $n_s \approx 1.449$ and agrees well with the calculated resolution of 2×10^{-6} shown in Figure 4-2.

4.3.2 Operating Point

To demonstrate the ability to shift the operating points in either of the two regions, the power transmission ratio was measured at several wavelengths using several monochromatic sources and the same method described in the previous section. Measurements were only made at the wavelengths that were readily available. At each wavelength, the Cauchy equations and thermo-optic coefficients for each oil were used to determine their respective refractive indices. Figure 4-12 shows the measured power transmission ratio of Sensor-1 at several wavelengths using OIL-1. To demonstrate the tuneable broadband sensor proposed in Figure 4-7, a second sensor, Sensor-2, with a smaller cladding thickness than Sensor-1 was fabricated. Figure 4-13 shows the measured power transmission ratio of Sensor-2 using OIL-2. The measured shift of the operating point in Region I shown in Figure 4-13 was ~0.006 RIUs, which agrees reasonably well with the calculated shift of 0.007 RIUs shown in Figure 4-4, validating the model and the predictions made. The measured maximum resolution for Sensor-2 was $\sim 4.8 \times 10^{-6}$ at $n_s \approx 1.4535$ for $\lambda_o = 1310$ nm and $\sim 9.8 \times 10^{-7}$ at $n_s \approx 1.4481$ for $\lambda_o = 1610$ nm.

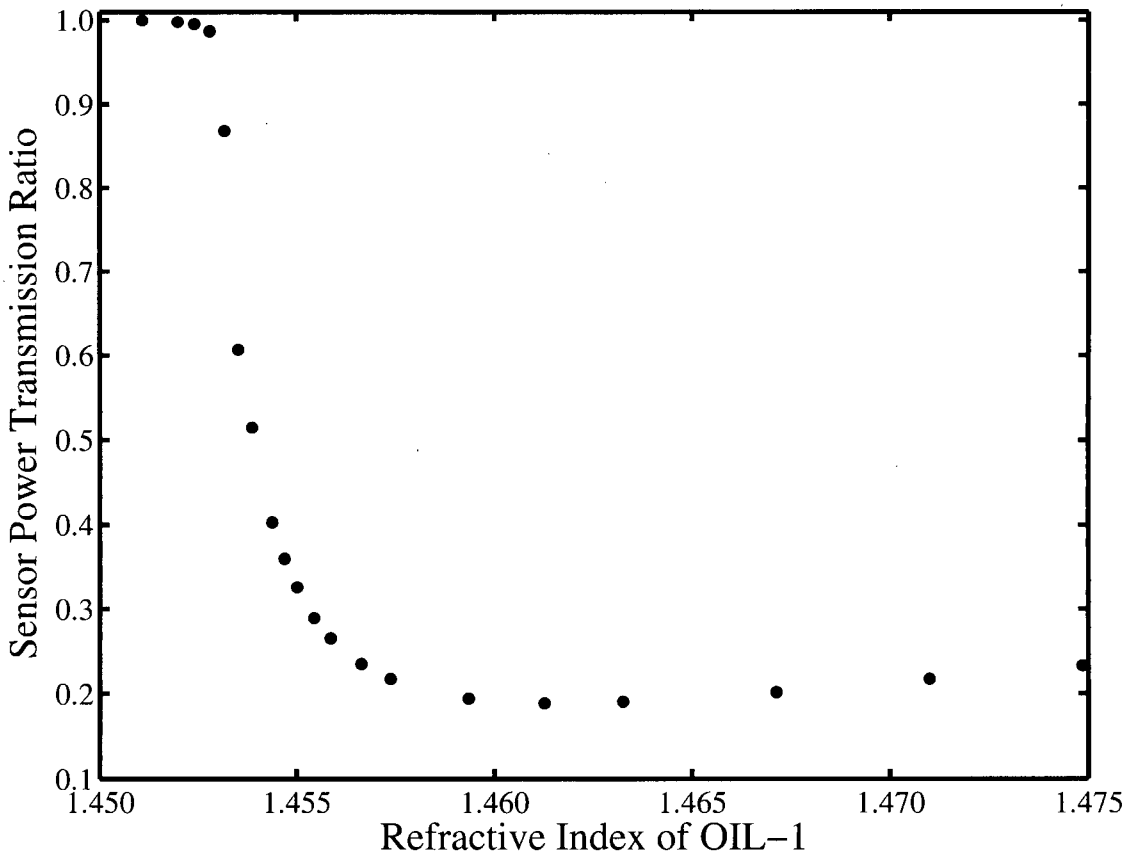

Figure 4-10: Measured power transmission ratio of Sensor-1 in all Regions using OIL-1 at $\lambda_o = 1550$ nm.

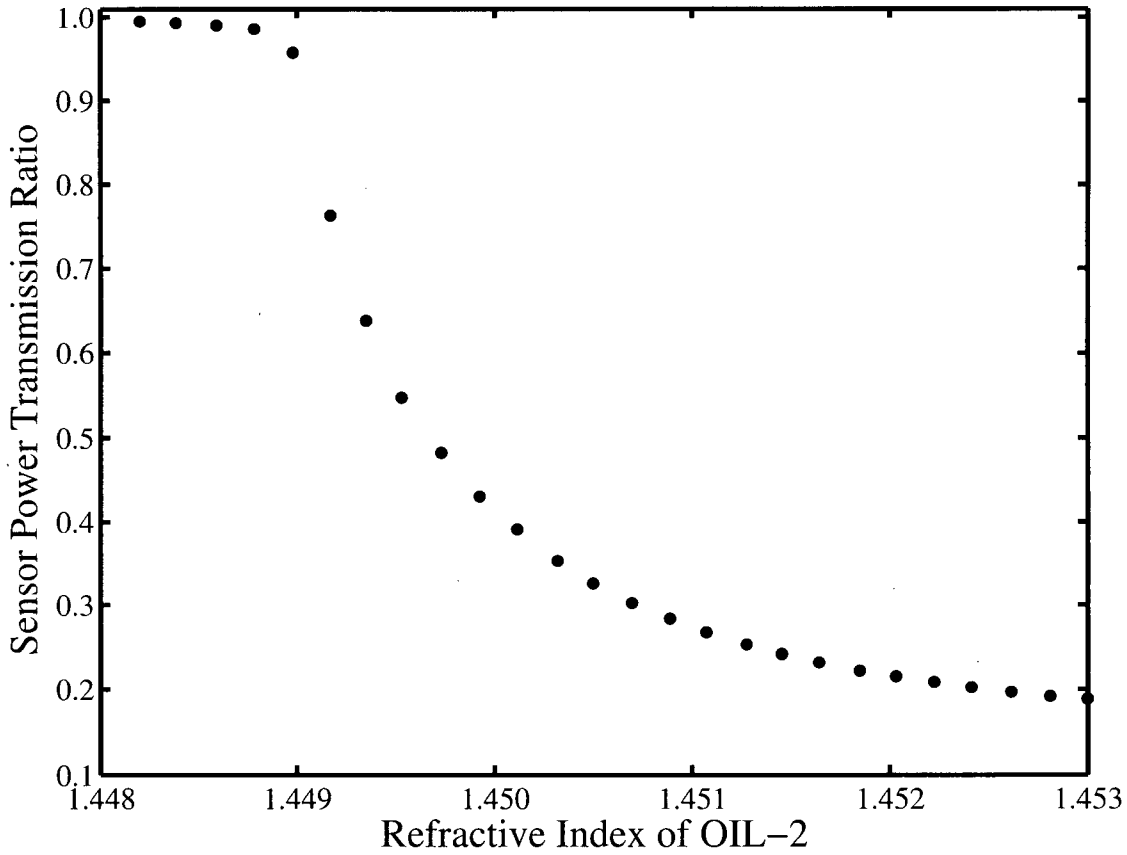

Figure 4-11: Measured power transmission ratio of Sensor-1 in Region I using OIL-2 at $\lambda_o = 1550$ nm.

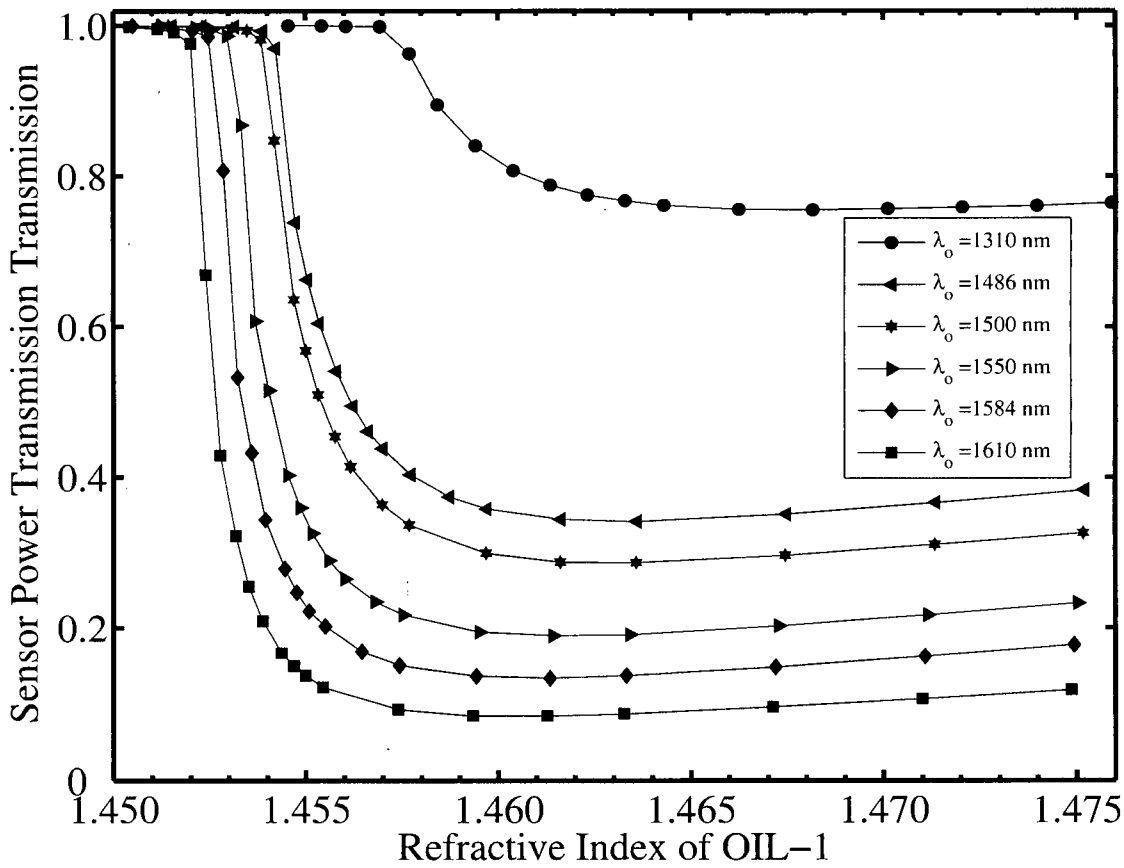

Figure 4-12: Measured power transmission ratio of Sensor-1 using OIL-1 at several wavelengths.

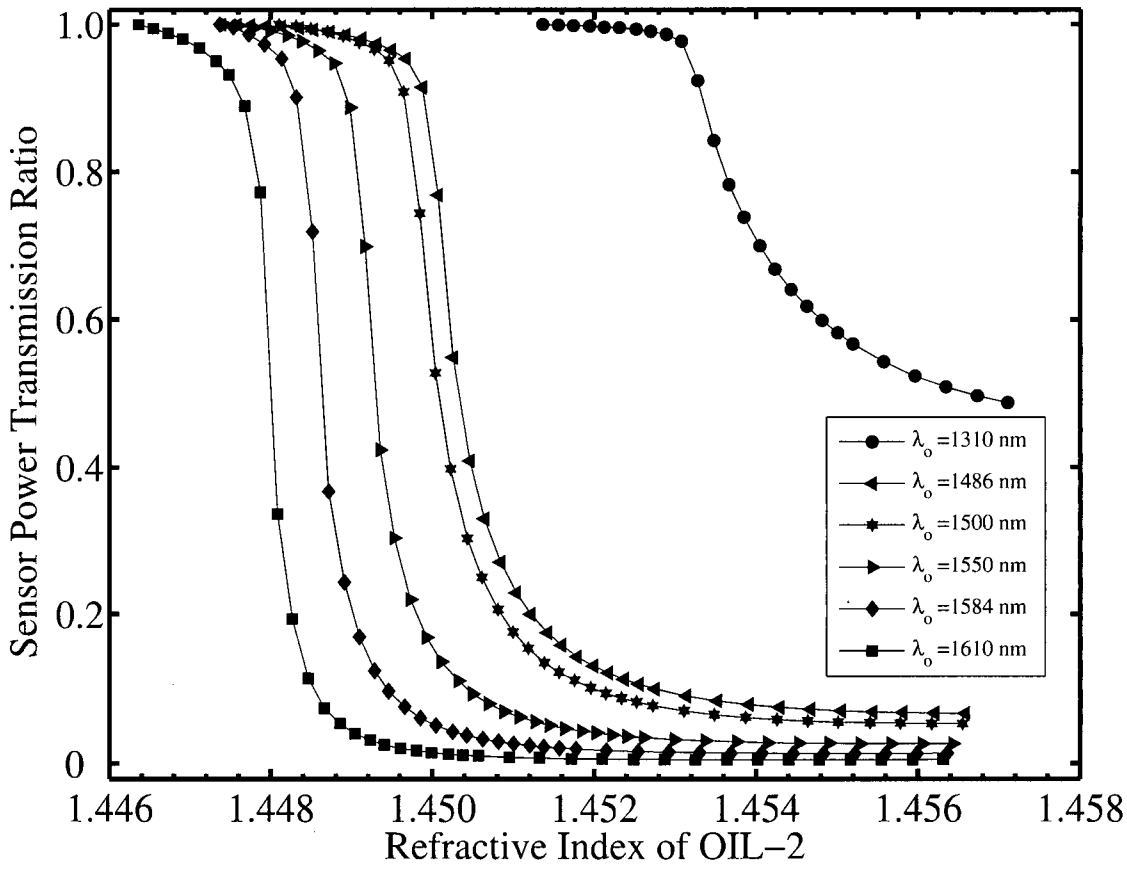

Figure 4-13: Measured power transmission ratio of Sensor-2 in Region I using OIL-2 at several wavelengths.

4.4 Discussion

As noted earlier, the sensor has two useful regions of operation and thus it is possible to get the same power transmission value for two different refractive indices. However, it is expected that the sensor would be optimized to operate in only one of these regions.

As we used a thermo-optic oil as the surrounding refractive index, the effects of temperature on the sensor could not be overlooked. The thermo-optic coefficient of silica, which is -10^{-5} RIU/°C, was used to calculate the effect of temperature on the sensor's response. This was done by calculating the refractive indices of the core and cladding at each temperature point and using those values in the model. Figure 4-14 shows the power transmission ratio at five different ambient temperatures for a sensor with $L = 1$ cm and $d = 4.0$ μm at $\lambda_o = 1550$ nm. The thermo-optic effect in the silica is most pronounced in Region I and has less of an effect in Region III. The shift of Region I due to ambient temperature changes is $\sim 10^{-5}$/°C, indicating that for an accurate measurement of the refractive index, when operated in Region I, the sensor and the surrounding refractive index must be kept at a constant temperature. As a majority of fibre optic sensors are sensitive to temperature changes and require some sort of temperature compensation/control, this is a common requirement.

The measured power transmission ratio curves of the D-fibres shown in the preceding figures illustrate that there is a gradual decrease in T_P as n_{ext} approaches n_{eff}, as opposed to a sharp decrease predicted by the theoretical model as is shown in the calculated transmission ratio curves. This effect is due to the fact that the thermo-optic oils used are lossy (their transparency decreases with increasing wavelength). Part of the evanescent optical field of the D-fibre propagates in the oil and thus optical power is lost due to absorption in the oil even before the mode becomes leaky, i.e., when $n_{ext} < n_{eff}$. As n_{ext} approaches n_{eff}, the evanescent field penetrates deeper into the oil (the transverse propagation constant decreases) and more of the optical field propagates in the oil, leading to increased absorption loss in the oil. This effect is demonstrated well in Figure 4-13 where this gradual decrease gets more pronounced as the wavelength increases.

Since the sensor presented is intensity-based, its response depends on the measurement of the optical transmission, which can fluctuate due to factors such as source temperature changes, detector responsivity changes, link attenuation changes, and those caused by changes in mechanical components such as connectors, mechanical support mounts, and optics [70].

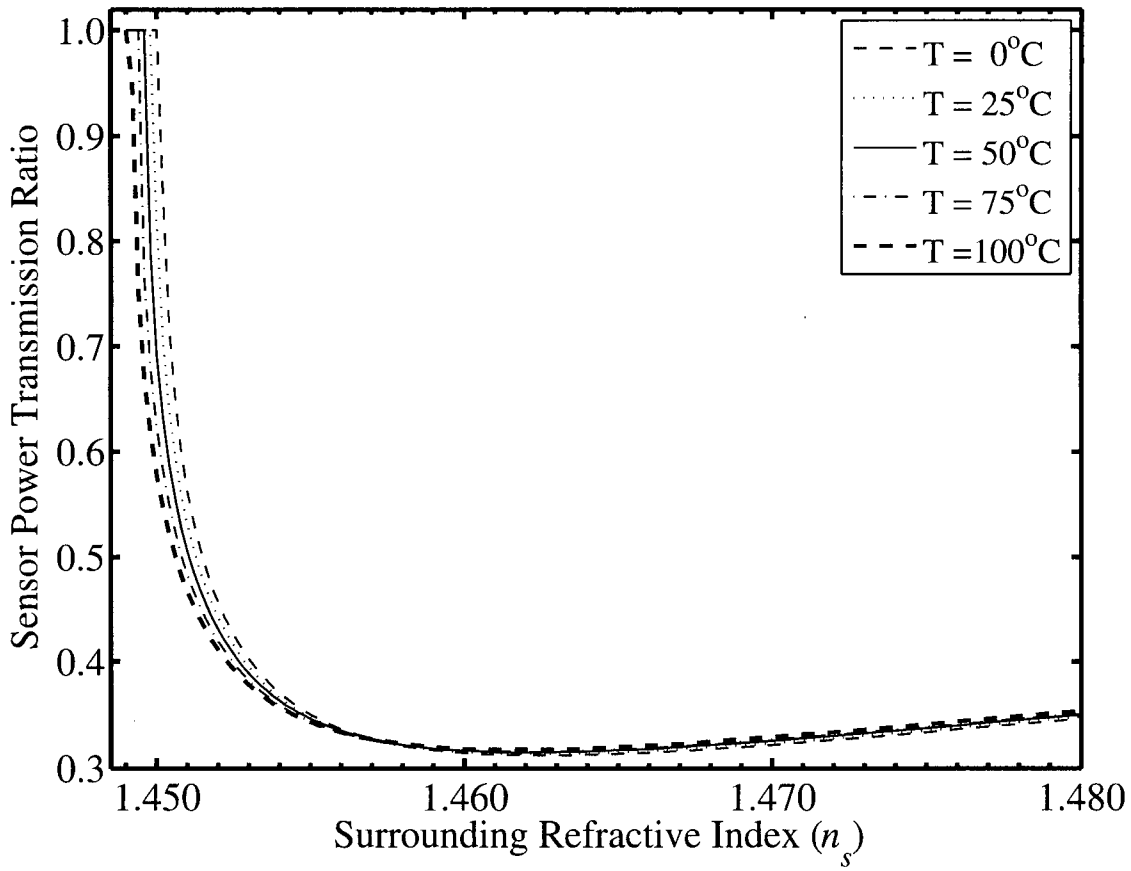

Figure 4-14: Calculated power transmission ratio versus surrounding refractive index at various ambient temperatures for a sensor with $L = 1$ cm and $d = 4.0$ μm at $\lambda_o = 1550$ nm.

Nevertheless, in an industrial application, compensation techniques commonly used with intensity-based optical fibre sensors can be applied [71].

4.5 Conclusions

In this chapter, a high resolution refractive index sensor that can be tailored with regard to its operating point and resolution was presented. The power transmission ratio of the sensor depends on the surrounding refractive index when it is greater than the mode effective index. Our sensor had a measured maximum resolution of 2×10^{-6} for $\lambda_o = 1550$ nm at indices close to the effective mode index. We have shown that the best calculated resolution can be 1×10^{-8} at $\lambda_o = 1700$ nm. The resolution and the point at which the maximum resolution occurs can be shifted by selecting the correct combination of the cladding thickness and operating wavelength. The maximum resolution point can be shifted by as much as ~0.012 RIUs in the high resolution region and by ~0.027 RIUs in the low resolution region with a corresponding wavelength change of 500 nm. The advantages of the sensor are its high resolution, its adjustable operating point, its wide operating range, its manufacturing simplicity, and its implementation using readily available optical sources and simple detection schemes.

Chapter 5

5 Temperature Sensor

5.1 Introduction

The use of thermo-optic oils to demonstrate the refractive index sensors presented in the previous chapter naturally led to the idea of creating high resolution temperature sensors. It became apparent that the oils could be used as the external medium to induce changes in the power transmission of the D-fibres. In this chapter we investigate the use of the etched D-fibres and thermo-optic oils as temperature sensors.

Wavelength-based fibre optic temperature sensors have been studied and demonstrated. They are commonly based on the shift of the reflected Bragg wavelength of gratings written in fibres with a change in temperature [14], [72], [73], [74], [75]. Resonance wavelength shifts with temperature have also been demonstrated in single-mode side-polished fibres covered with polymer planar waveguides [8], [76]. These sensors require measurement of their reflected Bragg wavelengths or their optical spectrums, in contrast to the sensors reported in this work, which are intensity-based. Such intensity-based sensors have been previously reported. The sensitivity of side-polished fibres to the refractive indices of external media has been demonstrated in [77] over a range of 10 to 70°C with a sensitivity of 0.5 dB/°C. A higher sensitivity of 5 dB/°C over a smaller range of 5°C was also demonstrated. The refractive index of the external medium had to be greater than the mode effective index of the fibre. Alternatively, a lossy medium with a refractive index less than the mode effective index of a single-mode fibre was used as the external medium in a side-polished fibre [78]. A range of 50°C and a sensitivity of 0.2 dB/°C were reported. A multimode fibre with its cladding replaced by a liquid over a short section (unclad zone) was used to change the number of guided rays in the section, resulting in a power loss through the fibre [79]. A range of around 50–80°C with a sensitivity of ~0.02 dB/°C was reported. The cross coupling between two multimode cores as a function of the temperature of the cladding material between the cores was exploited to create a temperature sensor with a range of 120°C and a sensitivity of 0.02 dB/°C [80]. It should be mentioned as a relevant side

---

A version of this chapter has been published. Chandani, S.M. and Jaeger, N.A.F. (2006) Fiber-optic temperature sensor using evanescent fields in D fibers, IEEE Photonics Technology Letters 17:2706-8.

note, that Smith *et al.* have replaced part of the core of a D-fibre with a polymer and have shown that its temperature sensitivity is enhanced by at least a factor of five [81].

In this section we describe temperature sensors realised using etched D-fibres [82]. In section 5.2 we briefly describe the operating principle of the sensor. The experimental setup and results are presented in Section 5.3 and concluding remarks given in Section 5.4.

5.2 Operating Principle

The principle of operation of the temperature sensor is based on that of the refractive index sensor presented in Section 4.2. By using thermo-optic oils as the external media, intensity-based fibre optic temperature sensors can be created. Thermo-optic oils are liquids that have a temperature dependent refractive index. Typically the change in refractive index is linear with a corresponding change in temperature. Thus, the refractive index of the oil, n_{oil}, at a particular temperature, T, can be written as

$$n_{oil} = n_0 + \frac{dn}{dT}(T - T_0) \tag{5-1}$$

where n_0 is the refractive index known at a particular temperature T_0, and dn/dT is the thermo-optic coefficient of the oil. The thermo-optic coefficient is negative and thus an increase in the temperature results in a decrease in the refractive index.

By carefully selecting a thermo-optic oil to have a refractive index greater than the mode effective index of the sensor head, a temperature sensor with a tailored sensitivity and temperature range can be realised. Referring to Figure 4-1, the sensor can have two useful regions of operation: Region I and Region III. The change in power transmission in Region II is smaller, and at some point is zero, than that in Regions I and III and thus is not a good choice for use as a sensor.

5.3 Experimental Setup and Results

The experimental setup is identical to that shown in Figure 4-9. One-centimetre long sections of the D-fibres were etched in a 10% hydrofluoric acid solution for ~180 minutes, resulting in values of d between 4 and 6 μm. The etched sections were immersed in thermo-optic oils obtained from Cargille Labs. The oils were contained in a specially built aluminum plate with a trench in it, through which the etched sections of the fibres were threaded. The plate also served as the cold plate for the thermoelectric cooler (TEC) that controlled the temperature of the oil. A

polarization controller was inserted between the optical source and the D-fibre so as to scan through all possible polarization states, which would then couple to the two modes of the D-fibre. In this way, we were able to launch each of the two orthogonal modes separately.

Figure 5-1 shows the measured power transmission ratio of a temperature sensor (Sensor-A) fabricated by etching a fibre for 180 minutes. Since a polarization controller was used to scan through all possible polarization states of the input light, the measured response at any particular temperature had a minimum and maximum value. These extreme values correspond to the sensor's response for each of the fibre's modes, i.e., in the absence of the other mode. Figure 5-1 shows the response for both modes, as well as the difference between the transmissions of the two modes, indicating a relatively constant offset. The thermo-optic oil used, OIL-1, had an index of refraction at 25°C, n_0, and thermo-optic coefficient, dn/dT, of 1.4710 ± 0.0005 and $-3.86\times10^{-4}/^{\circ}C$, respectively, at 1550 nm. Using these values, the refractive index of the oil can be determined as a function of temperature.

The data in Figure 5-1 show that in Region I, the power transmission ratio has a large slope over a small temperature range, whereas in Region III the power transmission ratio has a smaller slope over a larger temperature range. The sensor would likely be operated in either of these two distinct regions, but not both. The sensor's responses in portions of these two regions are shown in Figure 5-2 and Figure 5-3 along with linear fits to the data. The slopes (sensitivities) of the fitted line and the regression coefficients of the fits are given in the figures' legends. Given that the power transmission can be measured with a resolution of 0.2%, the resolution of the demonstrated sensor in Region I is 0.03°C between 80-85°C and the resolution in Region III is 1.5°C below 60°C (calculated using an equation similar to (4-1)). The resolution is very high in Region I but only over a narrow temperature range whereas the resolution is lower in Region III over a wider range.

The TEC used could not be reliably set to temperatures below 10°C, however, as predicted by the theoretical model, the sensor response remains monotonic for lower temperatures and, in principle, can be used as a sensor for temperatures below 10°C, depending on the thermo-optic oil. It is possible to shift the operating point and modify the range of the sensor. The high resolution of Region I can be shifted to other temperature ranges by using different thermo-optic oils. Similarly, Region III can also be shifted. The ranges of both these regions can be extended by using thermo-optic oils with lower thermo-optic coefficients. For example, Figure 5-4 shows the measured power transmission ratio of a second etched D-fibre (Sensor-B) with different

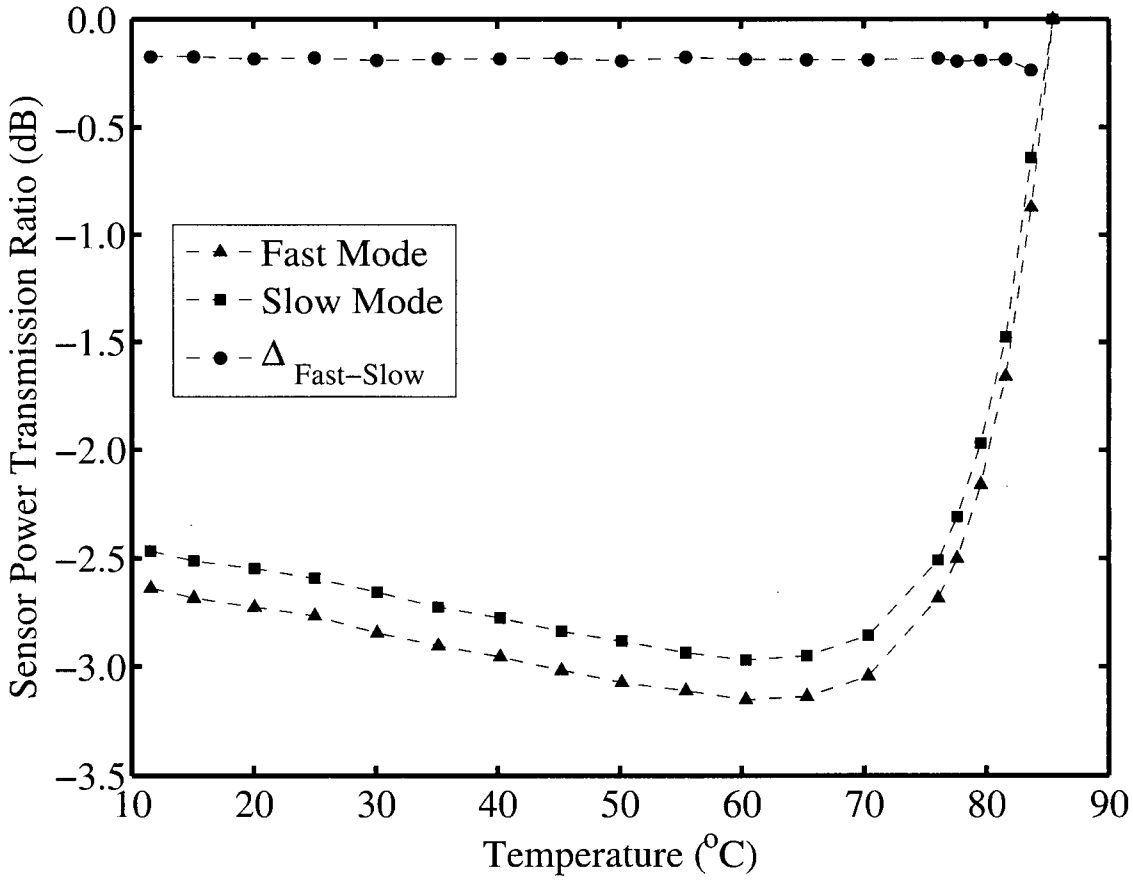

Figure 5-1: Measured power transmission ratio (in dB) of Sensor-A for both modes as a function of temperature of OIL-1. Shown is the relative difference in transmission for the two modes.

thermo-optic oil, OIL-2, having index of refraction at 25°C, n_0, and thermo-optic coefficient, dn/dT, of 1.4510 ± 0.0005 and -3.83×10^{-4}/°C, respectively, at 1550 nm. In this case, Region I has been shifted to be around 29°C. The data points in Region I have been fit to a line with the slope of the line and the regression coefficient of the fit shown in the figure's legend. In this case, the resolution of the sensor is ~0.005°C over a narrow range of 28-30°C.

An additional example shows the power transmission ratio in Region III of a third sensor (Sensor-C) with a third thermo-optic oil, OIL-3, having index of refraction at 25°C, n_0, and thermo-optic coefficient, dn/dT, of 1.493 ± 0.0005 and -3.91×10^{-4}/°C, respectively, at 1550 nm. In this case, the wide range of Region III has been extended to close to 100°C with a resolution of 1.3°C over the entire range. The response has been fit to a line with the slope of the line and the regression coefficient of the fit shown in the figure's legend.

5.4 Conclusions

In this chapter, a temperature sensor using etched D-fibres and thermo-optic oils was demonstrated. The sensor has two regions of operation; a high resolution region with a narrow range and a lower resolution range with a wide range. The operating point and dynamic range of the sensor can be shifted or extended by selecting appropriate thermo-optic oils and by controlling the cladding thickness. As with the refractive index sensor, designs that exhibit higher sensitivities and operate over various, selected temperature ranges can easily be achieved.

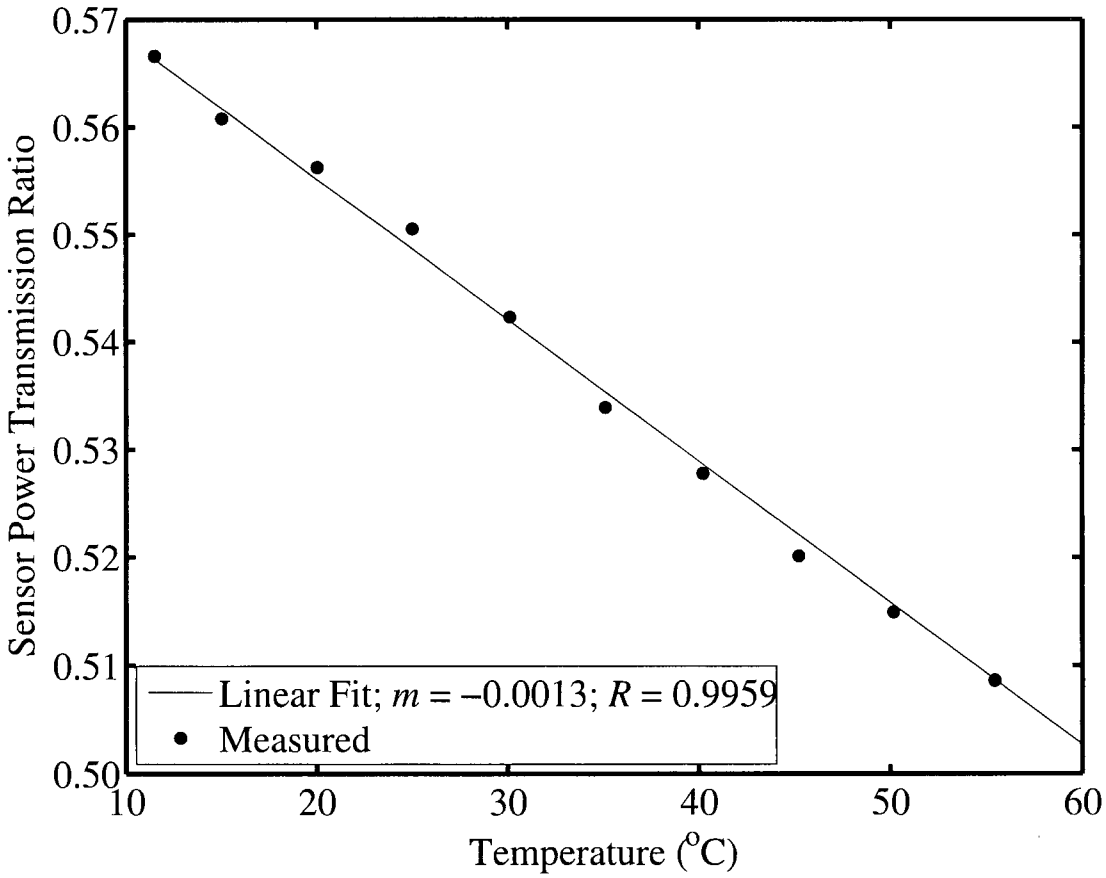

Figure 5-2: Measured power transmission ratio of Sensor-A in Region III along with linear fit with slope and regression of the linear fit given in the legend.

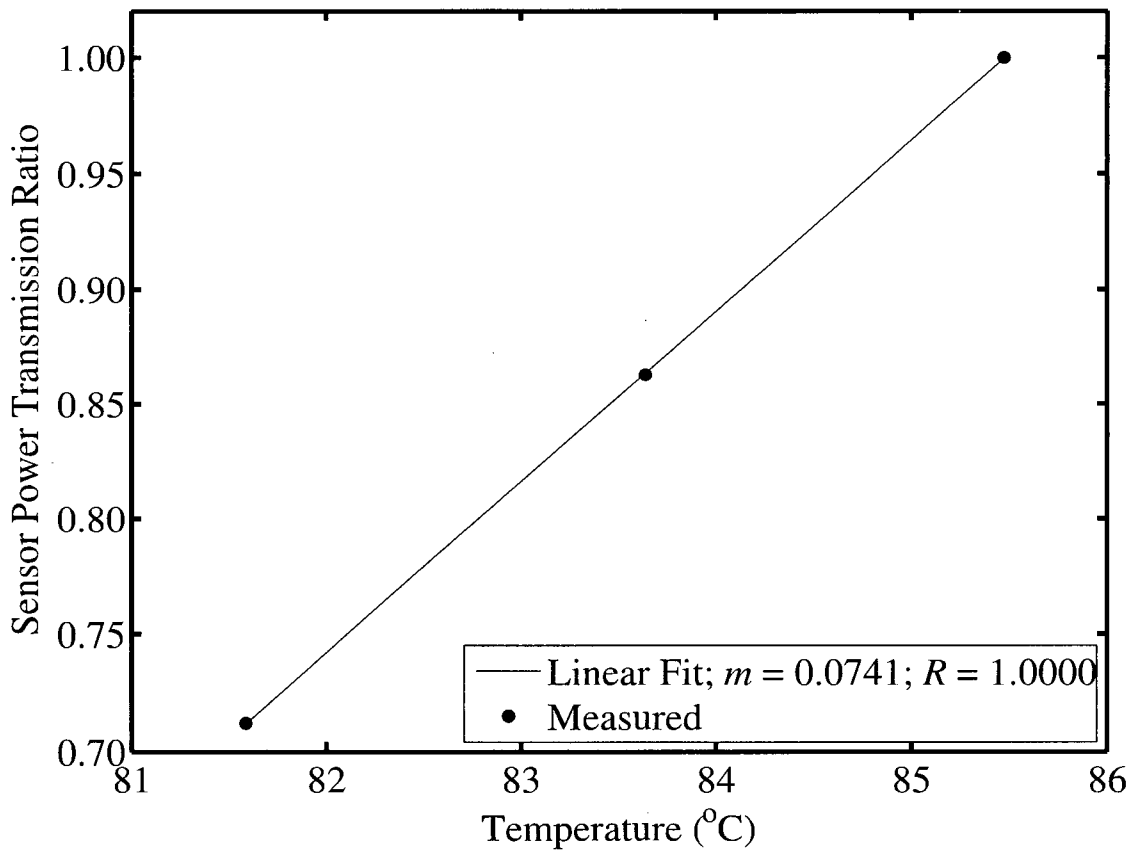

Figure 5-3: Measured power transmission ratio of Sensor-A in Region I along with linear fit with slope and regression of the linear fit given in the legend.

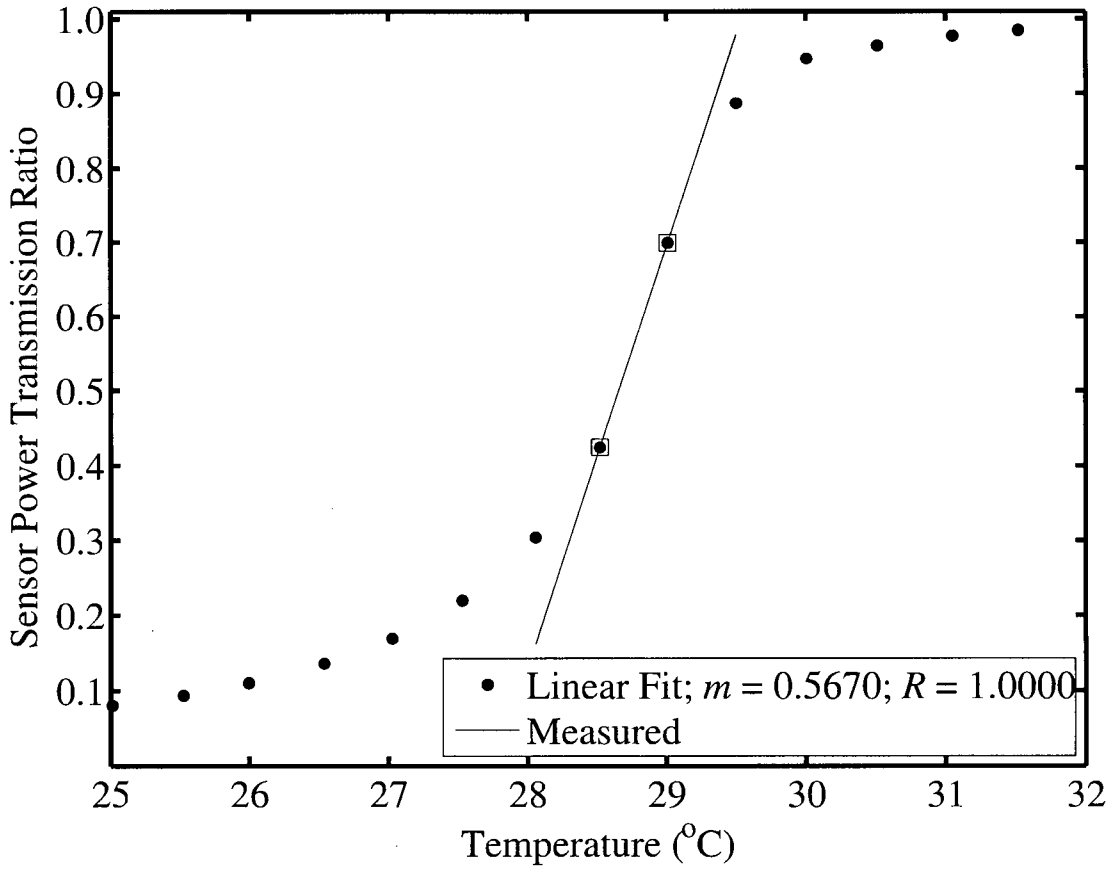

Figure 5-4: Measured power transmission ratio of Sensor-B using OIL-2 along with a linear fit of data points in Region I.

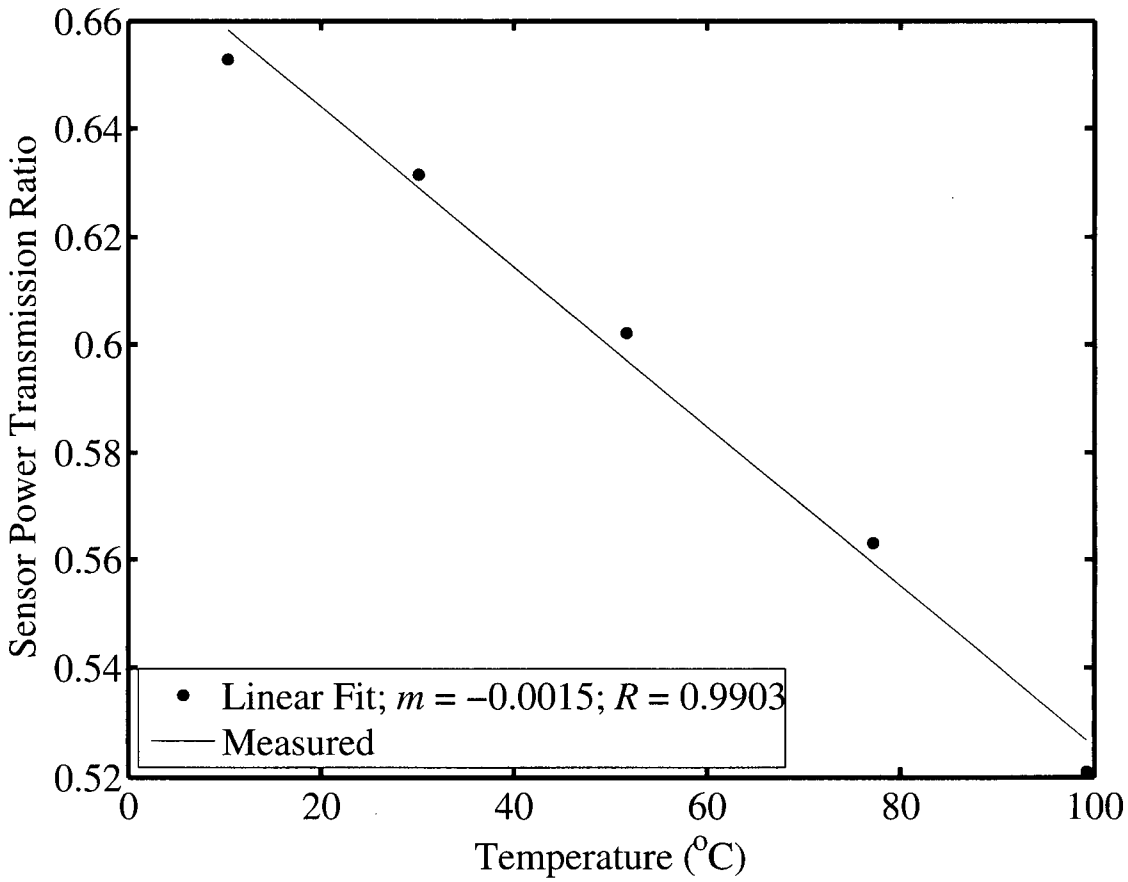

Figure 5-5: Measured power transmission ratio of Sensor-C using OIL-3 along with a linear fit to the data.

Chapter 6

6 Electric Field Sensor

6.1 Introduction

Optical electric field sensors are normally used for voltage measurements and were first investigated in the 1970's [83], [84], [85], [86]. Typically, these sensors used electro-optic crystals with free space optical links and components, which have been replaced by their fibre optic and integrated-optic counterparts. However, the sensor heads are typically still crystal based, i.e., the light is coupled out of the fibre, propagates through the crystal (sensor head) and then coupled back into a receiving fibre. This adds cost and complexity to the measurement.

The light travelling through the crystal experiences the linear electro-optic (or Pockels) effect, which causes a linear change in the refractive index of a crystal when exposed to an electric field [87]. Thus the light is phase modulated by the change in refractive index, which can be converted to amplitude modulation using interferometric techniques. Significant work has been carried out at the University of British Columbia on integrated-optic sensors. Passive immersion type devices for high-voltage measurements were proposed by Ahmed in 1981 [88], integrated sensors based on Mach-Zehnder modulators were proposed by Jaeger in 1985 [89], [90] and most recently Jaeger's integrated-optics Pockels cell (IOPC) [91] was used to develop and implement a voltage sensor by Rahmatian *et al.* [92]. There is interest in realising an entirely fibre-based sensor-head which can possibly be achieved using an evanescent wave sensor. The advantage of such a sensor would be its ability to keep the light in the fibre, i.e., removing the need to couple the light in and out.

A significant effort has been directed towards the use of liquid crystals which exhibit electro-optic behaviour. Room temperature liquid crystals are available and have indices of refraction close to and/or similar to those of optical fibres. In particular, chiral Smectic A (SmA*) liquid crystals are ideal as they allow for continuous modulation of their refractive indices via the electroclinic effect, allowing for their use in analog applications (unlike nematic liquid crystals, which require threshold electric fields to cause changes in their refractive indices) [93].

A version of this chapter has been published. Chandani, S.M., Shao, R.-F., Maclennan, J.E. and Jaeger, N.A.F. (2006) In-line D-fiber electric field sensor using chiral liquid crystals in Proc. of SPIE 6343:634317-1-10.

Several devices based on SmA* liquid crystals have been demonstrated such as a continuously tuneable liquid crystal filter using a SmA* liquid crystal as the active cavity material in a Fabry-Perot etalon [94], a continuously tuneable filter based on a Bragg grating in a planar waveguide with a SmA* liquid crystal overlayer [95]. There has also been some effort in electric field sensors using fibres and liquid crystals such as an electric field probe using a polymer dispersed liquid crystal inserted between two multimode optical fibres [96], a liquid crystal cell used to develop an electric field presence detector [97] and electric field measurements, covering a wide range, using a chiral liquid crystal cell placed between two optical fibres, which behaved like a polarizer [98]. However, the above sensors are not in-line fibre devices and require interruption of the light in the fibre and propagation through the liquid crystal.

In this section we present the design, investigation and fabrication of an in-line electric field sensor that uses the D-fibre and SmA* liquid crystals [99], [100]. The flat side of an etched D-fibre is coated with liquid crystals obtained from the Liquid Crystal Materials Research Center at the University of Colorado, Boulder. In Section 6.2 we present the theory of operation for our sensor. In Sections 6.3 and 6.4 we discuss the various aspects of the physical design of the sensor including liquid crystals, and the particular design architecture and fabrication method used for the prototype sensor. In Section 6.5 we show the experimental setup and experimental results of a prototype sensor. Finally, concluding remarks are given in Section 6.6.

6.2 Operating Principle

In order to create an electric field sensor, the external medium placed on the D-fibre should be electro-optic in nature so that an external electric field modifies the refractive index of the external medium causing a change in the D-fibre power transmission. The basic principle of operation is similar to that of the refractive index and temperature sensors described in Sections 4.2 and 5.2, where the zero-field refractive index of the electro-optic material is greater than the mode effective index of the D-fibre.

Typically, a time-varying electric field is sensed and small changes in the refractive index of the electro-optic material are induced by the field. Thus, the imaginary part of the propagation constant for the leaky TE_0 mode of the equivalent planar waveguide, β_j, will change when an electric field, $\hat{E}_{app}$, is applied and can be written as

$$\beta_j = \beta_{jo} + \sigma\left|\hat{E}_{app}\right| \tag{6-1}$$

where β_{jo} and σ are constants based on the zero-field refractive index and properties of the electro-optic material used. For small changes in β_j (i.e., $\sigma|\hat{E}_{app}| << \beta_{jo}$), Equation (2-2) can be linearized and rewritten as

$$T_p = e^{-2\beta_{jo}L} - 2e^{-2\beta_{jo}L}\sigma L\left|\hat{E}_{app}\right| \tag{6-2}$$

The first term in equation (6-2) is the static power transmission ratio of the sensor and the second term is the field dependent transmission ratio. It is apparent that an external electric field leads to changes in the power transmission ratio of the sensor. As alluded to in Section 6.1, liquid crystals are electro-optic in nature and are good candidates for the application in question as they can be used to coat the flat of the D-fibre.

6.3 Physical Design of Sensor

6.3.1 Liquid Crystals

The choice for the electro-optic material to be used depends mostly on its sensitivity to electric fields, compatibility with silica, and frequency response. Liquid crystal materials are a good choice for several reasons. They are well understood, are readily available, have refractive indices close to that of silica, and can respond to frequencies from DC into the MHz range.

Liquid crystals are materials that show mesophases between the isotropic liquid and the crystal phases of the material which occur over well-defined temperature ranges. The material is typically made of rod like molecules that have some molecular ordering which can be affected by external electric fields. The average direction of the molecules is known as the director, $\tilde{n}$, and the optic axis is parallel to $\tilde{n}$. Liquid crystals are anisotropic materials with extraordinary refractive index, n_e, along $\tilde{n}$ and ordinary refractive index, n_o, perpendicular to $\tilde{n}$. When an electric field is applied, the director can be rotated and, thus, the refractive index seen by polarized light can be modified.

The liquid crystals (LCs) being proposed for this work are chiral (indicated by the 'asterisk' sign) smectics. In the smectic A (SmA*) phase, in particular, LCs form a layered structure with the molecules aligned parallel to each other within each layer, so that the director is normal to the layer interfaces. The layer thickness is of the order of one molecular length. Application of an electric field perpendicular to the molecular axis causes a tilt of the director away from the layer normal by the electroclinic effect [101]. The molecular tilt results in an induced polarization

along the applied electric field. The tilt angle, θ, is linear with the applied field, up to a saturation tilt, and is governed by the electroclinic coefficient, χ, and is given as

$$\theta = \chi \left| \hat{E}_{app} \right| \tag{6-3}$$

6.3.2 Design Architectures

The possible design architectures are dictated by how the liquid crystals are aligned along the surface of the fibre flat. There are two ways in which liquid crystals align themselves to surfaces; homogeneous and homeotropic. Homogeneous alignment is when the rod like molecules are aligned parallel to the surface and homeotropic alignment is when they are perpendicular to the surface. Homogeneous alignment can be achieved simply by coating the surface with an appropriate solution, and rubbing it with a soft tissue or a brush – the rod like molecules align themselves along the direction of rubbing. Homeotropic alignment can be achieved using appropriate surfactants on the surface.Figure 6-1 shows the two proposed design architectures that differ only by the alignment of the liquid crystals. For each design, a cross sectional and top view of the D-fibre is shown with the directions of applied field, $\hat{E}_{app}$, n_o, n_e and $\tilde{n}$ indicated for each of the views. Since the LC is uniaxial, the two orthogonal modes of the fibre experience different indices and propagation constants.

In Design 1 the liquid crystals are homogeneously aligned at an angle θ_o with respect to the fibre axis. An electric field applied normal to the D-fibre flat rotates the liquid crystal molecules by a small angle $\delta\theta$. Consequently, the fibre mode that is polarized perpendicular to the fibre flat always sees n_o and its propagation constant is not affected by the applied field. Hence, only the fibre mode that is polarized parallel to the fibre flat, i.e., the ${}_oHE_{11}$ mode need be launched. The ${}_oHE_{11}$ mode sees $n_\theta(\theta_o \pm \delta\theta)$ depending on the direction of $\hat{E}_{app}$, where

$$n_\theta(\theta) = \frac{n_e n_o}{\sqrt{n_o^2 \sin^2\theta + n_e^2 \cos^2\theta}} \tag{6-4}$$

and θ is the angle between the polarization direction of the light and the optic axis [102]. n_θ is set to an operating point by fixing θ_o so that small changes of $\delta\theta$ by the electroclinic effect results in changes in n_θ, which results in changes in the power transmission through the sensor.

Design 2 shows the liquid crystals homeotropically aligned so that the molecules are oblique to the fibre flat surface at an angle θ_o. In this case, an electric field applied parallel to the fibre axis is needed to exploit the electroclinic effect. Both fibre modes see refractive indices that

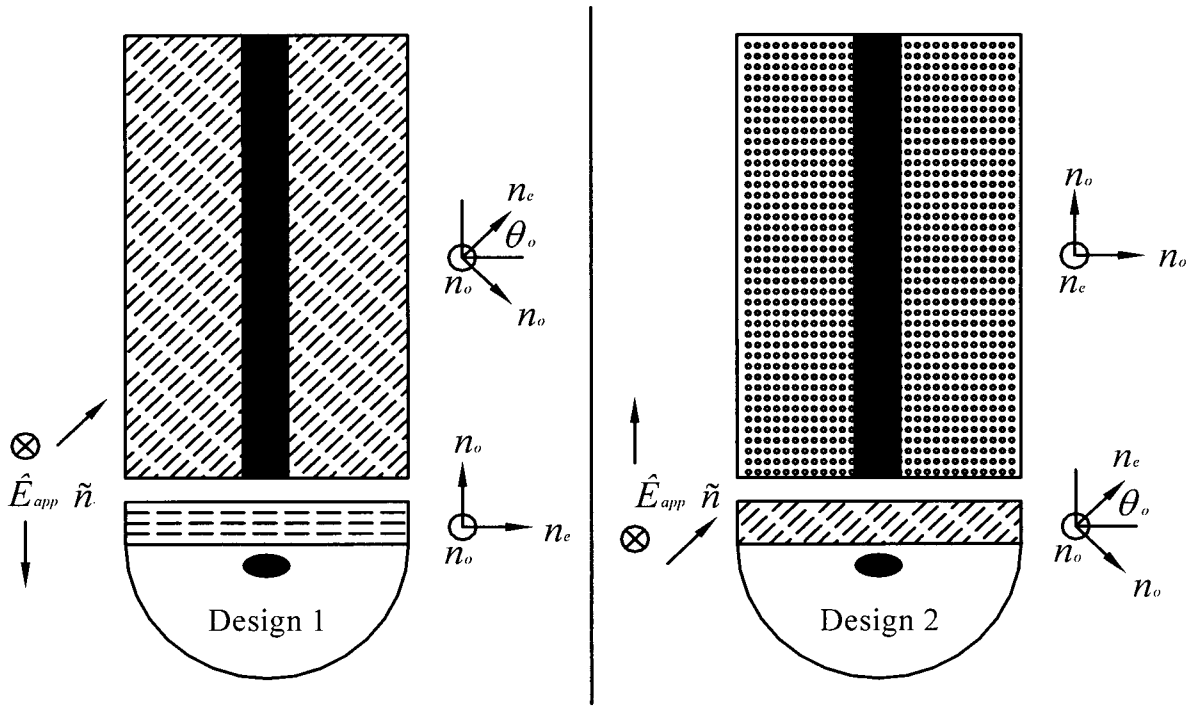

Figure 6-1: Proposed design architectures for electric field sensor using liquid crystals as external medium. Design 1: Homogeneous alignment; Design 2: Homeotropic alignment

change due to the applied field. One mode sees an increase in the refractive index while the other sees a decrease, which leads to a push-pull configuration. To achieve a good operating point, the liquid crystal molecules would have to be aligned at 45° with respect to the fibre flat surface. Such alignment of liquid crystals is very difficult and requires additional complex processing steps. Consequently, Design 1 was chosen for the sensor presented in this work. Additionally, the liquid crystals that were readily available to us had both n_o and $n_e > n_{eff}$ so that the sensor operated in Region III of its power transmission curve.

It should be pointed out that because the two fibre modes see different refractive indices opens up the possibility of designing an interferometric sensor in which both the modes are excited and propagate with different propagation constants. A liquid crystal would have to be engineered to have n_o and $n_\theta < n_{eff}$ so that both modes are guided and only the ${}_oHE_{11}$ mode propagation constant would be affected by the electric field. In such a sensor, interference of the two modes at the output of the sensor would be used to detect the electric field, similar to what is done in crystal-based electric field sensors.

6.4 Fabrication Techniques

To fabricate a sensor, a film of properly aligned liquid crystals must be placed over the flat of the D-fibre. This can be achieved using several techniques. Here we describe the technique used to fabricate the prototype sensor developed in this work. Figure 6-2 shows the cross section of the fabricated sensor. In order to apply an electric field, the sensor was sandwiched between two electrodes; an aluminium base and an indium tin oxide (ITO) coating on a top cover glass. The D-fibre was etched for ~150 min so that the cladding thickness was reduced to ~ 5 μm, which provides an appreciable loss as seen in Figure 4-1. Details of etching a D-fibre are given in Section 3.2. The etched section of the D-fibre was bonded, with its flat side facing up, into a groove machined into a plastic cover slip. W415, the liquid crystal material used, had a SmA* phase between 34.3°C and 24.1°C and an electroclinic coefficient of approximately 1.3 deg/(V/μm) at 30°C [103]. For correct planar alignment of the liquid crystal molecules, coating of both surfaces with a nylon solution and the rubbing of one or both of the surfaces with a brush to force the alignment of the crystals along the rubbing direction is required. The nylon solution was spun onto the fibre flat and onto the ITO coated side of the top cover. The fibre flat was then rubbed with a brush along the fibre axis. The liquid crystal in its isotropic phase (T = 50°C), was

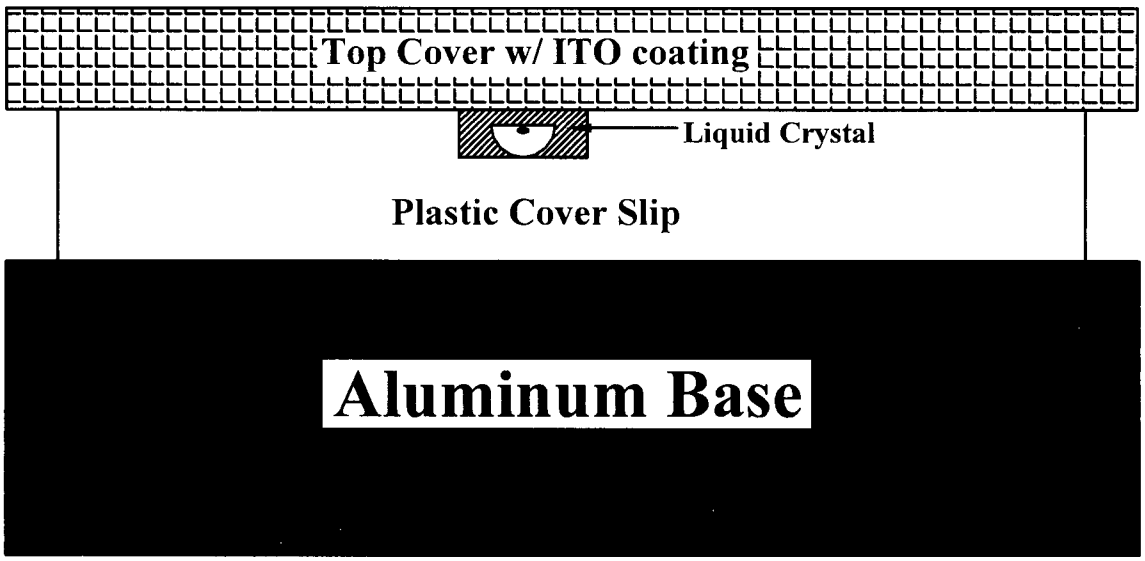

Figure 6-2: Cross section of fabricated sensor showing D-fibre surrounded by liquid crystals.

inserted into the cavity created around the fibre through capillary action and cooled to its SmA* phase (T = 30°C) at a rate of -0.1°C/min.

6.5 Experimental Setup and Results

The experimental setup used to verify the prototype is shown in Figure 6-3. A lock-in amplifier (LIA) was used to apply and detect the electric field. Its output was amplified using a high voltage amplifier capable of applying a maximum of $200V_{pk}$. The frequency of primary interest for high voltage applications is either 50 or 60 Hz, thus here we used a 50 Hz sinusoid.

The temperature of the liquid crystal was set to either 29 or 30°C so that the liquid crystal was in its SmA* phase. The voltage applied to the sensor was ramped up and down in 25 V steps between zero and its peak value of 200 V. Many such ramps were conducted in succession. For each voltage level within a ramp, the LIA signal was sampled every second for 60 seconds and the mean and standard deviation of the 60 samples was calculated. Based on the geometry of the sensor and the field reduction factor due to the induced depolarization field [104], the peak electric field in the liquid crystal layer was estimated to be ~ 0.45 V/μm. Figure 6-4 shows the prototype sensor's response at the two different temperatures. As expected, the sensor's response to a ramped AC applied voltage is linear; however, the slope of the response changed over time. Also shown in the figure is this evolution of slope of the sensor's linear response. To demonstrate the linearity of the sensor, Figure 6-5 shows the curve in Figure 6-4 with the largest slope, along with error bars and a linear fit. The error bars are the standard deviation of the mean of the samples taken at each voltage level.

Obviously, this time dependent change in the signal is unwanted and unexpected. As mentioned earlier, the alignment of the liquid crystal molecules is very important and this drift in the sensitivity is due to the improper alignment of the liquid crystals on the fibre surface. The surface alignment techniques used for this particular liquid crystal were developed for both surfaces being ITO coated, whereas in the present case, one surface was the fibre flat which was fluorine-doped silica. The slope of the sensor's response starts off small and increases to a peak. This initial increase is believed to be due to the application of the electric field over time, which forces or aids some improperly aligned molecules to align themselves with any properly aligned neighbouring molecules. The alignment process used was also developed for liquid crystal film thickness on the order of 1–5 μm, as is the case in the majority of liquid crystal applications, such as in display applications. In our case, the molecules were confined

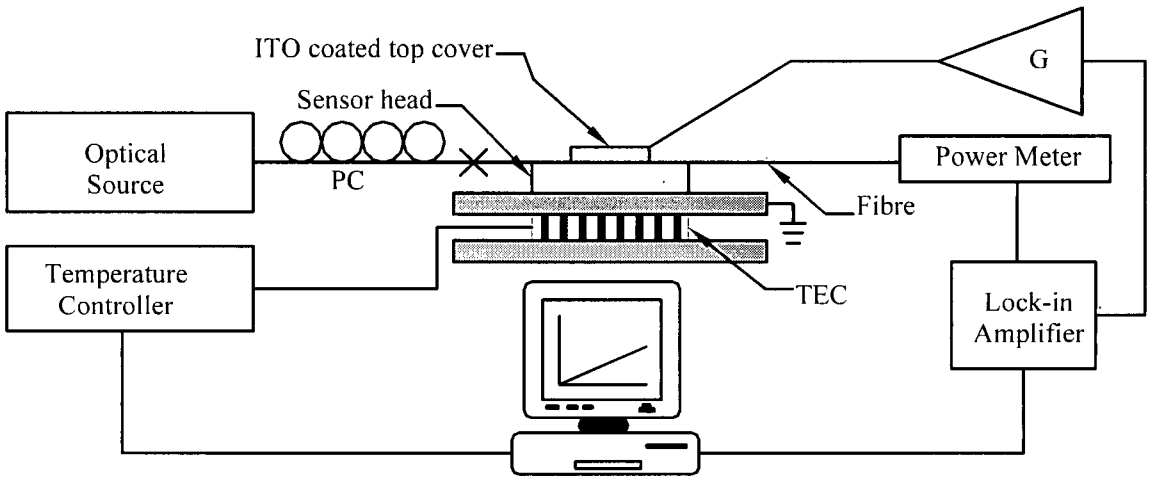

Figure 6-3: Experimental setup used to measure response of prototype electric field sensor. TEC-Thermoelectric Cooler; x-Fibre splice; PC-Polarization Controller; G-High Voltage Amplifier.

to a spacing of > 20 μm, which could have affected the alignment of the molecules. However, even with a smaller spacing, it is still believed that the surface of the fibre flat would lead to improper alignment. It is evident that further surface alignment process development is necessary to optimally align the liquid crystals on the fibre flat. In particular, surface alignment studies using fluorine-doped silica or undoped silica are required to assure that the liquid crystals are aligned as expected. Nevertheless, having shown proof of principle, such a sensor would be ideal for the measurement of high voltages in power substations. By having a sensor run down the length of high voltage column, it would be possible to get a true measure of the line integral of the electric field, which results in the measurement of the voltage. In any case, it is still unclear whether a liquid crystal with a large temperature range can be engineered for the targeted application of high voltage measurements in power substations.

6.6 Conclusions

In this section a design for an in-line electric field sensor using power attenuation in etched D-fibres and chiral liquid crystals was presented. Fabrication and testing of a prototype showed proof of principle. The sensor responded linearly to an applied electric field and had a peak sensitivity of 0.2 mV/(V/μm), but the sensitivity changed over time. The drift in sensitivity was due to the improper alignment of the liquid crystals on the fluorine-doped silica surface. Further surface alignment studies and the development of an alignment process is required. Nevertheless, it can be concluded that such an integrated all-fibre electric field sensor can be fabricated if an ideal liquid crystal can be engineered for the targeted application.

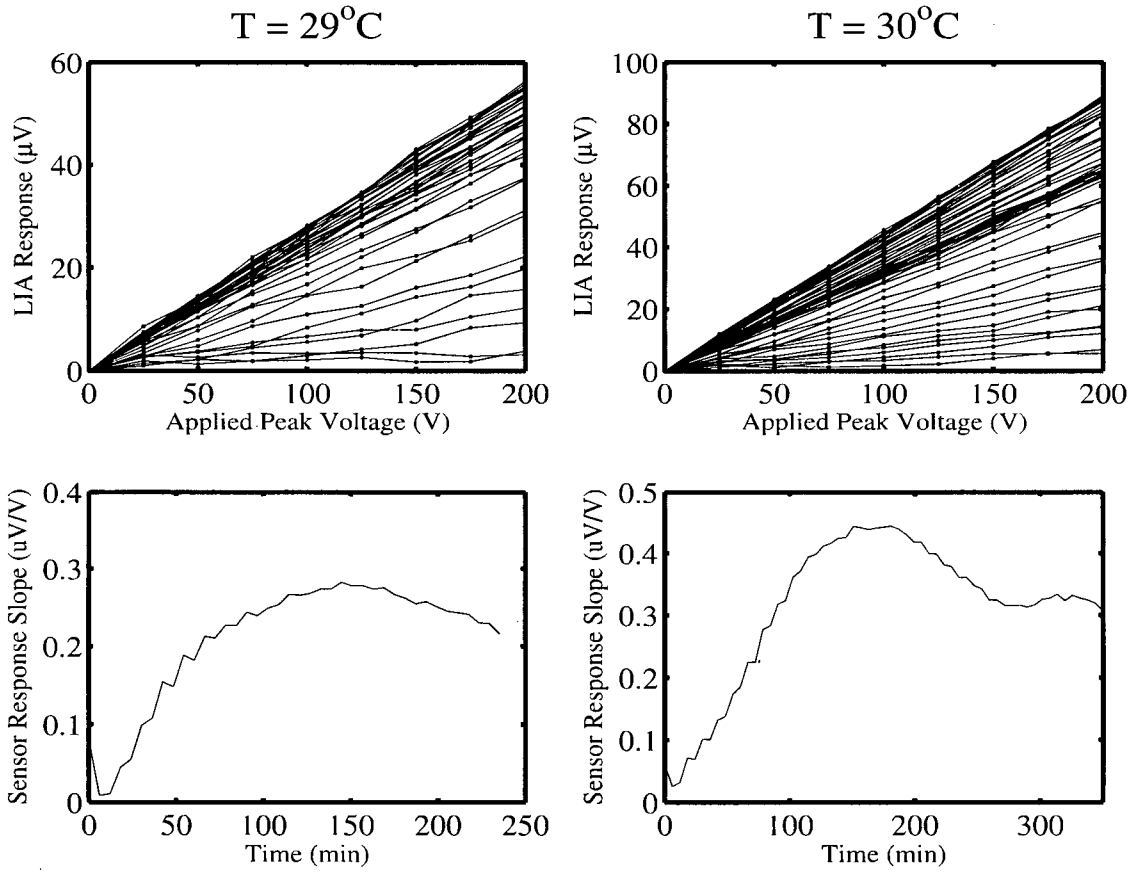

Figure 6-4: Prototype sensor response to voltage ramps for liquid crystal temperatures of 29 °C and 30°C along with slope of sensor's linear response.

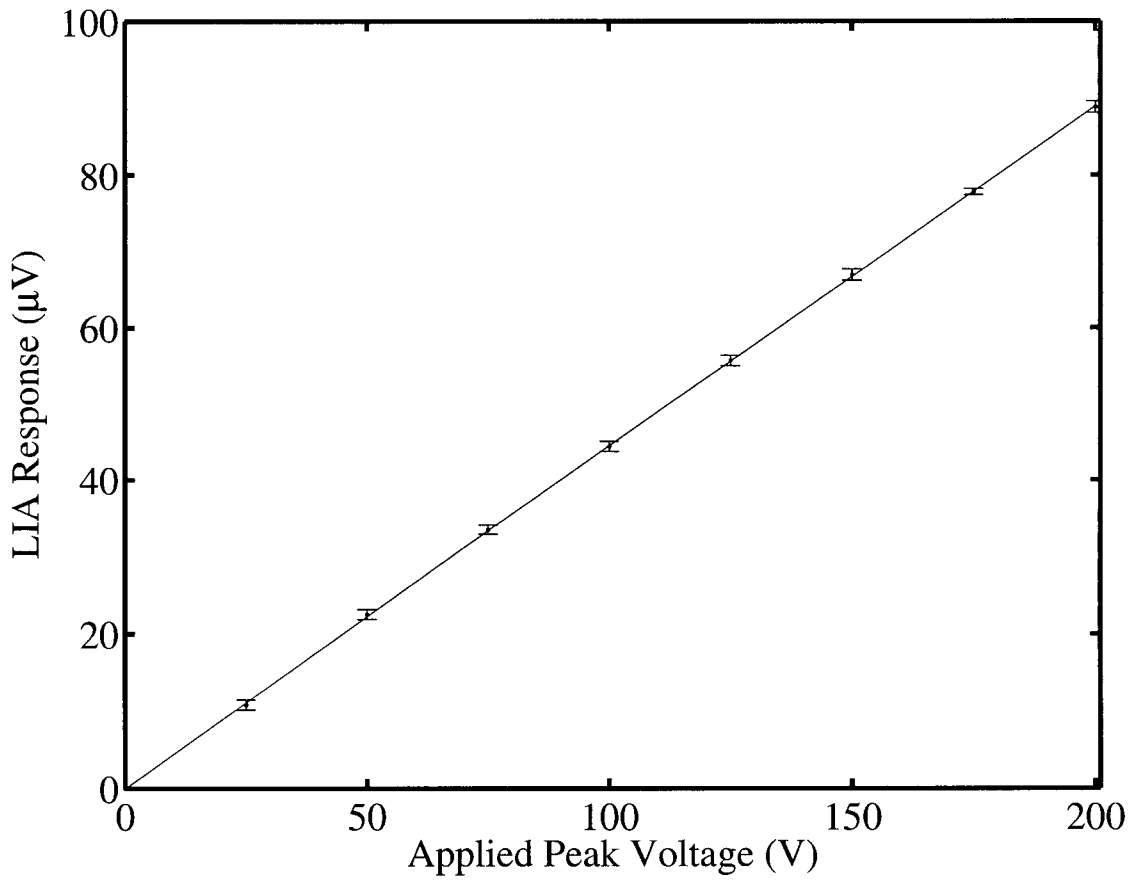

Figure 6-5: Sensor response with the largest slope along with error bars and linear fit

Chapter 7

7 Liquid Level Sensor

7.1 Introduction

There two main advantages of fibre optic sensors that make them attractive for use as liquid level sensors i.e., they are made from non-conducting (dielectric) materials and they are corrosion resistant. The former advantage is particularly attractive for applications in explosive environments and flammable atmospheres while the later is attractive for chemical processing applications. A specific liquid level application that is well-served by these two advantages is in sensing of flammable hydrocarbons or fuels and of chemicals in industrial and processing plants. For these reasons, there has been a significant amount of research into optical liquid level sensors [105]-[120].

Liquid level sensors can be classified into two main categories; continuous level sensors and discrete level sensors. Several continuous level sensors have been demonstrated. The coupling between optical waveguides at the surface of a liquid using six fibres and a reflecting array comprised of steel wires was demonstrated over 40 centimetres with a resolution of 6 mm [105]. A sensor using two specially treated plastic optical fibres immersed in a quartz tube filled with an intermediate liquid (such as water) was developed for any liquid with refractive index equal to or greater than 1.33 over 12 centimetres with a resolution of ~6 mm [106]. The refractive index sensitivity of long-period fibre optic gratings has been exploited over 24 millimetres with a resolution of 0.2 millimetres, but suffered limitations such as the need to use a specific wavelength, a linear response over only about 60% of the grating's length and a limiting restriction on the liquid's refractive index range to 1.400-1.456 [107]. A sensor based on the optical attenuation in a plastic optical fibre where the liquid acted as a second cladding was demonstrated over 2 metres with a resolution of 2 millimetres [108].

Some systems measure the reflected light off of the surface of the liquid using multiple fibres with collimating optics to measure the liquid surface proximity [109], [110]. Three fibres, a transmitting, receiving, and reference fibre were used to measure liquid levels over a 70-170

A version of this chapter has been accepted for publication. Chandani, S.M. and Jaeger, N.A.F. (2007) An optical fiber-based liquid level sensor, Optical Engineering (5-6 pages).

millimetre range with a resolution of 10 mm [109]. Alternatively, in [110], two plastic optical fibres were used to measure levels over a 2 metre range with a 10 millimetre resolution. Ladar techniques have also been demonstrated whereby the phase difference between a light beam reflected off the liquid surface and a reference beam is used to measure the liquid surface proximity [111], [112], [113]. The above systems require the placement of transmitting and receiving fibres and/or collimating optics at a fixed point above the liquid surface. The light can undergo undesired reflections or refractions due to ripples on the liquid's surface leading to errors.

In contrast, discrete level sensors are typically based on the change in optical reflection from or transmission through the sensor head, due to the change in refractive index surrounding the sensor head, when immersed in a liquid. Examples of such sensors are based on the coupling of cladding modes from a lead-in fibre to a lead-out fibre [114], on frustrated total internal reflection experienced in fibres with angled or retroreflecting tips [115] or conical/tapered tips [116], on total internal reflection experienced in fibres with reflecting elements such as prisms [117] or specially designed tips [118] cemented to their ends, and most recently on transmission through two fibres integrated using a hemispherical transparent dielectric element [119]. In each of the above cases, the sensor has been implemented as an on-off switch, or as an array of sensors placed along the wall of the liquid vessel, or on a mechanical assembly that translated the sensor up and down the liquid vessel. Thus, to achieve high resolutions, an array of many sensors (e.g. 140 in [119]) or some additional moving mechanism is needed, which adds to the cost and complexity of the level measurement.

Betta *et al.* have demonstrated a quasi-continuous sensor based on "unclad zones" on a plastic clad silica fibre where the cladding has been reduced in these zones to cause optical attenuation when surrounded by a liquid [120]. Using six fibres, each with 63 unclad zones, a 1 m full-scale, 4 mm resolution prototype was realized and tested. The sensor length is limited due to the fact that the power attenuation of each unclad zone is less than that of the previous zone so that, as the liquid level rises, the change in optical power becomes comparable to the noise amplitude.

In this section we describe and demonstrate a liquid level sensor that is based on the power attenuation experienced in an etched D-fibre [121]. The sensor can be realized as a continuous level sensor or as a discrete level sensor. In either case the use of only one fibre, one optical source and one detector is needed. In Section 7.2 we present the operating principle of the sensor. In Section 7.3 we demonstrate the sensor by fabricating a prototype and describe its static

and dynamic characterization. Comparison to existing sensors and concluding remarks are given in Section 7.4.

7.2 Operating Principle

As discussed and demonstrated in previous sections, power attenuation exists in the etched D-fibre if the surrounding refractive index is greater than the mode effective index, n_{eff}. Among other factors, the power transmission ratio, T_P, of the D-fibre depends exponentially on the length of the etched section that is surrounded by the external medium and is given as

$$T_P = \frac{P_{out}}{P_{in}} = e^{-2\beta_j L} = e^{-\gamma L} \tag{7-1}$$

where P_{in} and P_{out} are the optical powers into and out of the sensor head, respectively, L is the length of the sensor head that is surrounded by the liquid, and $\gamma = 2\beta_j$, is the power attenuation coefficient, which can be determined analytically using the model described in Chapter 2.

Thus, a liquid level sensor can be realized by running an etched D-fibre along the wall of a liquid vessel and monitoring the power transmission ratio, which would decrease with an increasing liquid level and vice versa for a decreasing level. Such a distributed sensor is advantageous as it only requires one piece of fibre, and one optical source and detector. Figure 7-1 shows a conceptual diagram of the liquid level sensor lining a vessel with a liquid of refractive index, n_{liq}, and the cross section of the D-fibre used.

Figure 7-2 shows the calculated power attenuation coefficient for the elliptical D-fibre's fundamental mode (the ${}_0HE_{11}$ mode as defined in [32], [33]) as a function of the liquid refractive index for four values of the cladding thickness at $\lambda_o = 1550$ nm. The power attenuation coefficient peaks sharply close to the fibre mode's effective index and then monotonically decreases for larger refractive indices. For $n_{liq} < n_{eff}$, the power attenuation coefficient, γ, is zero and there is no power lost from the sensor head due to contact with the liquid (as is typical with optical fibres, there are intrinsic losses due to other mechanisms such as scattering and absorption; however, these are negligible over short lengths). The power attenuation coefficient curves can be shifted to the left by increasing λ_o. For example, Figure 7-3 shows the calculated attenuation coefficient using $\lambda_o = 1650$ nm. It is apparent from Figure 7-2 and Figure 7-3 that the proposed sensor can be designed and operated such that it can be used with any liquid for which $n_{liq} > 1.45$. This is a favourable result considering that the refractive indices of many liquid

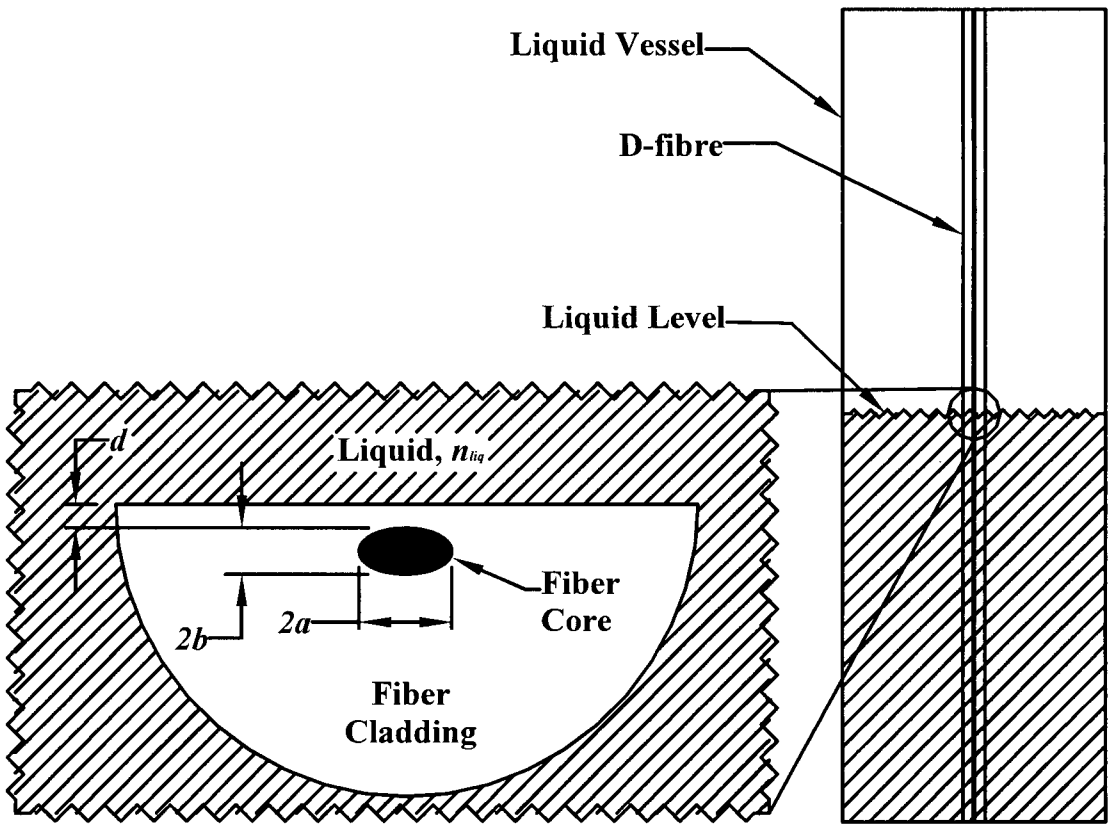

Figure 7-1: Conceptual diagram of liquid level sensor lining a vessel holding a liquid having refractive index, n_{liq}, with the cross section of sensor head showing an elliptical core of semimajor axis a and semiminor axis b, and cladding thickness d.

hydrocarbons and other industrial liquids are in the range from 1.45 to 1.55 [106], [122]. Changes in the liquid refractive index (for example, due to temperature fluctuations) could lead to errors since the attenuation coefficient is sensitive to the liquid refractive index. At the peak of the attenuation curves in Figure 7-2 and to their right, the sensitivity of γ to n_{liq} is moderate. Most liquids have thermo-optic coefficients on the order of 10^{-4} RIUs/°C and thus a change in temperature of 10°C would lead to a change in n_{liq} of 10^{-3}. Such a change would lead to a negligible change in γ and thus a negligible change in T_P. However, for liquids that have $n_{liq} \gtrsim n_{eff}$, the sensitivity of γ to n_{liq} is greater and temperature changes can lead to changes in T_P. Nevertheless, in an industrial application, compensation techniques commonly used with intensity-based optical fibre sensors can be applied [123].

Equation (7-1) has been used to calculate the sensor's power transmission ratio at $\lambda_0 = 1550$ nm and is shown in Figure 7-4 as a function of the liquid level for several values of n_{liq} using $d = 7.5$ μm. Here, a cladding thickness of 7.5 μm was chosen to give a nearly linear response over the length of the sensor. The sensitivity of the sensor, i.e., the slope of the response ($\partial T_P/\partial L$), depends on γ and thus, depending on the application, the sensor response and its sensitivity can be tailored by carefully selecting the cladding thickness to yield a desired value for γ for a particular n_{liq}. It should be noted that the average slope of the response for a particular d decreases as n_{liq} increases. In general, it is not necessary to have a linear sensor. For a given length of sensor, if the power attenuation coefficient is high (due to a smaller cladding thickness), the sensor response becomes exponential and remains relatively linear for low liquid levels. In addition, the sensitivity decreases with increasing liquid levels for such an exponential sensor. Nevertheless, such a sensor may be advantageous for applications requiring a high sensitivity for low liquid levels and a lower sensitivity for high liquid levels. The sensor can also be realized as a discrete level sensor for applications that have high liquid levels and require low resolutions. Short sections of the fibre (e.g., 1 mm) could be etched at regular intervals (determined by the required resolution) so that they all yield the same attenuation and the sensor response would then be a stair-like function, each step corresponding to a discrete liquid level. Such a discrete sensor requiring only one fibre, one source and one detector results in a significant decrease in the complexity and cost as compared to existing discrete level sensors that require multiple sensors, lead-in and lead-out fibres, sources and detectors [114], [117], [119] or moving mechanisms [115], [116], [118].

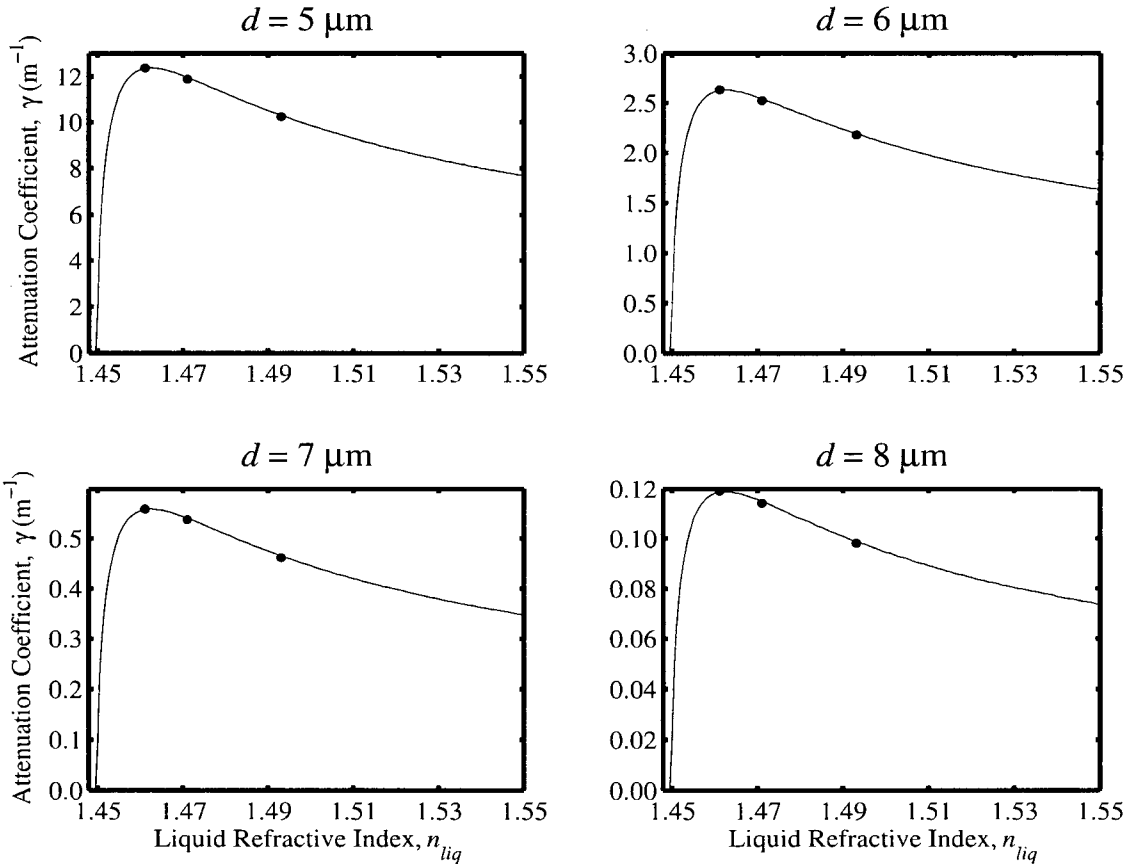

Figure 7-2: Calculated power attenuation coefficient for the ${}_oHE_{11}$ mode as a function of liquid refractive index for four values of d using $a = 2$ μm, $b = 1$ μm and $\lambda_o = 1550$ nm. Solid circles indicate points of interest.

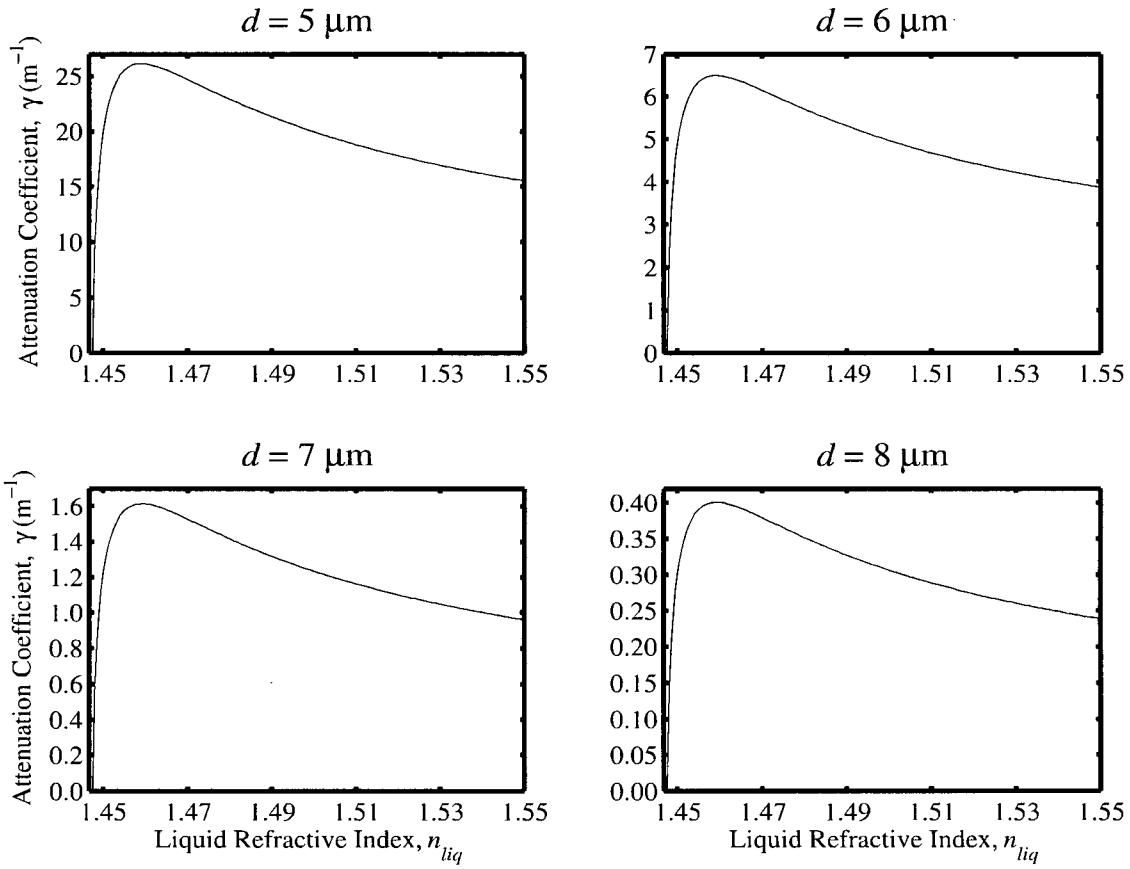

Figure 7-3: Calculated power attenuation coefficient for the ${}_oHE_{11}$ mode as a function of liquid refractive index for four values of d using $a = 2$ μm, $b = 1$ μm and $\lambda_o = 1650$ nm.

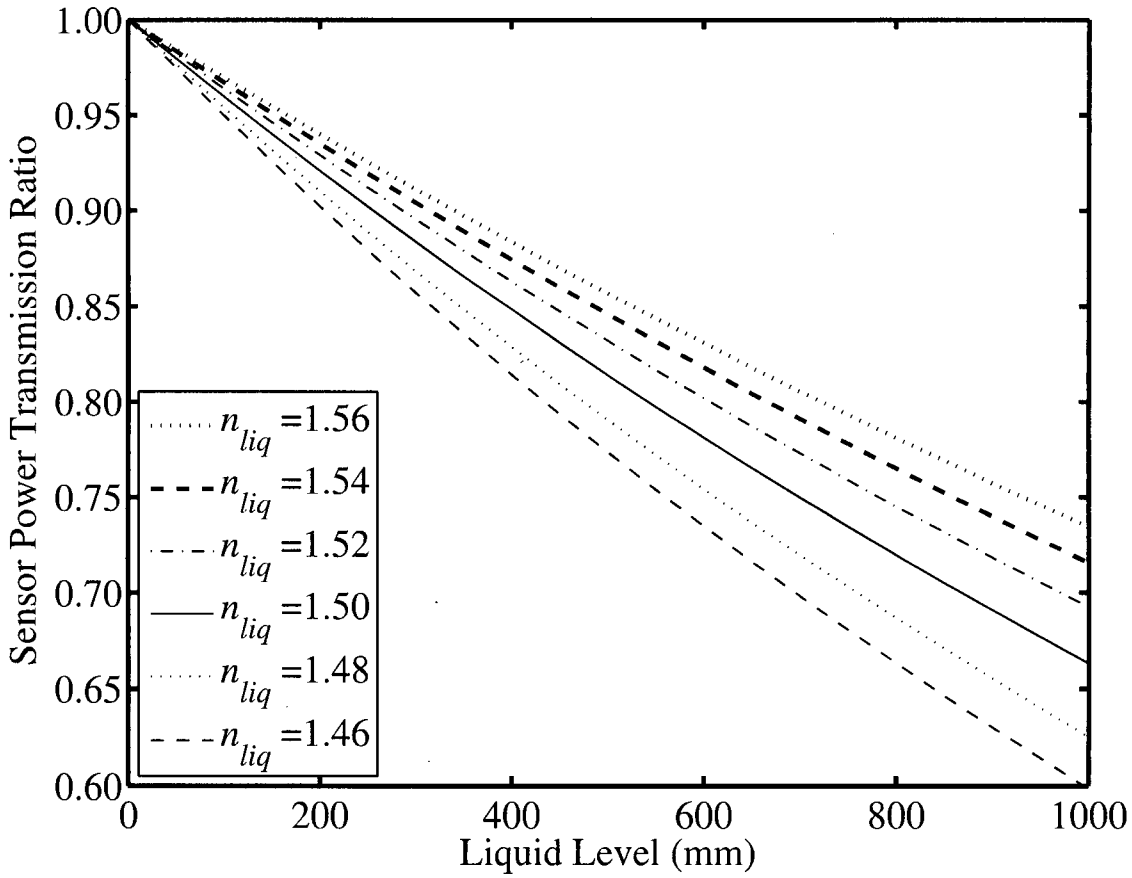

Figure 7-4: Calculated liquid level sensor power transmission ratio as a function of liquid level for several values of n_{liq} using d = 7.5 μm, a = 2 μm, b = 1 μm and λ_o = 1550 nm.

7.3 Experimental Setup and Results

To fabricate the proposed sensor, a 19 to 20 mm unjacketed section of our D-fibre was etched in a 10% BHF solution for ~170 minutes to decrease the cladding thickness to between 5 and 6 μm. As will be seen later, this was done to achieve a power attenuation coefficient that would result in a linear sensor response over its length. Standard thermo-optic oils were used as the liquids so that their temperatures could be used to accurately control their refractive indices.

The experimental setup in Figure 7-5 shows the D-fibre running down the centre of a specially built square aluminum tank, which had a transparent window along one of its walls with a scale, in mm, to read the liquid level. A plugged hole at the bottom of the tank allowed the routing of the fibre to the power meter. Alternatively, as in [108], the fibre can be looped back to the top of the tank so as to make a 'U' shape. In this case, however, only one side of the 'U' shape needs to be etched to create the sensor head. The other side of the "U" shape serves to direct the modulated light back to the power meter with negligible power loss. The liquid was inserted into the tank using a syringe. To accurately control the liquid level (by either introducing or extracting a small amount of liquid) the end of the syringe's plunger was attached to an automated translation stage. The aluminum tank was placed on a temperature stage so that the liquid's temperature, and hence its refractive index, could be controlled throughout the experiment. A 1550 nm monochromatic optical source was used and the light was coupled into the sensor from a standard SMF-28 fibre using a mechanical splice. A polarization controller was inserted between the optical source and the sensor so that the fundamental $_{o}HE_{11}$ mode of the D-fibre could be launched. To confirm that the $_{o}HE_{11}$ mode was launched, a polarizer placed at the output was used to measure the extinction ratio of the light, which was always in excess of 27dB. The output of the fibre was directed onto a power meter. To measure the power transmission ratio, the output power of the sensor was recorded with a liquid level of zero, i.e., air surrounding the sensor head. This power level was used as the reference to calculate the power transmission ratio so that for a liquid level of zero, $T_P = 1$. Thus, when the liquid level increases, the power transmission ratio decreases and thus becomes less than one. In this way, we normalize out the power losses due to other mechanisms such as intrinsic attenuation and absorption in the D-fibre. The characterization of the sensor was split into 1) static characterization and 2) dynamic characterization.

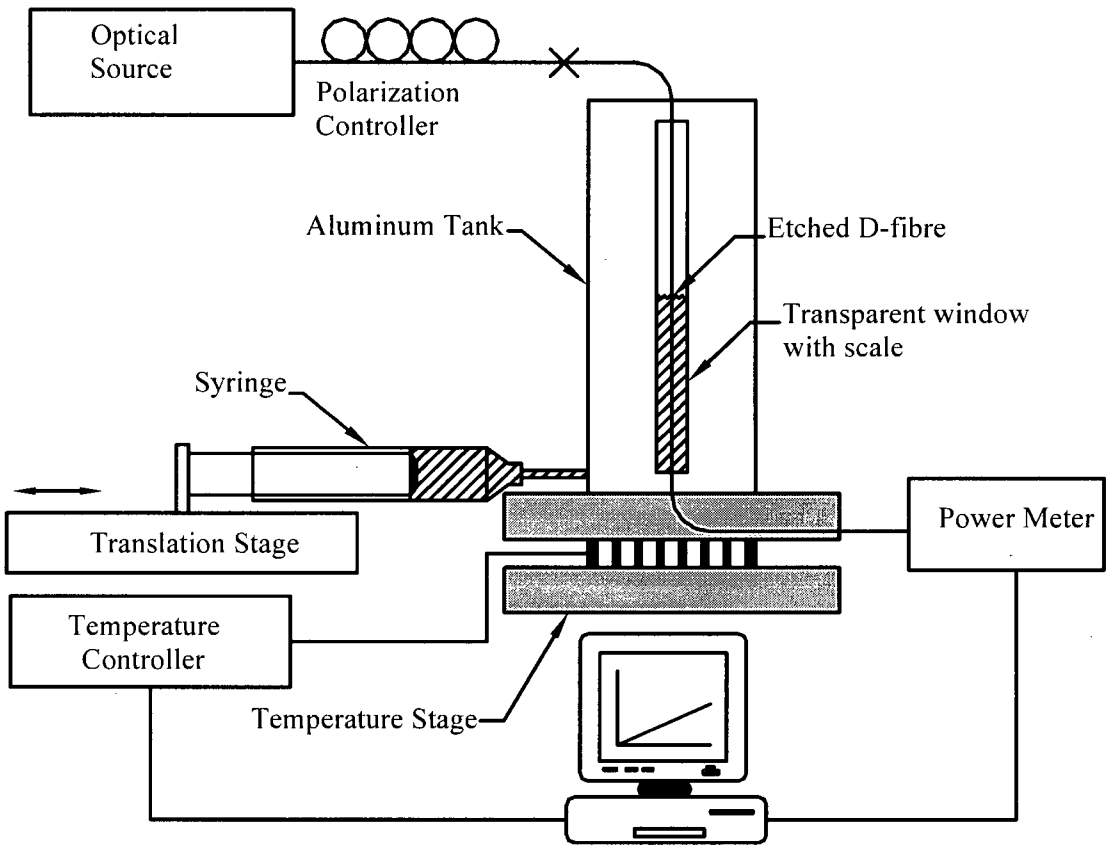

Figure 7-5: Experimental setup showing D-fibre running down center of aluminum tank with sensor head in the middle of tank. The 1550 nm optical source is used to couple light via a polarization controller into the sensor. The syringe on the translation stage is used to change the liquid level.

7.3.1 Static Characterization of the Sensor

The static characterization was carried out by measuring the sensor's response to increasing and decreasing liquid levels, which were changed in 2 mm steps. At each liquid level, the power level was measured and the power transmission ratio was calculated as described earlier. The response was measured at three values of refractive index achieved using two oils. OIL-1 had an index of refraction at 25°C, n_0, and thermo-optic coefficient, dn/dT, of 1.471 and -3.86×10^{-4}/°C, respectively, and OIL-3 had $n_0 = 1.493$ and $dn/dT = -3.91\times10^{-4}$/°C, all at $\lambda_o = 1550$ nm. The third refractive index was achieved by using OIL-1 at 50°C which resulted in an index of refraction of 1.461. These three values were chosen because they approximately occur at points of interest on the power attenuation coefficient curve of our D-fibre (indicated by solid circles in Figure 7-2), i.e., $n_{liq} = 1.461$ occurs near the peak of the curve, $n_{liq} = 1.471$ occurs near where the slope of the curve to the right of its peak is steepest and $n_{liq} = 1.493$ occurs near the middle of the range 1.45-1.55 for typical hydrocarbons and other industrial liquids. Figure 7-6 to Figure 7-8 show the sensor's measured power transmission ratios using liquids with the three refractive index values above. Shown in each figure is the response to an increasing and a decreasing liquid level. Each response has been fit to a line to illustrate the sensor's linearity with the fitted line's slope, m, and regression coefficient, R, given in the legend. The calculated slopes for the increasing and decreasing liquid levels differ by ~1% in each case, demonstrating that the sensor has virtually identical responses for increasing and decreasing liquid levels. The regression coefficients for the linear fits are all greater than 0.99 signifying the sensor's linearity. As predicted, the value of the slope decreases with increasing liquid refractive index.

The resolution of the sensor depends on the measurement of the optical transmission, which can fluctuate due to factors such as source temperature changes, detector responsivity changes, link attenuation changes, and those caused by changes in mechanical components such as connectors, mechanical support mounts, and optics [124]. We are able to achieve an optical transmission measurement resolution of 0.2% with no extra effort. This measurement resolution yields a liquid level measurement resolution of ~0.2 mm.

7.3.2 Dynamic Characterization of the Sensor

The dynamic characterization of the sensor was carried out by continuously varying the liquid level at a constant rate. The liquid level was first increased at a particular rate to fill up the tank, thus immersing the entire sensor head. After some time, the level was then decreased at the same rate. This time interval was introduced to demonstrate the power transmission ratio's stability

while the liquid level remained stationary. As the liquid level increased or decreased with time, the sensor's power transmission was sampled every second to calculate the corresponding power transmission ratio. The sensor's response to a dynamically changing liquid level is shown in Figure 7-9 for $n_{liq} = 1.461$ and in Figure 7-10 for $n_{liq} = 1.493$. As seen, the power transmission ratio decreases linearly with increasing liquid level and increases linearly back to one with decreasing liquid level. The dashed vertical lines in the figures separate the three different regions described above.

The rate of change of the liquid level only affects decreasing liquid levels. With increasing liquid levels, the rate is only limited by the optical detection time. However, if the level is decreased rapidly, the sensor's power transmission ratio does not increase linearly, as expected, but fluctuates with time. In fact, in some cases the power transmission ratio decreases to values below the minimum power transmission ratio value (i.e., the power transmission ratio value when the entire sensor head is immersed in the liquid). Figure 7-11 shows an example of the sensor's measured power transmission ratio with a rapidly decreasing liquid level for $n_{liq} = 1.461$. These fluctuations in the sensor transmission ratio are likely due to a thin film of liquid being left behind on the sensor head. It is possible that such a film would likely form a planar waveguide which would interact with, i.e., couple with, the core of the D-fibre [25], [125], [126]. Such coupling would likely be strongly dependant on the thickness and length of the liquid film, both of which would likely change over time, leading to oscillations in the sensor transmission ratio.

7.4 Conclusions

In this section, we have demonstrated a liquid level sensor using the etched D-fibre. Once calibrated, our sensor has a resolution of ~0.2 mm when used as a continuous level sensor and had virtually the same response for increasing and decreasing levels.

Advantages of the reported sensor over other continuous level sensors that use an optical fibre immersed in the liquid [105], [106], [120] is that it only requires one piece of fibre to achieve a high resolution. In [108], where one plastic optical fibre has been used with the liquid acting as a second cladding, the refractive index of the liquid has to be less than the refractive index of the fibre (typically ~1.49 for plastic fibres) to cause total internal reflection, thus placing an upper limit on the liquid's refractive index. The sensor based on the refractive index sensitivity of long-period fibre gratings [107] has a higher resolution; however, its operating

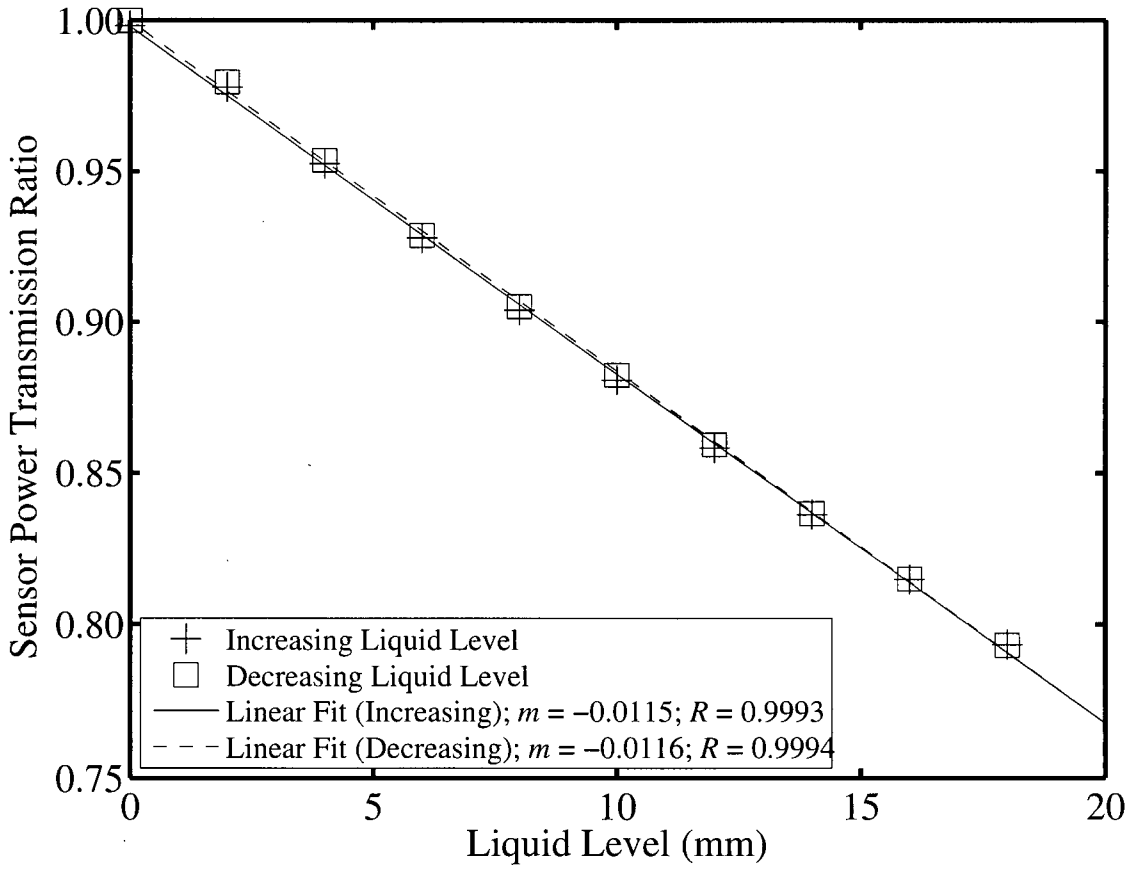

Figure 7-6: Sensor's measured power transmission ratio versus liquid level for $n_{liq} = 1.461$ for increasing and decreasing liquid levels along with linear fits.

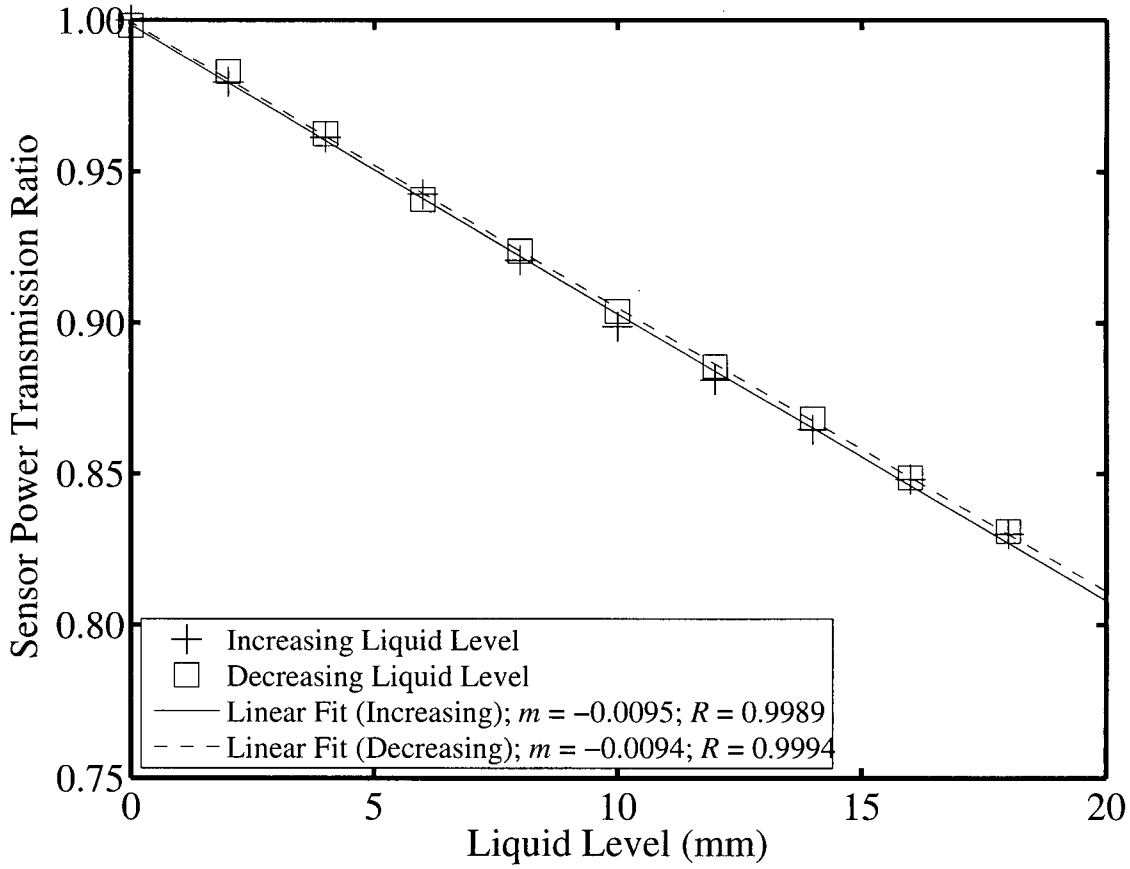

Figure 7-7: Sensor's measured power transmission ratio versus liquid level for $n_{liq} = 1.471$ for increasing and decreasing liquid levels along with linear fits.

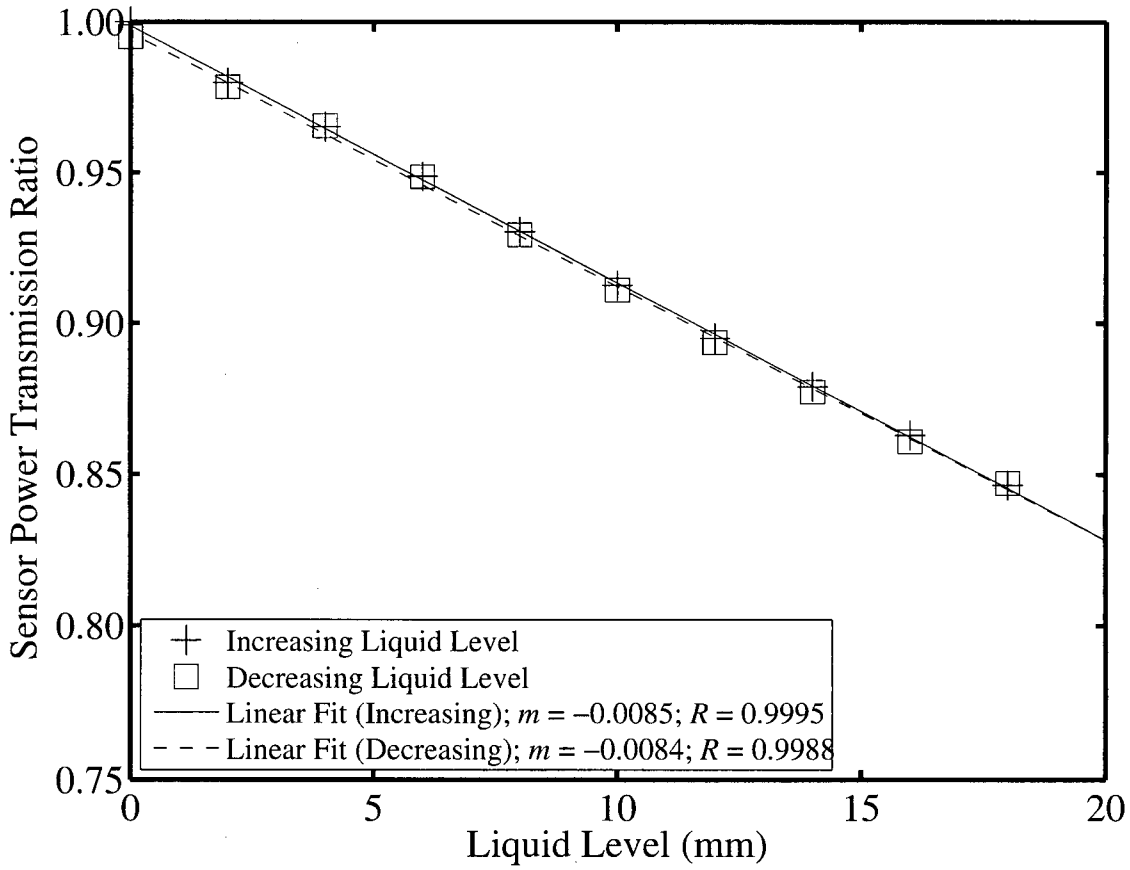

Figure 7-8: Sensor's measured power transmission ratio versus liquid level for $n_{liq} = 1.493$ for increasing and decreasing liquid levels along with linear fits.

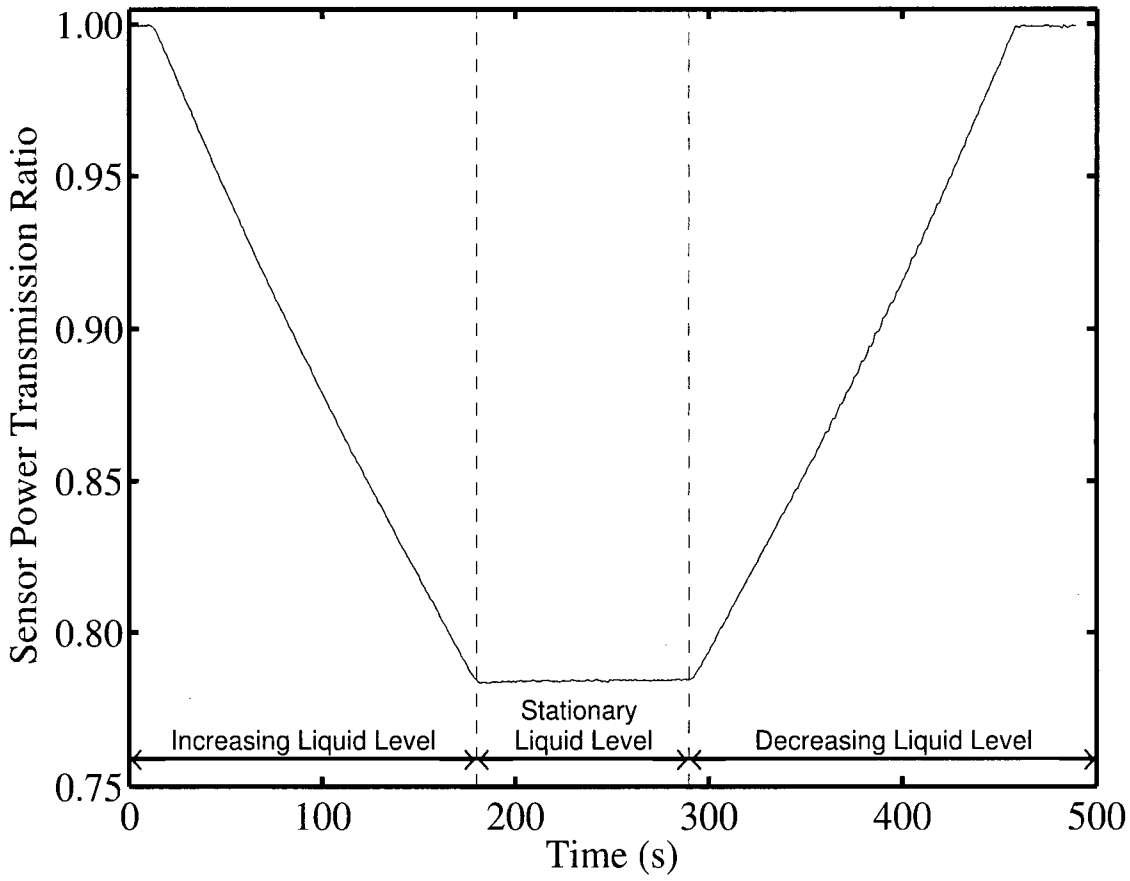

Figure 7-9: Sensor's measured power transmission ratio as a function of time for increasing and decreasing liquid levels for $n_{liq} = 1.461$.

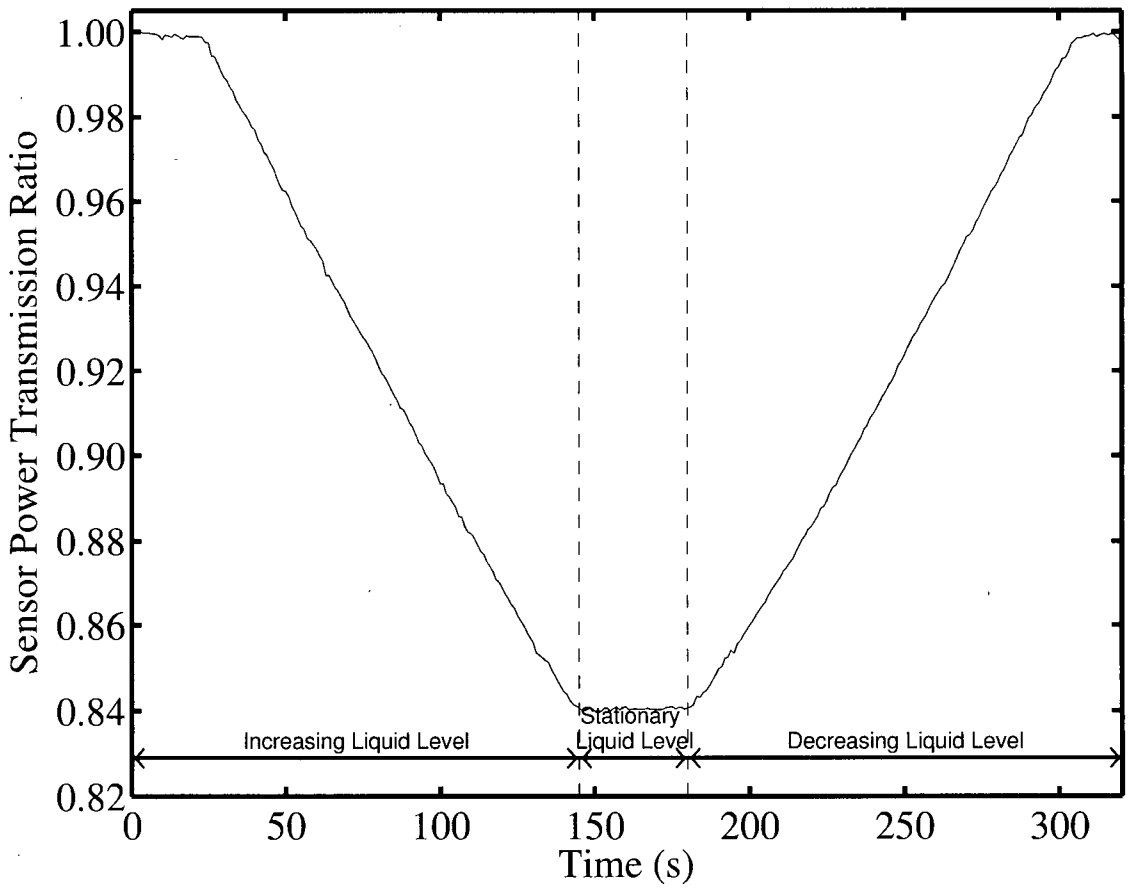

Figure 7-10: Sensor's measured power transmission ratio as a function of time for increasing and decreasing liquid levels for $n_{liq} = 1.493$.

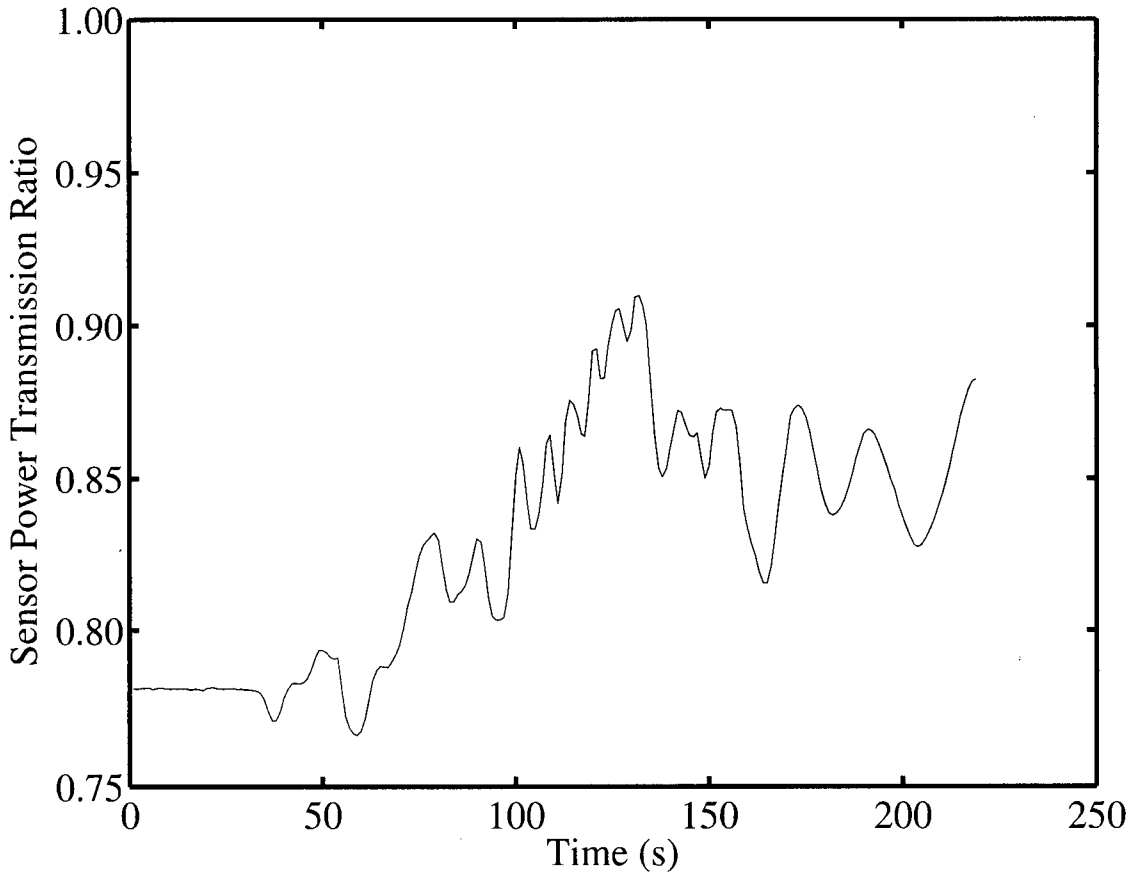

Figure 7-11: Sensor's measured power transmission ratio as a function of time with liquid level decreasing at a rapid rate for $n_{liq} = 1.461$.

principle is far more complicated, its refractive index range is limited to 1.400-1.456, it requires the use of a specific wavelength and it has a linear response over only about 60% of the grating's length.

The sensor reported here does not require the placement of any collimating optics, or receiving and transmitting fibres above the liquid surface as is required in [109]-[113]. A simple mechanical splice between a standard single-mode polarization maintaining fibre and the D-fibre is all that would be required. The sensor can also be implemented as a discrete level sensor requiring only one fibre, one source and one detector unlike other discrete level sensors that require multiple sensors [114]-[119].

The range of operation of the sensor is only limited by the length of the sensor, where a longer sensor would lead to an exponential response. This is not a serious limitation as a linear response is not necessary if appropriately calibrated. However, the sensitivity of the sensor would be less. Careful selection of the power attenuation coefficient can lead to a nearly linear response over the required length of the sensor. The refractive index of the liquid must be greater than the mode effective index of the fibre, which in our case was ~1.45. Since the liquid is in contact with the fibre, only liquids that do not modify the fibre should be used. Rapidly decreasing liquid levels can lead to errors in the sensor's response, which is likely due to residual liquid being left on the fibre surface.

Chapter 8

8 Summary, Conclusions, and Suggestions for Future Work

8.1 Summary

In summary, we have demonstrated the use of D-fibres as intensity-based fibre optic sensors. The sensor's behaviour can be adequately described using an existing theoretical model and software simulations. The exact refractive index distribution of the fibre used was unknown and thus an empirical parameter was introduced and the theoretical model was simplified to obtain closer agreement between the calculated and measured responses. This led to the development of a "non-destructive" technique to determine the etched cladding thickness to an accuracy of better than 0.3 μm.

The fibres were used to demonstrate a refractive index sensor with a high resolution on the order of 10^{-6}. We showed that there exists an optimum cladding thickness and that the maximum resolution point can be shifted by as much as ~0.012 RIUs in the region of high resolution and by ~0.027 RIUs in the region of low resolution with a corresponding change of 500 nm in the operating wavelength. The high resolution region had a narrow range whereas the low resolution region had a wide range of greater than 0.23 RIUs.

A temperature sensor using thermo-optic oils was also demonstrated. The operating point and dynamic range of this temperature sensor can be shifted or extended by selecting appropriate thermo-optic oils and by controlling the cladding thickness. Similar to the refractive index sensor, the high resolution region had a narrow range and the low resolution region had a wide range.

Proof of principle was demonstrated for an electric field sensor using chiral smectic A liquid crystals. The sensor responded linearly to an applied electric field but suffered a drift in its sensitivity, which was most likely due to the poor alignment of the liquid crystals on the surface of the fibre.

A novel liquid level sensor was also developed and implemented as a continuous level sensor. The sensor can also be implemented as a discrete level sensor using only one fibre, one source and one detector.

8.2 Conclusions

Based on the sensors presented and their characteristics, we conclude that it is possible to manufacture intensity-based fibre optic sensors using leaky modes in etched D-fibres. The etched cladding thickness can be determined to an accuracy better than 0.3 μm. The sensors investigated and presented obtain competitive dynamic ranges and resolutions as compared to existing sensors that are based on more complicated structures and principles such as fibre Bragg gratings, tapered and microstrutured fibres, surface plasmon resonance, and spectral analysis.

8.3 Suggestions for future work

Suggestions for future work aimed at improving and developing new applications for the D-fibre sensors presented here are:

1. The electric field sensor was limited by the temperature range of the liquid crystals and their poor alignment on the fibre surface. Nevertheless, with proof of principle demonstrated, it may be worthwhile to conduct surface alignment studies for aligning the liquid crystals on the fibre surface. The liquid crystals used were engineered for use on indium tin oxide coated glass surfaces, whereas the fibres used in this work presented a fluorine-doped silica surface to the liquid crystals. The engineering of liquid crystals that operate over wider temperature ranges is also needed if such sensors are to be used in the power industry for the measurement of high voltages. A working electric field sensor of the type demonstrated in this work would be ideal to create an integrated sensor for the measurement of voltages in high voltage columns, i.e., just one fibre could be run down the column to measure the integral of the electric field as opposed to using three optical point sensors as is done in some systems [127].
2. Surface plasmon resonance sensors are gaining popularity as chemical sensors due to their high resolutions [65], [66]. D-fibres are ideal platforms for growing thin metal layers on their flats to create plasmons in the interfaces between the dielectric and metal layers. The long interaction lengths possible using D-fibres could lead to distributed sensing of chemical properties.

3. Shifting of the three regions of operation of the sensor can be further increased by changing the mode effective index. This can be done by changing the refractive indices of the core and cladding, which would require manufacture of a new fibre. However, another technique is to use a grating structure to modulate the mode effective index. This could be achieved by writing long-period gratings in the fibre [16].
4. Tuneable filters using highly dispersive materials are also a possible application. By coating the fibre with a highly dispersive medium, the sharp decrease in the power transmission ratio when $n_{ext} \gtrsim n_{eff}$ can be used as a filter edge, i.e., certain wavelengths would see $n_{ext} < n_{eff}$ and thus operate in the lossless region and lower wavelengths would see $n_{ext} > n_{eff}$, leading to a sharp transmission loss. Changes in temperature (thermo-optic effect in the medium) could then be used to tune the filter edge [128].

Bibliography

[1] S. D. Crossley, "The Commercialisation of Fiber Optic Sensors," Chapter 2 in *Handbook of Optical Fibre Sensing Technology*, J. M. López-Higuera, Ed., pp. 23, John Wiley & Sons Ltd., West Sussex (2002).

[2] J. M. López-Higuera, "Introduction to Fibre Optic Sensing," Chapter 1 in *Handbook of Optical Fibre Sensing Technology*, J. M. López-Higuera, Ed. West Sussex: John Wiley & Sons Ltd., 2002, pp. 1-21.

[3] B. Culshaw and J. P. Dakin, "Introduction: Sensor Systems and Fiber Optics," Chapter 1 in *Optical Fiber Sensors: Principles and Components, Vol. 1*, J. Dakin and B. Culshaw, Eds. Norwood: Artech House, 1988, pp. 1-9.

[4] C. M. Davis, "Fiberoptic sensors: an overview," in *Proceedings of the SPIE*, vol. 412, 1983, pp. 2-8.

[5] S.-M Tseng, C.-L. Chen, 'Side-polished fibers', *Applied Optics*, vol. 31, no. 18, pp. 3438-3447, June 1992.

[6] W. Johnstone, G. Thursby, D. Moodie, K. McCallion, "Fiber-optic refractometer that utilizes multimode waveguide overlay devices," *Optics Letters*, vol. 17, no. 21, pp. 1538, November 1992.

[7] G. Raizada, B. P. Pal, "Refractometers and tuneable components based on side-polished fibers with multimode overlay waveguides: role of the superstrate," *Optics Letters*, vol. 21, no. 6, pp. 399-401, March 1996.

[8] A. Álvarez-Herrero, H. Guerrero, T. Belenguer, and D. Levy, "High-Sensitivity Temperature Sensor Based on Overlay on Side-Polished Fibers," *IEEE Photonics Technology Letters*, vol. 12, no. 8, pp. 1043-45, August 2000.

[9] D. Flannery, S. W. James, R. P. Tatam, G. J. Ashwell, "pH sensor using Langmuir Blodgett overlays on polished optical f ibers", *Optics Letters*, vol. 22, no. 8, pp. 567-69, April 1997.

[10] A. Álvarez-Herrero, H. Guerrero, and D. Levy, "High-Sensitivity Sensor of Low Relative Humidity Based on Overlay on Side-Polished Fibers," *IEEE Sensors Journal*, vol. 4, no. 1, pp. 52-56, February 2004.

[11] A. Gaston, I. Lozano, F. Perez, F. Auza, and J. Sevilla, "Evanescent Wave Optical-Fiber Sensing (Temperature, Relative Humidity, and pH Sensors)", *IEEE Sensors Journal*, vol. 3, no. 6, pp. 806-11, December 2003.

[12] A. C. Boucouvalas, M. P. Greaves, N. S. Rayit, "D shaped optical fibre for sensing applications," *Proceedings of SPIE*, vol. 798, pp. 370-5, 1987.

[13] R. H. Selfridge, G. T. Pugmire, M. Curtis, "In-situ monitoring of D-type fiber etching," *Proceedings of SPIE,* vol. 1168, pp. 314-22, 1989.

[14] T. L. Lowder, K. H. Smith, B. L. Ipson, A. R. Hawkins, R. H. Selfridge, S. M. Schultz, "High-temperature sensing using surface relief fiber Bragg gratings," *IEEE Photonics Technology Letters*, vol. 17, no. 9, pp. 1926-8, September 2005.

[15] K. H. Smith, B. L. Ipson, T. L. Lowder, A. R. Hawkins, R. H. Selfridge, and S. M. Schultz, "Surface-relief fiber Bragg gratings for sensing applications," *Applied Optics,* vol. 45, no. 8, March 2006.

[16] X. Chen, K. Zhou, L. Zhang, I. Bennion, "Optical chemsensors utilizing long-period fiber gratings UV-inscribed in D-fiber with enhanced sensitivity through cladding etching," *IEEE Photonics Technology Letters*, vol. 16, no. 5, pp. 1352- 1354, May 2004.

[17] T. Allsop, A. Gillooly, V. Mezentsev, T. Earthgrowl-Gould, R. Neal, D.J. Webb, I. Bennion, "Bending and orientational characteristics of long period gratings written in D-shaped optical fiber [directional bend sensors]," *IEEE Transactions on Instrumentation and Measurement*, vol. 53, no. 1, pp. 130-5, February 2004.

[18] I. Latka, W. Ecke, B. Hofer, C. Chojetzki, A. Reutlinger, "Fiber optic sensors for the monitoring of cryogenic spacecraft tank structures," *Proceedings of the SPIE*, vol. 5579, 2004, pp. 195-204.

[19] B. Culshaw, F. A. Muhammad, G. Stewart, S. Murray, D. Pinchbeck, J. Noms, S. Cassidy, D. Williams, I. Crisp, M. Wilkinson, R. V. Ewyk, and A. McGhee, "Evanescent wave methane detection using optical fiber," *Electronics Letters*, vol. 28, no. 24, pp. 2232-2234, November 1992.

[20] W. Jin, G. Stewart, B. Culshaw, "A liquid contamination detector for D-fibre sensors using white light interferometry," *Measurement Science & Technology*, vol. 6, no. 10, pp. 1471-5, October 1995.

[21] Y. Zhang, C. Gu, A. M. Schwartzberg, J. Z. Zhang, "Surface-enhanced Raman scattering sensor based on D-shaped fiber," *Applied Physics Letters*, vol. 87, no. 12, pp. 123105-1-319, September 2005.

[22] BeamPROP User's Guide, RSoft Inc., 200 Executive Blvd., Ossining, N.Y. 10562.

[23] A. W. Snyder and J. D. Love, 'Optical Waveguide Theory', pp. 488, Chapman and Hall, London (1983).

[24] A. K. Ghatak and K. Thygarajan, 'Optical electronics', pp. 347-354, Cambridge University Press, Cambridge (1989).

[25] D. Marcuse, "Investigation of coupling between a fiber and an infinite slab," *IEEE Journal of Lightwave Technology*, vol. 7, no. 1, pp. 122-130, January 1989.

[26] M. J. F. Digonnet, J. R. Feth, L. F. Stokes, H. J Shaw, "Measurement of the core proximity in polished fiber substrates and couplers," *Optics Letters*, vol. 10, no. 9, pp. 463-5, September 1985.

[27] A. K. Ghatak, "Leaky modes in optical waveguides," *Optical and Quantum Electronics*, vol. 17, no. 5, pp. 311-21, September 1985.

[28] J. A. Arnaud, "Transverse coupling in fiber optics, Part I: Coupling between trapped modes," *Bell System Technical Journal,* vol. 53, no. 2, pp. 217-24, February 1974.

[29] J. A. Arnaud, "Transverse coupling in fiber optics, Part II: Coupling to mode sinks," *Bell System Technical Journal,* vol. 53, no. 4, pp. 675-96, April 1974.

[30] D. J. Markos, B. L. Ipson, K. H. Smith, S. M. Schultz, R. H. Selfridge, T. D. Monte, R. B. Dyott, G. Miller, "Controlled Core Removal from a D-Shaped Optical Fiber," *Applied Optics*, vol. 42, no. 36, pp. 7121-25, December 2003.

[31] Thomas D. Monte, KVH Industries, Inc., Tinley Park, IL, private communication, August 2006.

[32] C. Yeh, "Elliptical dielectric waveguides," *Journal of Applied Physics*, vol. 33, no. 11, pp. 3235-3243, November 1962.

[33] R. B. Dyott, "Elliptical fiber waveguides," pp. 44, Artech House, Boston (1995).

[34] M. A. Jensen, R. H. Selfridge, "Analysis of etching-induced birefringence changes in elliptic core fibers," *Applied Optics*, vol. 31, no. 12, pp. 2011-2016, April 1992.

[35] A. Sharma, J. Kompella, P. K. Mishra, "Analysis of fiber directional couplers and coupler half-blocks using a new simple model for single-mode fibers," *Journal of Lightwave Technology*, vol. 8, no. 2, pp. 143-151, February 1990.

[36] O. Leminger, R. Zengerle, "Determination of single-mode fiber coupler design parameters from loss measurements," *Journal of Lightwave Technology*, vol. 3, no. 4, pp. 864-7, August 1985.

[37] S. Pilevar, A. Kumar, K. Thyagarajan, "Polarization characteristics of a metal clad elliptic-core fiber polarizer," *Optics Communications*, vol. 83, no. 1-2, pp. 31-6, May 1991.

[38] C. Vassallo, "Rigorous theory for modes of optical fibres with cladding limited by a plane," *Electronics Letters*, vol. 22, no. 18, pp. 944-5, Aug. 1986.

[39] K. Thyagarajan, S. Diggavi, A. K. Ghatak, "Analytical investigations of leaky and absorbing planar structures [integrated optic polarizers]," *Optical and Quantum Electronics*, vol. 19, no. 2, pp. 131-7, March 1987.

[40] X. Chen, B. Yu, Y. Zhu, A. Wang, "Deep wet etching on fused silica material for fiber optic sensors," in *Proceedings of the SPIE*, vol. 5342, 2004, pp. 128-36.

[41] S. M. Chandani, A. Kulpa, and N. A. F. Jaeger, "Non-destructive determination of cladding thickness in D-fibers", *IEEE Photonics Technology Letters*, vol. 18, no. 9, pp. 1082-84, May 2006.

[42] S. M. Chandani, and N. A. F. Jaeger, "Modelling of elliptical core D-fibers for determination of cladding thickness," accepted for publication in Proceedings of the SPIE, 2007, (6 pages).

[43] Y. Jung, S. Kim, D. S. Lee and K. Oh, "Compact three segmented multimode fiber modal interferometer for high sensitivity refractive-index measurement," in *Proceeding of the SPIE*, vol. 5855, 2005, pp. 150-153.

[44] J. Villatoro, D. Monzón-Hernández, "Low-cost optical fiber refractive-index sensor based on core diameter mismatch ," *IEEE Journal of Lightwave Technology*, vol. 24, no. 3, pp. 1409-1413, March 2006.

[45] A. Iadicicco, A. Cusano, S. Campopiano, A. Cutolo, M. Giordano, "Thinned fiber Bragg gratings as refractive index sensors," *IEEE Sensors Journal*, vol. 5, no. 6, pp. 1288-95, December 2005.

[46] W. Liang, Y. Huang, Y. Xu, R. K. Lee, and A. Yariv, "Highly sensitive fiber Bragg grating refractive index sensors," *Applied Physics Letters*, vol. 86, no. 15, pp. 151122-1-3, April 2005.

[47] N. Chen, B. Yun, Y. Cui, "Cladding mode resonances of etch-eroded fiber Bragg grating for ambient refractive index sensing," *Applied Physics Letters*, vol. 88, no. 13, pp. 133902-1-3, March 2006.

[48] K. Zhou, L. Zhang, X. Chen, I. Bennion, "Optic sensors of high refractive-index responsivity and low thermal cross sensitivity that use fiber Bragg gratings of >80° tilted structures," *Optics Letters*, vol. 31, no. 9, pp. 1193-5, May 2006.

[49] C-F. Chan, C. Chen, A. Jafari, A. Laronche, D. J. Thomson, and J. Albert, "Optical fiber refractometer using narrowband cladding-mode resonance shifts," *Applied Optics*, vol. 46, no. 7, pp. 1142-1149, March 2007.

[50] K. Schroeder, W. Ecke, R. Mueller, R. Willsch, A. Andreev, "A fibre Bragg grating refractometer," *Measurement Science & Technology*, vol. 12, no. 7, pp. 757-64, July 2001.

[51] G. Meltz, S. J. Hewlett, and J. D. Love, "Fiber grating evanescent-wave sensors," in *Proceedings of the SPIE*, vol. 2836, 1996, pp. 342-350.

[52] M. C. P. Huy *et al.*, "Fibre Bragg grating photowriting in microstructured optical fibres for refractive index measurement," *Measurement Science & Technology*, vol. 17, no. 5, pp. 992-7, May 2006.

[53] B. H. Lee, Y. Liu, S. B. Lee, S. S. Choi, J. N. Jang, "Displacements of the resonant peaks of a long-period fiber grating induced by a change of ambient refractive index," *Optics Letters*, vol. 22, no. 23, pp. 1769-71, December 1997.

[54] X. Shu, B. A. L. Gwandu, Y. Liu, L. Zhang. I. Bennion, "Sampled fiber Bragg grating for simultaneous refractive-index and temperature measurement," *Optics Letters*, vol. 26, no. 11, pp. 774-6, June 2001.

[55] J.-F. Ding, A. P. Zhang, L.-Y. Shao, J-H.Yan, S. He, "Fiber-taper seeded long-period grating pair as a highly sensitive refractive-index sensor," *Photonics Technology Letters*, vol. 17, no. 6, pp. 1247-9, June 2005.

[56] T. Takeo and H. Hattori, "Optical fiber sensor for measuring refractive index," *Japanese Journal of Applied Physics, Part 1* , vol. 21, no. 10, pp. 1509-12, Oct. 1982.

[57] J. Villatoro, D. Monzón-Hernández, D. Luna-Moreno, "Miniature optical fiber refractometer using cladded multimode tapered fiber tips," *Sensors and Actuators B*, vol. 110, no. 1, pp. 36-40, September 2005.

[58] P. Polynkin, A. Polynkin, N. Peyghambarian, M. Mansuripur, "Evanescent field-based optical fiber sensing device for measuring the refractive index of liquids in microfluidic channels," *Optics Letters*, vol. 30, no. 11, pp. 1273-5, June 2005.

[59] L. Falco, G. Spescha, P. Roth, O. Parriaux, "Non-ambiguous evanescent-wave fibre refractive index and temperature sensor," *Optica Acta*, vol. 33, no. 12, pp. 1563-70, December 1986.

[60] R. M. Ribeiro, J. L. P. Canedo, M. M. Werneck, L. R. Kawase, "An evanescent-coupling plastic optical fibre refractometer and absorption meter based on surface light scattering," *Sensors and Actuators A*, vol. A101, no. 1-2, pp. 69-76, September 2002.

[61] J. Zubia, G. Garitaonaindia, J. Arrue, "Passive device based on plastic optical fibers to determine the indices of refraction of liquids ," *Applied Optics*, vol. 39, no. 6, pp. 941-6, 20 February 2000.

[62] A. Iadicicco, S. Campopiano, A. Cutolo, M. Giordano, A. Cusano, "Refractive index sensor based on microstructured fiber Bragg grating," *Photonics Technology Letters*, vol. 17, no. 6, pp. 1250-2, June 2005.

[63] J. M. Trudeau *et al.*, "Combined fibre-optic sensor for colour and refractive index (CI) monitoring," *Measurement Science & Technology*, vol. 17, no. 5, pp. 1134-9, May 2006.

[64] L.-Y. Shao, A. P. Zhang, W.-S. Liu, H.-Y. Fu, S. He, "Optical refractive-index sensor based on dual fiber-Bragg gratings interposed with a multimode-fiber taper," *IEEE Photonics Technology Letters*, vol. 19, no. 1, pp. 30-2, January 2007.

[65] J. Homola, S. S. Yee, G. Gauglitz, "Surface plasmon resonance sensors: review," *Sensors and Actuators B*, vol. B54, no. 1-2, pp. 3-15, January 1999.

[66] D. Monzón-Hernández. J. Villatoro, , "High-resolution refractive index sensing by means of a multiple-peak surface plasmon resonance optical fiber sensor," *Sensors and Actuators B*, vol. 115, no. 1, pp. 227-231, May 2006.

[67] R. Slavík J. Homola and J. Čtyroký, "Single-mode optical fiber surface plasmon resonance sensor," *Sensors and Actuators B*, vol. 54, no. 1-2, pp. 74-79, Jan 1999.

[68] M-.H Chiu, S-.F. Wang and R-.S. Chang, "D-type fiber biosensor based on surface-plasmon resonance technology and heterodyne interferometry," *Optics Letters*, vol. 30, no. 3, pp. 233-235, February 2005.

[69] R. B. Dyott, *Elliptical Fiber Waveguides*. Norwood, MA: Artech House, 1995, pp. 100-102.

[70] B. E. Jones, R. S. Medlock, R. C. Spooncer, "Intensity and Wavelength-Based Sensor and Optical Actuators," Chapter 12 in *Optical Fiber Sensors: Systems and Applications, Vol. 2*, B. Culshaw and J. Dakin, Eds., pp. 433-434, Artech House, Norwood, (1989).

[71] A. C. García, J. E. Cuena, "Transduction Techniques based on Intensity Modulation of Light," Chapter 11 in *Handbook of Optical Fibre Sensing Technology*, J. M. López-Higuera, Ed., pp. 221-2233, John Wiley & Sons Ltd., West Sussex (2002).

[72] A. D. Kersey, T. A. Berkoff, "Fiber-optic Bragg-grating differential-temperature sensor," *IEEE Photonics Technology Letters*, vol. 4, no. 10, pp. 1183-5, October 1992.

[73] B. Zhang, M. Kahrizi, "High-Temperature Resistance Fiber Bragg Grating Temperature Sensor Fabrication," *IEEE Sensors Journal,* vol. 7, no. 4, pp. 586–591, April 2007.

[74] A. I. Gusarov, D. S. Starodubov, F. Berghmans, O. Deparis, Y. Defosse, A. Fernandez, M. Decreton, P. Megret, M. Blondel, "Design of a radiation-hard optical fibre Bragg grating temperature sensor," *Proceedings of the SPIE*, vol. 3872, 1999, p 43-50.

[75] M. W. Hathaway, N. E. Fisher, D. J. Webb, C. N. Pannell, D. A. Jackson, L. R. Gavrilov, J. W. Hand, L. Zhang, I. Bennion, "Combined ultrasound and temperature sensor using a fibre Bragg grating," *Optics Communications*, vol. 171, no. 4-6, pp. 225-31, December 1999.

[76] W.-G. Jung, S.-W. Kim, K.-T. Kim, E.-S. Kim, and S.-W. Kang, "High sensitivity temperature sensor using a side-polished single-mode fiber covered with the polymer planar waveguide," *IEEE Photonics Technology Letters*, vol. 13, no. 11, pp. 1209–1211, November 2001.

[77] J. Senosiain, I. Diaz, A. Gaston, and J. Sevilla, "High sensitivity temperature sensor based on side-polished optical fiber," *IEEE Transactions on Instrumentation and Measurement*, vol. 50, no. 6, pp. 1656–1660, December 2001.

[78] L. Falco, H. Berthou, F. Cochet, B. Scheja, and O. Parriaux, "Temperature sensor using single mode fiber evanescent field absorption," in *Proceedings of the SPIE*, vol. 586, 1986, pp. 114–119.

[79] G. Betta and A. Pietrosanto, "An intrinsic fiber optic temperature sensor," in *Proceedings of the IEEE Instrumentation Measurement Technology Conference*, vol. 2, May 1998, pp. 1067–1070.

[80] J. Kusznier, "Optical fiber temperature sensor," in *Proceedings of the SPIE*, vol. 5028, 2003, pp. 150–154.

[81] K. H. Smith, B. L. Ipson, R. H. Selfridge, and S. M. Schultz, "Versatile in-fiber sensing by use of core-replaced D-fiber," *Applied Optics*, vol. 44, no. 1, pp. 22–26, 2005.

[82] S. M. Chandani and N. A. F. Jaeger, "Fiber-optic temperature sensor using evanescent fields in D fibers", *IEEE Photonics Technology Letters*, vol. 17, no. 12, pp. 2706-8, Dec. 2005.

[83] A. J. Rogers, "Optical technique for the measurement of current at high voltage," in *Proceedings of the IEE*, vol. 120, no. 2, pp. 261-267, 1973.

[84] G. A. Massey, D.C. Erickson, and R.A. Kaldec, "Electromagnetic field components: their measurement using linear electrooptic and magnetooptic effects," *Applied Optics*, vol. 14, no. 11, pp. 2712-2719, November 1975.

[85] A. J. Rogers, "Method for simultaneous measurement of current and voltage on a high-voltage lines using optical techniques," in *Proceedings of the IEE*, vol. 123, no. 10, pp. 957-960, 1976.

[86] R. E. Hebner, R. A. Malewski, E. C. Cassidy, "Optical methods of electrical measurements at high voltage levels," in *Proceedings of the IEEE*, vol. 65, no. 11, pp. 1524-1548, 1977.

[87] J. A. Valdmanis, "Electro-optic measurement techniques for picosecond materials, devices, and integrated circuits," in *Measurement of High-Speed Signals in Solid State Devices*, edited by R. B. Marcus, Academic Press, San Diego, pp. 136-217, 1990.

[88] M. J. Ahmed, "*Integrated optical devices in lithium niobate*," Ph.D. dissertation, University of British Columbia, Vancouver, B.C., Canada, 1981.

[89] N. A. F. Jaeger, "*Integrated optical devices in lithium niobate*," M.A.Sc thesis, University of British Columbia, Vancouver, B.C., Canada, 1985.

[90] N. A. F. Jaeger, L. Young, "High-voltage sensor employing an integrated optics Mach-Zehnder interferometer in conjunction with a capacitive divider," *IEEE Journal of Lightwave Technology*, vol. 7, no. 2, pp. 229-235, February 1989.

[91] N. A. F. Jaeger, "Integrated Optics Pockels Cell Voltage Sensor," U.S. Patent #5,029,273, July 2, 1991.

[92] F. Rahmatian, "*Integrated optics Pockels cell high voltage sensor*," M.A.Sc. thesis, University of British Columbia, Vancouver, B.C., Canada, 1993.

[93] G. Andersson *et al.*, ''Device physics of the soft mode electro-optic effect,'' *Journal of Applied Physics*, vol. 66, no. 10, pp. 4983-95, November 1989.

[94] A. Sneh, K. M. Johnson, "High-speed continuously tuneable liquid crystal filter for WDM networks," *Journal of Lightwave Technology,* vol. 14, no. 6, pp. 1067-1080, June 1996.

[95] Luigi Sirleto *et al.*, "Electro-optical switch and continuously tuneable filter based on a Bragg grating in a planar waveguide with a liquid crystal overlayer," *Optical Engineering,* vol. 4, no.11, pp. 2890–2898, November 2002.

[96] B. M. Lacquet, P. L. Swart, S. J. Spammer, "Polymer dispersed liquid crystal fiber-optic electric field probe," *IEEE Transactions on Instrumentation and Measurement*, vol. 46, no. 1, pp. 31-5, February 1997.

[97] F. Anagni, C. Bartoletti, U. Marchetti, L. Podesta, G. Sacerdoti, "Optical sensors for electric substations: a voltage presence detector using a liquid crystal cell," *IEEE Transactions on Instrumentation and Measurement*, vol. 43, no. 3, pp. 475-80, June 1994.

[98] S. Sato and T. Hara, "Applications of a ferroelectric liquid-crystal cell to an electric field sensor," *Japanese Journal of Applied Physics,* vol. 32, no. 8, pp. 3664–3665, August 1993.

[99] S. M. Chandani, N. A. F. Jaeger, R.-F. Shao, and J. E. Maclennan, "In-line D-fiber electric field sensor using chiral liquid crystals", in *Proceedings of the SPIE*, vol. 6343, pp. 634317-1-10, September 2006.

[100] S. M. Chandani, N. A. F. Jaeger, R.-F. Shao, and J. E. Maclennan, "Electric field sensor using smectic A liquid crystals", International Liquid Crystal Conference, Keystone, Colorado, July 2 - 7, 2006.

[101] S. Garoff and R. B. Meyer, 'Electroclinic Effect at the A-C Phase Change in a Chiral Smectic Liquid Crystal', *Physics Review Letters*, vol. 38, no. 15, pp. 848-51, April 1977.

[102] C. C. Davis, *Lasers and Electro-Optics: Fundamentals and Engineering*, Cambridge University Press, Cambridge, 1996, pp. 448.

[103] R-F. Shao, J. E. Maclennan, N. A. Clark, D. J. Dyer, D. M. Walba, "Giant surface electroclinic effect in a chiral smectic A liquid crystal," *Liquid Crystals*, vol. 28, no. 1, pp. 117-23, January 2001.

[104] C. Kittel, Introduction to solid state physics, Wiley, New York, 1956, pp. 157.

[105] J. A. Morris, C. R. Pollock, "A digital fiber-optic liquid level sensor," *IEEE Journal of Lightwave Technology*, vol. 5, no. 7, pp. 920-925, July 1987.

[106] L. A. Danisch, "Removing index of refraction constraints in the optical measurement of liquid level," in *Proceedings of the SPIE*, vol. 1795, 1993, pp. 268-279.

[107] S. Khaliq, S. W. James, R. P. Tatam, "Fiber-optic liquid-level sensor using a long-period grating," *Optics Letters*, vol. 26, no. 16, pp. 1224-1226, August 2001.

[108] F. Pérez-Ocón, M. Rubiño, J. M. Abril, P. Casanova, J. A. Martínez, "Fiber-optic liquid-level continuous gauge," *Sensors and Actuators A*, vol. A125, no. 2, pp. 124-132, January 2006.

[109] K. Iwamoto, I. Kamata, "Liquid-level sensor with optical fibers," *Applied Optics*, vol. 31, no. 1, pp. 51-54, January 1992.

[110] C. Vázquez, A. B. Gonzlo, S. Vargas, J. Montalvo, "Multi-sensor system using plastic optical fibers for intrinsically safe level measurements," *Sensors and Actuators A*, vol. A116, no. 1, pp. 22-32, October 2004.

[111] D. A. Jackson, "High precision remote liquid level measurement using a combination of optical radar and optical fibers," in *Proceedings of First International IEE Conference on Optical Fiber Sensors*, London, England, 1983, pp. 100-103.

[112] W. Peng, J. Lin, "The study on Ladar fiber optical liquid level sensor system," in *Proceedings of the SPIE*, vol. 3740, 1999, pp. 488-491.

[113] L. Yan-Bing, Y. Yong-Hua, "Optical remote measurement of liquid level," in *Proceedings of the SPIE*, vol. 2101, 1993, pp. 1004-1007.

[114] A. Wang, M. F. Gunther, K. A. Murphy, R. O. Claus, "Fiber-optic liquid-level sensor," *Sensors and Actuators A*, vol. A35, no. 2, pp. 161-164, December 1992.

[115] I. K. Ilev, R. W. Waynant, "All-fiber-optic sensor for liquid level measurement," *Review of Scientific Instruments*, vol. 70, no. 5, pp. 2551-2554, May 1999.

[116] L. Ren, Q. Yu, "High-accuracy fiber optic level sensor," in *Proceedings of the SPIE*, vol. 4920, 2002, pp. 362-366.

[117] C. Yang, S. Chen, G. Yang, "Fiber optical liquid level sensor under cryogenic environment," *Sensors and Actuators A*, vol. A94, no. 1, pp. 69-75, October 2001.

[118] P. Raatikainen, I. Kassamakov, R. Kakanakov, M. Luukkala, "Fiber-optic liquid-level sensor," *Sensors and Actuators A*, vol. A58, no. 2, pp. 93-97, February 1997.

[119] K. E. Romo-Medrano, S. N. Khotiaintsev, "An optical-fibre refractometric liquid-level sensor for liquid nitrogen," *Measurement Science & Technology*, vol. 17, no. 5, pp. 998-1004, May 2006.

[120] G. Betta, A. Pietrosanto, A. Scaglione, "A Gray-code-based fiber optic liquid level transducer," *IEEE Transactions on Instrumentation and Measurement*, vol. 47, no. 1, pp. 174-178, February 1998.

[121] S. M. Chandani, and N. A. F. Jaeger, "An optical fiber-based liquid level sensor," accepted for publication in *Optical Engineering*, 5-6 pages, 2007.

[122] http://www.soes.soton.ac.uk/research/groups/oil_monitor/oiltype.htm

[123] A. C. García, J. E. Cuena, "Transduction Techniques Based on Intensity Modulation of Light," Chapter 11 in *Handbook of Optical Fiber Sensing Technology*, J. M. López-Higuera, Ed., pp. 221-223, John Wiley & Sons Ltd., West Sussex (2002).

[124] B. E. Jones, R. S. Medlock, R. C. Spooncer, "Intensity and Wavelength-Based Sensors and Optical Actuators," Chap. 12 in *Optical Fiber Sensors: Systems and Applications Volume 2*, B. Culshaw and J. Dakin, Eds., pp. 433-434, Artech House, Norwood, (1989).

[125] A. T. Andreev, K. P. Panajotov, "Distributed single-mode fiber to single-mode planar waveguide coupler," *Journal of Lightwave Technology,* vol. 11, no. 12, pp. 1985-89, December 1993.

[126] W. Johnstone, S. Murray, G. Thursby, M. Gill, A. McDonach, D. Moodie, B. Culshaw, "Fiber optic modulators using active multimode waveguide overlays", *Electronics Letters*, vol. 27, no. 11, pp. 894-896, March 1991.

[127] Patrick P. Chavez, Nicolas A.F. Jaeger, Farnoosh Rahmatian, "Accurate voltage measurement by the quadrature method," *IEEE Transactions on Power Delivery*, vol. 18, no. 1, pp. 14-19, January 2003.

[128] N.-K. Chen, S. Chi, S.-M. Tseng, "Wideband tunable fiber short-pass filter based on side-polished fiber with dispersive polymer overlay," *Optics Letters*, vol. 29, no. 19, pp. 2219-2221, October 2004.